Coffin, M.F., Frey, F.A., Wallace, P.J., et al., 2000
Proceedings of the Ocean Drilling Program, Initial Reports Volume 183

2. EXPLANATORY NOTES[1]

Shipboard Scientific Party[2]

INTRODUCTION

Introduction

In this chapter, we describe the shipboard procedures and observations that led to our preliminary conclusions. These data are also useful for selecting samples for shore-based research. This information concerns only shipboard operations and analyses described in the site reports in the Leg 183 *Initial Reports* volume of the *Proceedings of the Ocean Drilling Program*. Methods used by various investigators for shore-based analyses of Leg 183 data will be described in the individual scientific contributions to be published in the *Scientific Results* volume.

Authorship of Site Chapters

The separate sections of the site chapters were written by the following shipboard scientists (authors are listed in alphabetical order):

Background and Objectives: Mike Coffin, Fred Frey
Operations: Mike Storms, Paul Wallace
Lithostratigraphy: Florian Boehm, John Damuth, Douglas Reusch, Veronika Wähnert
Biostratigraphy: Helen Coxall, Veronika Wähnert, Woody Wise
Physical Volcanology: Laszlo Keszthelyi, Leah Moore
Igneous Petrology: Nicholas Arndt, Jane Barling, Robert Duncan, John Mahoney, Clive Neal, Kirsten Nicolaysen, Malcolm Pringle, Paul Wallace, Dominique Weis
Alteration and Weathering: Peter Saccocia, Damon Teagle
Structural Geology: Laszlo Keszthelyi, Peter Saccocia, Damon Teagle
Paleomagnetism: Maria Antretter, Hiroo Inokuchi
Physical Properties: Mai Borre, Xixi Zhao

[1]Examples of how to reference the whole or part of this volume.
[2]Shipboard Scientific Party addresses.

Ms 183IR-102

Organic and Inorganic Geochemistry: Erik Moortgat, Paul Wallace
Seismic Stratigraphy: Dietmar Müller
Downhole Measurements: Heike Delius, Dietmar Müller
Appendix: Shipboard Scientific Party

In addition to each site chapter, summary core descriptions ("barrel sheets" and images of each core) are presented (see the "Core Descriptions" contents list).

Shipboard Scientific Procedures

Numbering of Sites, Holes, Cores, and Samples

Ocean Drilling Program (ODP) drill sites are numbered consecutively and refer to one or more holes drilled while the ship was positioned over one acoustic beacon. Multiple holes may be drilled at a single site by pulling the drill pipe above the seafloor (out of the hole), moving the ship some distance from the previous hole, and then drilling another hole.

For all ODP drill sites, a letter suffix distinguishes holes drilled at the same site. The first hole drilled is assigned the site number modified by the suffix "-A"; the second hole takes the site number and suffix "-B," and so forth. Note that this procedure differs slightly from that used by the Deep Sea Drilling Project (DSDP; Sites 1 through 624), but it prevents ambiguity between site- and hole-number designations. It is important to distinguish among holes drilled at a site because recovered sediments or rocks from different holes usually do not come from equivalent positions in the stratigraphic column.

The cored interval is measured in meters below seafloor (mbsf). The depth interval assigned to an individual core begins with the depth below the seafloor at which the coring began and extends to the depth that the coring ended. Each coring interval is generally up to 9.5 m long, which is the length of a core barrel. Coring intervals may be shorter and may not necessarily be adjacent if separated by drilled intervals. In soft sediments, the drill string can be "washed ahead" with the core barrel in place, without recovering sediments. This is achieved by pumping water down the pipe at high pressure to wash the sediment out of the way of the bit and up the space between the drill pipe and the wall of the hole. If thin, hard rock layers are present, then it is possible to get "spotty" sampling of these resistant layers within the washed interval and thus to have a cored interval >9.5 m. When drilling hard rock, a center bit may replace the core barrel if it is necessary to drill without core recovery.

Cores taken from a hole are numbered serially from the top of the hole downward. Core numbers and their associated cored intervals in meters below seafloor usually are unique in a given hole; however, this may not be true if an interval must be cored twice because of caving of cuttings or other hole problems. Maximum recovery for a single core is 9.5 m of rock or sediment contained in a plastic liner (6.6-cm internal diameter) plus about 0.2 m (without a plastic liner) in the core catcher (Fig. F1). The core catcher is a device at the bottom of the core barrel that prevents the core from sliding out when the barrel is being retrieved from the hole. In certain situations (e.g., when coring gas-charged sediments that expand while being brought on deck) recovery may exceed the 9.5-m maximum.

F1. Examples of numbered core sections, p. 55.

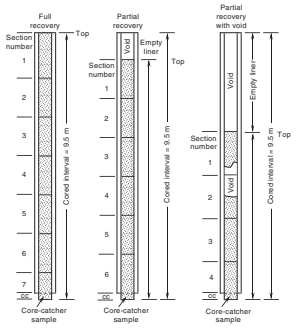

A recovered core is divided into 1.5-m sections that are numbered serially from the top (Fig. F1). When full recovery is obtained, the sections are numbered from 1 through 7, with the last section possibly being shorter than 1.5 m (rarely, an unusually long core may require more than seven sections). When less than full recovery is obtained, as many sections as needed to accommodate the length of the core will be recovered (e.g., 4 m of core would be divided into two 1.5-m sections and one 1-m section). If cores are fragmented (recovery is <100%), sections are numbered serially and intervening sections are noted as void, whether shipboard scientists believe that the fragments were contiguous in situ or not. In rare cases, a section <1.5 m may be cut to preserve features of interest (e.g., lithologic contacts).

By convention, material recovered from the core catcher is placed below the last section when the core is described and is labeled "core catcher" (CC); in sedimentary cores, this is treated as a separate section. The core catcher is placed at the top of the cored interval in cases where material is recovered only in the core catcher. However, information supplied by the drillers or by other sources may allow for more precise interpretation as to the correct position of core-catcher material within an incompletely recovered cored interval.

When the recovered core is shorter than the cored interval, the top of the core is equated with the top of the cored interval by convention to achieve consistency when handling analytical data derived from the cores. Samples removed from the cores are designated by distance, measured in centimeters from the top of the section to the top and bottom of each sample removed from that section.

A complete identification number for a sample consists of the following information: leg, site, hole, core number, core type, section number, piece number (for hard rock), and interval in centimeters measured from the top of the section. For example, a sample identification of "183-1135A-25R-1, 10–12 cm" would be interpreted as representing a sample removed from the interval between 10 and 12 cm below the top of Section 1, Core 25 (R designates that this core was taken during rotary drilling) of Hole 1135A during Leg 183.

All ODP core and sample identifiers indicate core type. The following abbreviations were used: R = rotary core barrel (RCB); B = drill-bit recovery; C = center-bit recovery; S = sidewall sample; W = washed-core recovery; and M = miscellaneous material. Only RCB cores were cut during Leg 183.

Core Handling

Sediments

As soon as a core is retrieved on deck, a sample is taken from the core catcher and given to the paleontology laboratory for an initial age assessment. Then the core is placed on a long horizontal rack, and gas samples may be taken by piercing the core liner and withdrawing gas into a vacuum tube. Voids within the core are sought as sites for gas sampling. Some of the gas samples are stored for shore-based study, but others are analyzed immediately as part of the shipboard safety and pollution-prevention program. Next, the core is marked into section lengths, each section is labeled, and the core is cut into sections. Headspace gas samples are scraped from the ends of cut sections on the catwalk and sealed in glass vials for light hydrocarbon analysis. Each section then is sealed at the top and bottom by gluing on color-coded

plastic caps: blue to identify the top of a section, and clear for the bottom. A yellow cap is placed on the section ends from which a whole-round sample has been removed. These caps are usually attached to the liner by coating the end liner and the inside rim of the cap with acetone, and then the caps are taped to the liners.

Next, the cores are carried into the laboratory where the sections again are labeled. An engraver is used to permanently mark the full designation of each section. The length of the core in each section and the core-catcher sample are measured to the nearest centimeter. This information is logged into the shipboard CORELOG database program. After cores have equilibrated to room temperature (~3 hr), they are run through the multisensor track (MST), thermal conductivity measurements are performed on relatively soft sediments, and the cores are split.

Cores of soft material are split lengthwise into working and archive halves. The softer cores are split with a wire or saw, depending on the degree of induration. Harder cores are split with a diamond saw. During Leg 183, the wire-cut cores were split from the bottom to top; thus, investigators should be aware that older material may have been transported up the core on the split face of each section.

The working half of the core is sampled for both shipboard and shore-based laboratory studies. Each extracted sample is logged into the sampling computer database program by the location and the name of the investigator receiving the sample. Records of all removed samples are kept by the curator at ODP. The extracted samples are sealed in plastic vials or bags and labeled. Samples are routinely taken for shipboard physical properties analysis and for calcium carbonate (coulometric analysis) and organic carbon (CNS elemental analyzer) analyses.

The archive half is described visually. Smear slides are made from sediment samples taken from the archive half. Most archive sections are run through the cryogenic magnetometer. The archive half then is photographed using both black-and-white and color film, a whole core at a time. Close-up photographs (black and white) are taken of particular features for illustrations in the summary of each site, as requested by individual scientists.

Both halves of the core then are placed into labeled plastic tubes, sealed, and transferred to cold-storage space aboard the drilling vessel. At the end of the leg, the cores are transferred from the ship in refrigerated air-freight containers to cold storage at the Gulf Coast Repository of the Ocean Drilling Program at Texas A&M University.

Igneous and Metamorphic Rocks

Igneous-rock cores are handled differently than sedimentary cores. Once on deck, the core-catcher sample is placed at the bottom of the core liner, and total core recovery is calculated by shunting the rock pieces together and measuring to the nearest centimeter. This information is logged into the shipboard CORELOG database program. The core is then cut into 1.5-m-long sections and transferred into the laboratory.

The contents of each section are transferred into 1.5-m-long sections of split-core liner, where the bottom of oriented pieces (i.e., pieces that clearly could not have rotated top to bottom about a horizontal axis in the liner) are marked with a red wax pencil. This is to ensure that orientation is not lost during the splitting and labeling processes. Important primary features of the cores also are recorded at this time. The core is

then split into archive and working halves. A plastic spacer is used to separate individual pieces and/or reconstructed groups of pieces in the core liner. These spacers may represent a substantial interval of no recovery. Each piece is numbered sequentially from the top of each section, beginning with number 1; reconstructed groups of pieces are assigned the same number, but are lettered consecutively. Pieces are labeled only on the outer cylindrical surfaces of the core. If the piece is oriented, an arrow is added to the label pointing to the top of the section. Because pieces are free to turn about a vertical axis during drilling, azimuthal orientation during Leg 183 was possible only by using paleomagnetic or downhole logging data.

In splitting the core, every effort is made to ensure that important features are represented in both halves. The working half is sampled for shipboard physical properties measurements, magnetic studies, X-ray fluorescence (XRF), X-ray diffraction (XRD), and thin-section studies. Nondestructive physical properties measurements, such as magnetic susceptibility, are performed on the archive half of the core. Where recovery permits, samples are taken from each lithologic unit. Some of these samples are minicores. The archive half is described using the visual core description (VCD) form and is photographed before storage.

The working half of the hard-rock core then is sampled for shipboard laboratory studies. Records of all samples are kept by the curator at ODP. The archive half is described visually, then photographed with both black-and-white and color film, one core at a time. Both halves of the core are then shrink-wrapped in plastic to prevent rock pieces from vibrating out of sequence during transit, placed into labeled plastic tubes, sealed, and transferred to cold-storage space aboard the drilling vessel. As with the other Leg 183 cores, they are housed at ODP's Gulf Coast Repository.

SITE GEOPHYSICS

Sites for Leg 183 were selected on the basis of multichannel seismic (MCS), bathymetric, satellite-derived gravity, sonobuoy, coring, and dredge data collected during several surveys on board Australian, French, and U.S. ships (Fig. F2). The type and quality of seismic site survey data vary (see Table T1 for a summary of seismic parameters). Some surveys were undertaken before the availability of Global Positioning System (GPS) coverage, and these have less reliable navigation data.

Rig Seismic Survey 47

Australian Geological Survey Organisation (AGSO) scientists on board the *Rig Seismic* acquired 5600 km of MCS, bathymetric, gravity, and magnetic data over the Kerguelen Plateau between 50°S and 60°S in 1985 (Ramsay et al., 1986). Segments of the *Rig Seismic* Survey 47 (RS47) MCS data were used to locate proposed drill sites KIP-7C (central plateau), 10C (Enderby Basin), and 14C (Labuan Basin).

Marion Dufresne Cruise 47

The 1986 *Marion Dufresne* survey (MD47) examined the plateau between 55°S and 63°S, collecting 4450 km of coincident MCS, bathymetric, gravity, and magnetic data (Schlich et al., 1988). Proposed drill site KIP-13A (southern plateau) is located at the intersection of the MD47

F2. Bathymetry of the Kerguelen Plateau, p. 56.

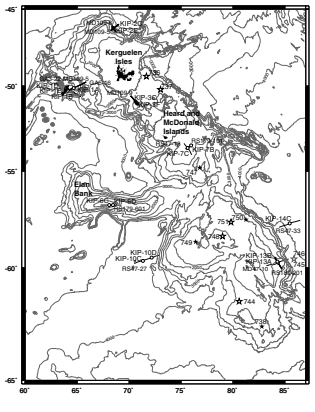

T1. Data used in selecting drill sites on the Kerguelen Plateau and Broken Ridge, p. 75.

and the *Rig Seismic* survey 180 (RS180) MCS lines, and KIP-13C (Site 1136) lies nearby on the plateau's eastern flank.

Robert D. Conrad Cruise 2708

As part of ODP site surveys for Leg 121 in 1986, scientists on board the *Robert D. Conrad* acquired 4400 km of single-channel seismic reflection, bathymetry, gravity, and magnetic data on Broken Ridge, including some data in the vicinity of proposed drill sites KIP-9B and KIP-9C (Peirce, Weissel, et al., 1989). In addition, more than 50 sonobuoys were deployed to investigate the velocity structure of the sedimentary section. The site survey was conducted by Lamont-Doherty Earth Observatory (LDEO) scientists (Chief Scientist Jeffrey K. Weissel) and supported by the U.S. National Science Foundation.

Rig Seismic Survey 179/180

During two 6-week marine surveys over the southern Kerguelen Plateau in 1997, AGSO and University of Texas Institute for Geophysics scientists acquired ~3500 km of high-quality MCS and other geophysical data. Survey 179 concentrated on Elan Bank, a prominent salient extending westward from the main Kerguelen Plateau (see Fig. **F2**). Two short lines were recorded specifically to support ODP drilling on the central Kerguelen Plateau (proposed drill sites KIP-7B [Site 1138] and KIP-7C) and Elan Bank (KIP-6C [Site 1137] and KIP-6D). Approximately 2000 km of MCS data was collected together with bathymetric, gravity, and magnetic data. Survey 180 focused on the plateau's eastern margin, including a short ODP site survey on the southern Kerguelen Plateau (KIP-13A and KIP-13B [Site 1135]). MCS data from survey 180 total ~1500 line-km with coincident bathymetric, gravity, and magnetic data.

Australia's site surveys on board the *Rig Seismic* were funded and conducted by AGSO (Project Leader Phil Symonds; cruise leaders Doug Ramsay and George Bernadel), in collaboration with the Institute for Geophysics, The University of Texas at Austin (MCS data processing), and the Department of Geology, University of Oslo, Norway, with financial support for U.S. scientist involvement provided by the U.S. Science Support Program of Joint Oceanographic Institutions, Inc.

Marion Dufresne Cruise 109

The KERIMIS (Kerguelen, Imagerie Multifasceau et Imagerie Sismique) campaign, in February and March of 1998, acquired ~2000 km of MCS data and dredged >1000 kg of rocks from the northern Kerguelen Plateau to investigate the feature's structure and geodynamics and to conduct site surveys for ODP Leg 183. Two major transects across the entire northern plateau from the Enderby Basin to the Australia-Antarctic Basin were completed, and three dedicated site surveys were undertaken for proposed drill sites KIP-1D (Site 1139) and KIP-1E (Skiff Bank/Leclaire Rise), KIP-2C and KIP-2E (Site 1140) (northern plateau), and KIP-3C and KIP-3F (central plateau).

France's site survey on board the *Marion Dufresne* was conducted by the Ecole et Observatoire des Sciences de la Terre of the Université Louis Pasteur (Strasbourg 1) (Chief Scientist Roland Schlich), in collaboration with the Département des Sciences de la Terre et de l'Environnement de l'Université Libre de Bruxelles, with the assistance of the Institut

Français de la Recherche et de l'Exploitation de la Mer with MCS, and the logistical and financial support of the Institut Français pour la Recherche et al Technologie Polaires.

LITHOSTRATIGRAPHY

This section outlines the procedures for documenting the basic sedimentology of the sedimentary deposits recovered in cores drilled during Leg 183, including core description, XRD, color spectrophotometry, and smear-slide preparation. Only general procedures are outlined, except where they depart significantly from ODP conventions. This section applies only to sedimentary deposits recovered; procedures followed for description of igneous and metamorphic rocks recovered during Leg 183 are described in "Physical Volcanology," p. 16, "Igneous Petrology," p. 22, "Alteration and Weathering," p. 25, and "Structural Geology," p. 27.

Visual Core Description

Information from megascopic description of each core was recorded manually for each core section on paper VCD forms. This information was then condensed and entered into AppleCORE (version 0.7.5g) software, which generates a simplified, one-page graphical description ("barrel sheet") of each core. Barrel sheets are presented with whole-core images (see the "Core Descriptions" contents list). The lithologies of the recovered sediments are represented on barrel sheets by symbols in the column entitled "Graphic Lithology" (Fig. F3). Grain-size divisions for siliciclastic sand, silt, and clay are those of Wentworth (1922) (see "Sediment Classification," p. 8). The siliciclastic fraction is represented by a single "Siliciclastic Sediment" symbol if it is homogeneous in texture, or by two vertical strips of these symbols if texturally distinct siliciclastic sediments are interbedded (e.g., interbeds of sand and clay). Alternatively, in some cases, where each interval of interbedded lithologies can be graphically displayed, these lithologies are shown by horizontal strips of the two siliciclastic symbols.

Sediment color was generally determined visually; in most cases the Munsell Soil Color Charts (1971) were used to give a more precise color to a sediment interval. A wide variety of features that characterize the sediment, such as bed thicknesses, primary sedimentary structures, bioturbation parameters, soft-sediment deformation, and structural and diagenetic features are indicated in columns to the right of the graphic log. The symbols are schematic, but are placed as close as possible to their proper stratigraphic position. For exact positions of sedimentary features, the detailed section-by-section paper VCDs can be obtained from ODP. A key to the full set of symbols used on the graphic sedimentologic columns is shown in Figure F3. Bed thickness is characterized by the terms "very thick bedded" (>100 cm thick), "thick bedded" (30–100 cm thick), "medium bedded" (10–30 cm thick), "thin bedded" (3–10 cm thick), and "very thin bedded" (1–3 cm thick) (McKee and Weir, 1953).

Deformation and disturbance of sediment that clearly resulted from the coring process are illustrated in the "Drilling Disturbance" column, using symbols shown in Figure F3. Blank regions indicate the absence of coring disturbance. Detailed accounts of drilling disturbance appear in many previous ODP volumes (e.g., Leg 155, Shipboard Scientific

F3. Key to symbols used in the barrel sheets, p. 57.

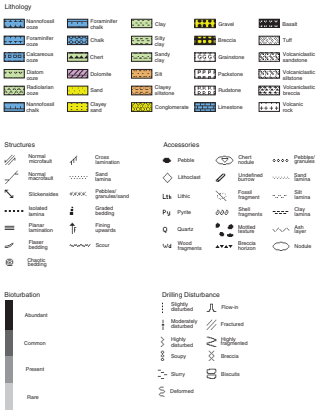

Party, 1995). Locations of all samples taken for shipboard analysis are indicated in the "Samples" column by the codes listed in Figure F3.

A summary lithologic description with sedimentologic highlights is given in the "Remarks" column of the barrel sheet. This generally gives all the major sediment lithologies; important minor lithologies; an extended summary description of the sediments, including color, composition, sedimentary structures, trace fossils identified, extent of bioturbation, and other notable characteristics; and age of the sediments as determined by shipboard paleontologists and paleomagnetists. Descriptions and locations of thin, interbedded, or minor lithologies that could not be depicted in the "Graphic Lithology" column are presented in the "Remarks" column, where space permits.

Sediment Classification

The sediment classification scheme used during Leg 183 is descriptive and follows the ODP classification (Mazzullo et al., 1988), with some simplifying modifications for mixed siliclastic and biogenic sediments (Fig. F4). Classification is based primarily on megascopic description of the cores and examination of smear slides. During Leg 183, total calcium carbonate content of the sediments determined on board (see "Organic and Inorganic Geochemistry," p. 37) was also used to aid in classification. Composition and texture are the only criteria used to define lithology. Genetic terms (such as pelagic, neritic, hemipelagic, debris flow, and so forth) do not appear in this classification. The term "clay" is used only for particle size and is applied to both clay minerals and other siliciclastic material <4 mm in size. Biogenic components are not described in textural terms. Thus, a sediment with 55% sand-sized foraminifers and 45% siliciclastic clay is called a foraminifer clay, not a foraminifer clayey sand. Similar considerations apply to sediment containing abundant sand-sized glauconite.

The principal name applied to a sediment is determined by the component or group of components (e.g., total biogenic carbonate) that comprise(s) >60% of the sediment or rock, except for subequal mixtures of biogenic and siliciclastic material. If the total of a siliciclastic component is >40%, the main name is determined by the relative proportions of sand, silt, and clay sizes when plotted on a modified Shepard (1954) classification diagram (Fig. F4A). Examples of siliciclastic principal names are clay, silt, silty clay, sandy mud, or sand. However, if the total of biogenic components is >60% (i.e., siliciclastic material <40%), then the principal name applied is "ooze" (Fig. F4B).

In mixtures of biogenic and nonbiogenic material, where the biogenic content is 30%–60% (termed "mixed sediments" in the ODP classification), the name consists of two parts: (1) the major modifier(s) consisting of the name(s) of the major fossil(s), with the least common fossil listed first, followed by (2) the principal name appropriate for the siliciclastic components (e.g., foraminiferal clay) (Fig. F4B). If any component (biogenic or siliciclastic) represents only 10%–30% of a sediment, it qualifies for minor modifier status and is hyphenated with the word "-bearing" (e.g., nannofossil-bearing clay). In cases of approximately subequal mixtures of calcareous microfossils, the modifiers "calcareous" or "carbonate-bearing" can be used instead of microfossil names (e.g., calcareous clay).

F4. Textural classification scheme and sediment naming procedure, p. 58.

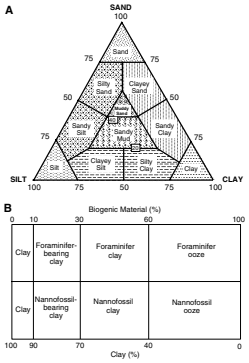

Examples: foraminifer-bearing nannofossil clay
(11%) (34%) (55%)
diatom-bearing foraminifer ooze
(20%) (80%)

Chemical sediments and diagenetic beds or nodules, including minerals formed by inorganic precipitation such as evaporites and many carbonates (e.g., packstone, rudstone, and grainstone) are classified according to mineralogy, texture, and fabric following the ODP classification (Mazzullo et al., 1988). For semilithified to lithified sediments, the suffix "-stone" is added to the principal names sand, silt, clay, or mud. The term "chalk" is used for partially lithified sediment composed of >60% calcareous nannofossils. Sediments composed of >60% siliciclastic and volcanic grains are classified as "volcaniclastic" if they contain a higher proportion of volcaniclastic than siliciclastic grains. The classification used for volcaniclastic sediments is described in "Physical Volcanology," p. 16.

X-Ray Diffraction

Relative abundances of the main silicate and carbonate minerals were determined semiquantitatively using a Philips model PW-1729 X-ray diffractometer with Cu Kα radiation (Ni filter). Each bulk-sediment sample was freeze-dried, crushed, and mounted with a random orientation into an aluminum sample holder. Instrument conditions were as follows: 40 kV, 35 mA, goniometer scan from 2° to 70° 2θ for bulk samples, step size 0.01° 2θ, scan speed at 1.2° 2θ/min, and count time 0.5 s. Peak intensities were converted to values appropriate for a fixed-slit width. An interactive software package (MacDiff 3.3.0 PPC) was used on a Macintosh computer to identify the main minerals. Most diffractograms were peak corrected to match the main calcite peak at 3.035 Å, except where quartz was present as a major component (major peak at 3.343 Å). In absence of both quartz and calcite, no peak correction was applied. Identifications were based on multiple peak matches, using the mineral database provided with MacDiff (Table T2).

T2. Positions of diagnostic peaks, p. 76.

Peak areas were measured only to estimate calcite/dolomite ratios. In all other cases, minerals were grouped as "major" or "trace" components depending on relative peak heights. It is not possible to reasonably estimate the proportions of clay minerals, glass, or amorphous opal with the bulk samples used for analysis; however, mixtures of these minerals with calcite comprise most of the analyzed samples. Relative abundances reported in this volume during Leg 183 are useful for general characterization of the sediments, but they are not precise quantitative data.

Smear Slides

Petrographic analysis of the sediment was primarily by smear-slide description. See the "Core Descriptions" contents list for tables summarizing data from the smear slides. These tables include information about the sample location, whether the sample represents a dominant (D) or a minor (M) lithology in the core, and the estimated percentage ranges of sand, silt, and clay, together with all identified components. We emphasize here that smear-slide analysis provides only crude estimates of the relative abundances of detrital constituents because the mineral identification of finer grained particles can be difficult using

only a petrographic microscope, and sand-sized grains tend to be underestimated because they cannot be incorporated into the smear evenly. The mineralogy of smear-slide components was validated by XRD. The relative proportions of carbonate and noncarbonate materials estimated from smear slides was validated by chemical analysis of the sediments (see **"Organic and Inorganic Geochemistry,"** p. 37).

Spectrophotometer

Reflectance of visible light from cores was routinely measured downhole using a Minolta Spectrophotometer (Model CM-2002) mounted on the archive multisensor track (AMST) (see **"Physical Properties,"** p. 31). The AMST measures the archive half of each core section. The purpose of measuring the visible light spectra was to provide a continuous stratigraphic record of color variations downhole for visible wavelengths (400–700 nm). Spectrophotometer readings were taken before cleaning the surface of each core section. The measurements were then automatically taken and recorded by the AMST, which permits measurements only at evenly spaced intervals along each core. Each measurement consists of 31 separate determinations of reflectance in 10-nm-wide spectral bands from 400 to 700 nm. Additional detailed information about measurement and interpretation of spectral data with the Minolta spectrophotometer can be found in Balsam et al. (1997; 1998; in press). During Leg 183, there was no way to program the AMST software to avoid taking measurements in void intervals in the cores or in disturbed areas of core with drilling slurry or biscuits. This produced many spurious measurements, which must be edited from the color data before use.

Warning: During the cruise and postcruise, it was determined that a large number, if not all, values measured with the spectrophotometer are in error. Whether these data can be restored to correct values or rendered otherwise usable is being assessed by ODP personnel. Users of these data should check with ODP database personnel before proceeding.

BIOSTRATIGRAPHY

ODP Leg 183 drilled two formerly united geological features, the Kerguelen Plateau and Broken Ridge, which rifted apart during the Eocene and now lie at rather different southern latitudes (~30°S and 45°–65°S latitude, respectively). As a consequence, for the calcareous microfossil groups examined on board ship (calcareous nannofossils and planktonic foraminifers), rather different zonations were applied for age-dating sediments in these two regions. For instance, for the Neogene interval, the nannofossil zonation given in the revised Cenozoic geochronology and chronostratigraphy of Berggren et al. (1995) and the temperate planktonic foraminiferal zonation of Srinivasan and Kennett (1981) were in general directly applicable for Broken Ridge but not for the Kerguelen Plateau, where higher latitude schemes worked out by previous workers in that area were more suitable. For this reason, two somewhat different zonations for the calcareous microfossil groups, one for Broken Ridge and the other for the Kerguelen Plateau, are presented for Neogene sediments drilled during this cruise (Figs. **F5** and **F6**, respectively). In these cases, we inserted the mid- or high-latitude zona-

F5. Neogene time scale and biostratigraphic datums used, **p. 59.**

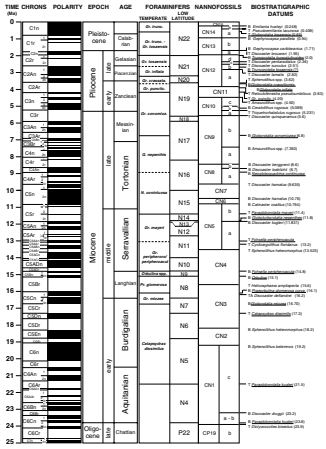

F6. Holocene through Late Cretaceous time scale and biostratigraphic datums used, **p. 61.**

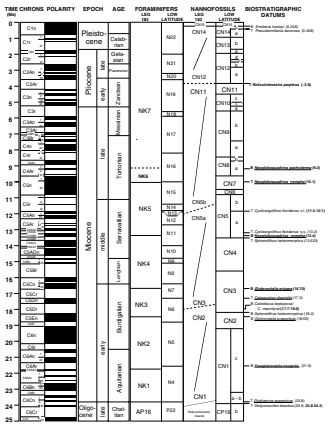

tions alongside the low-latitude schemes to aid in comparisons and interpretation.

In Figure F6, high-latitude species, groupings of species, or species concepts that are used for biostratigraphic datums are indicated in bold type to distinguish them from low-latitude datums (which are shown in plain type). The same is true of any differences in age calibrations between the high- and low-latitude datums. Foraminiferal biostratigraphic datums are underlined to distinguish them from nannofossil datums.

The shipboard palynomorph biostratigraphy was primarily concerned with nonmarine Cretaceous sequences. We discuss this separately below.

Preliminary age assignments made on board ship were based primarily on biostratigraphic analyses of calcareous planktonic microfossils from core-catcher samples, which were then supplemented as time permitted with additional samples taken within the cores. Estimates of biostratigraphic ages were calibrated against the magnetic polarity time scale of Cande and Kent (1995). As noted above, the time scale of Berggren et al. (1995) was applied to the Cenozoic where applicable. The time scale of Gradstein et al. (1994) was used for the Cretaceous. Age estimates for Cretaceous calcareous nannofossil datums traceable to the low latitudes were taken from Erba et al. (1995), which are calibrated by the Gradstein et al. time scale (1995). Cretaceous austral zonations are used where applicable for calcareous microfossils; however, none of these have yet been calibrated against the Gradstein et al. time scale, and, thus, their correlations with low latitude zonal schemes are highly tentative.

Calcareous Nannofossils

Biostratigraphy

For the Cenozoic, the nannofossil biostratigraphic framework was provided by the zonal schemes of Martini (1971; with modifications by Martini and Müller, 1986) and Bukry (1973, 1975; zonal code numbers added and modified by Okada and Bukry, 1980). As noted above, these schemes were applied directly for the Broken Ridge site but were condensed and/or modified as necessary for the Kerguelen Plateau sites, particularly for the Neogene, Oligocene, and Danian.

Pospichal et al. (1992) illustrated decreasing biostratigraphic resolution in nannofossil zonations from the low to high latitudes of the South Atlantic. The greatest loss occurs in the Neogene, where little stratigraphic control could be achieved between 51°S and 65°S. Wei and Wise (1992) summarized and calibrated to the paleomagnetic time scale a few usable Neogene high-latitude nannofossil datums detectable on the Kerguelen Plateau and elsewhere in the Southern Ocean. These are indicated on Figure F6 alongside the low-latitude zonation of Bukry for comparison, where they are labeled "Leg 183" and "Low Lat." respectively; in this figure the datums have been recalibrated for comparison with the Berggren et al. (1995) time scale (see discussion below). With so few datums, however, most Neogene nannofossil zones have had to be combined into about five total zones at these latitudes.

High-latitude nannofossil zonations with moderate resolution have been developed for the Oligocene to mid-middle Eocene (Wise, 1983; Wei and Wise, 1990; Wei and Thierstein, 1991), and these have been inserted into Figure F6. Ages for key datum levels have been calibrated in

the region of the Kerguelen Plateau against magnetostratigraphy by Wei (1992); these are indicated in bold type in Figure F6, where they have been recalibrated against the Berggren et al. (1995) time scale.

As noted by Wei (1992), biomagnetostratigraphic correlations at several Southern Ocean sites may show considerably different ages relative to those compiled from the mid-latitudes by Berggren et al. (1985, 1995). Where such differences exist, we have, in most instances, chosen to use ages derived from the high-latitude calibrations against the magnetostratigraphy. As noted above, where such ages differ from those in the lower latitudes, the high-latitude ages are shown in bold type in Figure F6 following the corresponding datum level (similarly, high-latitude biostratigraphic datums are also indicated in bold type). For major differences in age assignment, arrows indicate where on the chart a datum has been repositioned for proposes of this study.

As Pospichal et al. (1992) indicate, biostratigraphic resolution increases down column from the mid-Eocene through the Paleocene because global climates were warmer then, nannofossil diversities higher, and the zonations for that interval were largely defined in temperate rather than tropical regions. Thus, the standard zonal compilations of Martini and Bukry cited above can be applied with relatively few modifications, although subzones may not be discernible. Unfortunately, few sections for that interval from the Kerguelen Plateau are available for age calibration because of poor core recovery (mostly a result of the presence of cherts or condensed intervals) or to the lack of detailed paleomagnetic studies. Thus, the biomagnetostratigraphic high-latitude correlations for the mid-Eocene–Paleocene given by Wei (1992, fig. 3) are from Broken Ridge or the Atlantic sector of the Southern Ocean only. For this reason, we indicate in Figure F6 no changes in the calibrations of Berggren et al. (1995) for this part of the column. Wei and Pospichal (1991) do, however, provide a useful lower Paleocene Antarctic zonation based on ODP Holes 690C (Leg 113: Maud Rise) and 738C (Leg 119: southern Kerguelen Plateau). Their zonation (nannofossil Zones NA1–NA6) has been inserted into Figure F6 with our best estimate for correlations to the current paleomagnetic time scale. We note, however, that little detailed paleomagnetic work is available on their sections.

The nannofossil zonation employed for the Upper Cretaceous during Leg 183 is that of Watkins et al. (1996), a high-latitude scheme developed for the Southern Ocean based on DSDP/ODP drilling throughout this region. In Figure F6, high-latitude zones used during Leg 183 have been inserted alongside the low-latitude zonal scheme compiled by Sissingh (1977) ("CC" zones) as modified or embellished by Perch-Nielsen (1985a). As Watkins et al. (1996) point out, the upper part of their zonation has the highest resolution and reliability, but is based nearly exclusively on high-latitude taxa; thus, it is highly provincial. For instance, only one of the uppermost eight nannofossil datum levels can be correlated directly to the low or mid-latitudes because of the marked endemism that characterizes the assemblages and biostratigraphic datums. Huber and Watkins (1992) discuss paleoceanographic scenarios that may account for this circumstance. On the other hand, there is some paleomagnetic control for this part of the Cretaceous section, and trial correlations with magnetic stratigraphy based primarily on ODP Site 690 in the Weddell Sea are indicated in Figure F6. We have also been guided in part by the correlation charts of Southern Ocean datums compiled by Cita et al. (1997). All of these correlations are highly tenta-

tive, however, and will be revised to the extent possible based on shore-based research on the Leg 183 materials.

Below the Campanian, the Upper Cretaceous zonation of Watkins et al. (1994) becomes more cosmopolitan in character, with more direct ties to low-latitude nannofossil zonations. No useful correlation with magnetostratigraphy is possible, however, because of the presence of the long Cretaceous normal superchron. Correlations with European stratotype stages in many cases are only approximate, particularly for the high-latitude index taxa; some of this uncertainty is indicated by the dashed zonal boundary lines and question marks attached to high-latitude biostratigraphic datums. Only their relative positions in the succession are known at this time.

The Lower Cretaceous (Albian) Austral zonation considers primarily the high-latitude zones of Wise (1983) within the context of the cosmopolitan nannofossil zonation by Bralower (1992; see also Bralower et al., 1993, 1995, and the more recent compilation by Bown et al., 1998). These authors include the "NC" zonal numbering scheme initiated by Roth (1978). None of these zonal schemes, however, have previously been calibrated against the Gradstein et al. (1995) time scale; thus, their correlation here with that chronology is only approximate.

Methods

Calcareous nannofossils were examined using standard light microscope techniques, under crossed polarizers, transmitted light, and phase contrast light at 1000× magnification. Preservation and abundance of calcareous nannofossil species may vary significantly because of etching, dissolution, or calcite overgrowth. It is not uncommon to find nearly pristine specimens occurring in the same sample as specimens exhibiting overgrowth or etching. Thus, a simple code system to characterize preservation has been adopted and is listed below:

VG = very good preservation (no evidence of dissolution and/or overgrowth; no alteration of primary morphological characteristics, and specimens appear diaphanous; specimens are identifiable to the species level);
G = good preservation (little or no evidence of dissolution and/or overgrowth; primary morphological characteristics only slightly altered; specimens are identifiable to the species level);
M = moderate preservation (specimens exhibit some etching and/or overgrowth; primary morphological characteristics sometimes altered; however, most specimens are identifiable to the species level); and
P = poor preservation (specimens are severely etched or exhibit overgrowth; primary morphological characteristics largely destroyed; fragmentation has occurred; specimens cannot be identified at the species and/or generic level).

Six calcareous nannofossil abundance levels are recorded as follows:

V = very abundant (10–100 specimens per field of view);
A = abundant (1–10 specimens per field of view);
C = common (1 specimen per 2–10 fields of view);
F = few (1 specimen per 11–100 fields of view);
R = rare (1 specimen per 101–1000 fields of view); and
B = barren.

Planktonic Foraminifers

Biostratigraphy

High-latitude planktonic foraminifer faunas, as observed by previous workers during DSDP/ODP drilling (Berggren, 1992a, 1992b; Huber, 1990, 1991, 1992; Stott and Kennett, 1990; Quilty, 1992; Krashenninikov and Basov, 1983; Sliter, 1977), typically exhibit low diversity and high dominance, and, thus, many of the key index species useful for biostratigraphic correlation at low latitudes are absent. Cretaceous and Cenozoic zonal schemes developed specifically for the subpolar Southern Ocean regions have, therefore, been applied to all Kerguelen Plateau pelagic sediment sections. Figure **F6,** shows approximate correlations between high-latitude provincial ("Leg 183") planktonic foraminiferal and tropical ("Low Lat.") zonations.

In contrast to the low-diversity assemblages encountered on the Kerguelen Plateau, Neogene planktonic foraminifers recovered from Site 1141 on Broken Ridge (32.2°S) are diverse and show affinities with subtropical regions as well as with the Southern Ocean. At this site we were, therefore, able to employ a more detailed temperate planktonic foraminifer zonation based on a largely different suite of planktonic foraminifers.

Cenozoic

Berggren's (1992) Neogene Kerguelen zonal scheme is used for Miocene planktonic foraminifers, and the Antarctic Paleogene (AP) zonal scheme of Stott and Kennett (1990; modified by Huber, 1991, and Berggren, 1992) is applied to the Paleocene–Oligocene sections. In descriptions of the fauna at Broken Ridge, we refer to the temperate planktonic foraminifer zonation of Srinivasan and Kennett (1981), which is based on the Austral Cenozoic zonation of Jenkins (1971; see also Jenkins and Srinivasan, 1986, and Kennett and Srinivasan, 1983). The generic classification of Kennett and Srinivasan (1983) is used throughout the Neogene. For most of the Paleogene, we base our taxonomic concepts on the work of Tourmarkine and Luterbacher (1985), and refer to Jenkins' (1971) and Berggren's (1992) discussions on the classification of Austral and high-latitude forms. For Paleocene and early Eocene forms, taxonomic usage has been modified according to Olsson et al. (1999).

Mesozoic

Zonation of Upper Cretaceous sections (Maastrichtian–Turonian) is based on Cita et al.'s (1997) Upper Cretaceous biostratigraphy for the Southern Ocean. We modified this scheme during Leg 183 drilling within the original framework of Huber's (1992) Upper Cretaceous Austral realm zonal scheme. The rather impoverished Lower Cretaceous planktonic foraminiferal fauna, encountered for the first time on the Kerguelen Plateau at Site 1136, was compared to Albian assemblages from the Falkland Plateau (DSDP Sites 327 and 511) described by Sliter (1977), Krasheninikov and Basov (1983), and Bralower et al. (1993), within the framework of the mid-Cretaceous zonal scheme of Leckie (1984). Our generic classification follows that of Caron (1985).

Methods

Core-catcher samples of ~20 cm^3 (plus additional samples where necessary) were soaked in 3% hydrogen peroxide with a small amount of Calgon added, warmed on a hot plate and desegregated by washing in tap water over a 63-µm mesh sieve. Each sieve was dipped in a solution of methyl blue dye to identify contaminants from previous samples. All samples were dried over a hot plate at ~50°C. The dried samples were examined under a binocular microscope and planktonic foraminifer faunal composition was recorded in nonquantitative terms based on an assessment of forms observed in a random sample of 200–400 specimens from the >63-µm size fraction. Relative abundances were reported using the following categories:

A = Abundant (30%);
C = Common (15%–30%);
F = Few (3%–15%);
R = Rare (2%–3%); and
T = Trace (<1.5%).

Preservation of planktonic foraminifer assemblages was recorded as

G = Good (> 90% of the specimens unbroken with only minor evidence of diagenetic alteration);
M = Moderate (30%–90% of specimens having broken chambers and or showing signs of dissolution); and
P = Poor (sample dominated by specimens with fragmented and/or strongly dissolved tests).

Palynology

The main interest for palynomorph studies during Leg 183 was the Cretaceous terrestrial palynoflora, which records the advent and radiation of angiosperms during the early Albian in Antarctica. The relatively fast dispersal of angiosperms during the Late Cretaceous provides insight into the biological and geological evolution of the Southern Hemisphere, especially for the pattern of Gondwana fragmentation.

The time calibration employed here is based on data from ODP Legs 113 and 120 by Mohr and Gee (1992). Dinoflagellate-based palynostratigraphy will also be used to improve marine biostratigraphic correlations.

To concentrate the organic material, samples were first treated with 10% HCl to dissolve out carbonates. After several washings and centrifuging, high-strength HF was added to dissolve silicates. After further washing and centrifuging, the concentrated material was sieved with 20-µm sieves. Samples were mounted on slides, using glycerin jelly and wax.

Preliminary analyses were performed only on core-catcher material. The shipboard results do not represent the total palynomorph content of the sediments.

The following abundance categories of total palynomorphs per sample were used:

A = abundant (> 20 palynomorphs);
C = common (10–20 palynomorphs);

O = occasional (5–10 palynomorphs);
P = present (<5 palynomorphs); and
B = barren.

Diatoms

Fossil diatoms were used sparingly to provide age dates for Neogene siliceous sections where little or no biostratigraphic control could be provided by calcareous microfossils. For this purpose, the biostratigraphic zonation of Harwood and Maruyama (1992) as modified and calibrated to the time scale of Berggren et al. (1995) for Leg 178 (Shipboard Scientific Party, 1999b) was followed, using smear slides prepared from raw sediment. That zonal scheme, which extends down to the middle Miocene, is shown in Figure F7. Below the middle Miocene, we referred to the zonation of Harwood and Maruyama (1992) as calibrated by datums compiled for Leg 177 by Gersonde, Hoddell, Blum, et al. (1999). Also useful were species ranges compiled by Gersonde, Hoddell, Blum, et al. (1999) shown in Figure F8.

F7. Holocene to middle Miocene diatom zones and datums used, p. 68.

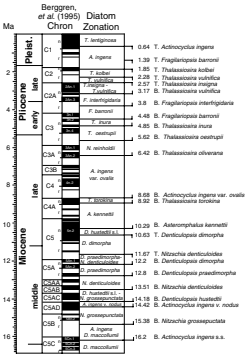

F8. Diatom zonation, p. 69.

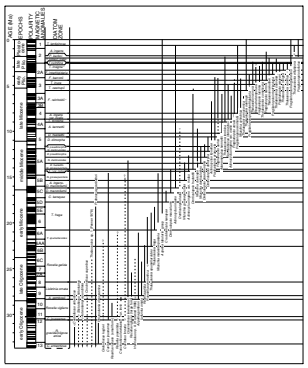

Silicoflagellates

Silicoflagellates are most commonly preserved in diatomites underlying modern or ancient ocean upwelling areas or in diatomites preserved by nearby volcanism. The investigation of silicoflagellates often allows the dating of sediment from high-latitude areas, where calcareous micro- and nannofossils are missing or nondiagnostic. It also allows some conclusions as to the paleoenvironmental conditions under which the sediments were deposited.

Smear slides of unprocessed material provided the simplest way to obtain an initial overview of the occurrence and abundance of silicoflagellates. For more detailed work, we processed samples.

Silicoflagellates usually make up only a small proportion of the siliceous microfossils in a sediment sample. Therefore, the preparation technique should concentrate the siliceous material. On board ship, we placed core catcher in beakers and treated them first with a few drops of hydrogen peroxide to desegregate the sediment and to remove the organic carbon. Then 10% HCl in various volumes (depending on the type of sediment and the percentage of calcium carbonate) was added to dissolve most of the carbonate. The residue was washed, centrifuged, and decanted. This procedure was repeated a minimum of three times. Samples were then strewn on a slide, covered with a 22 mm × 30 mm cover slip, and mounted using Norland 61 mounting media. To determine the abundance of silicoflagellates, all specimens that consisted of more than half a skeleton were counted.

The silicoflagellate zonation followed was that utilized by McCartney and Wise (1990) and McCartney and Harwood (1992). The compilation by Perch-Nielsen (1985b) was also helpful.

PHYSICAL VOLCANOLOGY

The physical volcanologists on board the *JOIDES Resolution* during Leg 183 sought to determine the types of eruptive activity that formed the volcanic rocks and volcaniclastic sediments recovered in the cores. This was accomplished by describing the rocks and identifying features that are diagnostic of specific physical processes to produce an inte-

grated picture of the style of volcanism and environmental setting of each site drilled. Additional information presented in "Lithostratigraphy," "Igneous Petrology," "Downhole Measurements," and "Alteration and Weathering" of each site chapter were particularly important in producing the final interpretation.

Volcaniclastic Sediments

We define volcaniclastic sediments as containing >60% siliciclastic and volcaniclastic grains and <40% biogenic material and a higher proportion of volcaniclastic than siliciclastic grains. This class includes epiclastic sediments, the volcanic detritus produced by erosion of volcanic rocks by wind, water, and ice; pyroclastic deposits, the products of the explosive degassing of magmas; and hydroclastic sediments, the products of granulation by steam (phreatic) explosions and quenching (hyaloclastite and peperite). Note that because this definition includes epiclastic sediments, it does not imply any active volcanism at the time of deposition.

The subclassification of volcaniclastic sediments followed by shipboard scientists during Leg 183 differs from the standard ODP classification (Mazzullo et al., 1988) in that we adopt a descriptive (nongenetic) terminology similar to that employed during Leg 157 (Gran Canaria and Madeira Abyssal Plain). Unless a pyroclastic origin for sediments can be defined, clasts of volcanic provenance (volcaniclastic) are described according to the classification scheme for siliciclastic sediments, noting the dominant composition of the volcanic grains. We follow the siliciclastic textural classification of Wentworth (1922) to separate the various volcanic sediments and sedimentary rocks into volcanic gravel (grain size = >2 mm), volcanic sand (2–0.0625 mm), volcanic silt (0.0625–0.0039 mm), and volcanic clay (<0.0039 mm). For unsorted or poorly sorted volcaniclastic sediments, such as those characterized by debris flows, we apply the terms volcanic breccia (angular clasts) or volcanic conglomerate (rounded clasts) and use modifiers to describe the sediment further.

Volcanic sediment can be classified by designating a principal name and major and minor modifiers. The principal name of a granular sediment defines its sediment class (e.g., sand, silt, or clay). Relative proportions of the vitric (glass), crystal (mineral), and lithic (rock fragment) components of the sediments are expressed as major (25%–40%) and minor (10%–25%) modifiers in the name. The major modifiers are placed before the principal name and minor modifiers are placed after the principal name using "with." For example, volcanic sand composed of 45% glass, 35% feldspar crystals, and 20% lithic fragments is named a crystal vitric volcanic sand with lithic fragments. Volcanological features are recorded on both sediment and hard-rock VCD (HRVCD) forms (see the **"Core Descriptions"** contents list). Detailed systematic information was recorded on a separate volcaniclastic sediment description log (Table **T3**). Volcanic breccias/conglomerates were further characterized using a point counting grid (Moore et al., 1996), and these data were recorded on the volcaniclastic breccia/conglomerate grid information log (Table **T4**).

Where there was evidence for a pyroclastic origin, volcanologists followed the classification of Fisher and Schmincke (1984), as adopted by Mazzullo et al. (1988), that uses the names volcanic breccia (>64 mm), lapilli (lapillistone; 2–64 mm), and ash (tuff; <2 mm).

T3. Volcaniclastic sediment description sheet, **p. 77.**

T4. Volcaniclastic breccia grid information, **p. 78.**

Sedimentary structures including graded bedding, cross-bedding, planar laminations, foreset bedding, dune forms, ripples, and any evidence of agglutination, welding, or rheomorphism are recorded on the volcaniclastic sediment description log (Table T3).

Lava Flows

General

The physical description of lava during Leg 183 was a multistage process. Unit boundaries and lithologic descriptions were selected first. The lithologic descriptions are presented in the "Igneous Petrology" section of each chapter. A general description of the volcanological features within the flows was compiled. After this, individual units were examined in detail. Often, time did not permit detailed examination of all the units, and only a selected subset was subjected to full scrutiny. Finally, an attempt was made to synthesize the observations from the different units, combining data from sections such as "Igneous Petrology" and "Downhole Measurements." The descriptions and interpretations were checked during the sampling for shore-based studies. This examination was particularly useful for comparison between different sites.

The site chapters start with a description of each unit using nongenetic terminology. Phrases such as "chill zone" or "flow-top breccia" are generally avoided since they are interpretations. This descriptive part is followed by a unit-by-unit interpretation, with explanations of the criteria used to separate the different units. For most readers, it may be helpful to first read the interpretive section and refer to the unit descriptions in conjunction with the core photographs for the observations leading us to these interpretations.

Methodology

The first step in describing the core (selection of unit boundaries) required considerable interpretation of the rocks. As a result, the initial justification for placing these boundaries sometimes shifted or evaporated as our understanding of the site improved. Also, the unit boundaries reflect major physical changes in the core (e.g., brecciated vs. massive) that were visible in the physical properties and downhole measurements. More subtle boundaries were usually not broken out, despite their possible significance to the volcanological interpretation. Finally, when the precise location of the boundary could not be determined in the initial examination, an arbitrary decision was required for the core description to proceed. Rarely did we later make changes to the unit boundary locations when additional observations were gathered. Thus, although a strong effort was made to have unit boundaries reflect individual lava packages, the term "unit" should not be considered synonymous with "lava flow" in this volume.

General observations were made during the initial description of the rocks. We first noted intervals of breccia and coherent lava and gross changes in vesicularity. We then characterized clasts in the breccias using the same techniques as sedimentologists (clast size, shape, sorting, and lithology). We also noted the volume fraction and type of matrix (commonly none or only secondary alteration minerals) and the abundance of finer lava fragments. Of particular interest was the presence (or absence) of features diagnostic of brecciation while the lava was hot. These include clasts engulfing fragments of other (earlier) clasts, weld-

ing, glassy margins surrounding the clasts, extensions of the interior of the flow into the breccia, entrained clasts within the interior of the flow, and the presence of a basal breccia. Changes in the abundance and morphology of vesicles were used to identify clasts of different lithologies within the breccia.

The second more systematic description of units concentrated on documenting vesicle features by recording (1) volume percentage, (2) size range (maximum, minimum, and average diameters), (3) number density, (4) shape (sphericity and angularity), and (5) grading (fining up or coarsening up) of the vesicles at intervals appropriate for the variability shown in the core (typically every 1–30 cm). This information is recorded on a separate vesicle description log (Table T5) (see the "Supplementary Materials" contents list). The volume fraction of vesicles was estimated using visual percentage estimate charts that provided examples at 1%, 2%, 3%, 5%, 7%, 10%, 15%, 20%, 25%, 30%, 40%, and 50%. The reported values are only accurate to ±1 of these steps. Thus, a reported value of 10% indicates a 2-σ confidence that the actual value is between 7% and 15%. In a few locations, these visual estimates were supplemented by measurements using a binocular microscope. Lines covering ~50 cm of the core were examined, and the fraction of the length of these lines that intersected vesicles provided a more quantitative vesicle abundance. The measurement of maximum and minimum vesicle sizes was straightforward, though vesicles <0.1 mm were usually not visible. The average vesicle size is a measure of what appeared to be a typical vesicle. It is subjective, but provides a measure for whether the vesicle size distribution is skewed toward the small or large end of the size range. Number density was determined by counting the number of vesicles in a given area. The size of the measurement area changed depending on the density of vesicles but, in general, was large enough to contain 20 to 100 vesicles. Because vesicle number density varied by ~5 orders of magnitude in the rocks recovered during Leg 183, the measurement areas ranged from 0.25 to 500 cm^2. Angularity and rounding were estimated using the charts produced for describing sedimentary rocks. During these measurements, notes were also taken on the presence of mesostasis blebs, orientation of elongated vesicles, changes in groundmass texture, and other features.

T5. Vesicle description sheet, p. 79.

For the breccias, the more intensive measurements included determination of the percentages of clasts in size categories of >1, 0.1–1, and <1 cm, as well as void space. The margins of clasts were also subjected to more careful examination to characterize the brecciation process.

Finally, during the synthesis of the various data sets, we estimated the thickness of the various units and flows. It is very important to note that ODP curation procedures assume that the top of recovered material is from the top of the cored interval. This can lead to large (up to 9 m) differences between the curated depth and the actual depth. During Leg 183 there were several occasions in which the pattern of rock recovery and selection of unit boundaries combined to maximize these problems. Unit thicknesses derived from curated depths alone must be considered accurate to only ±5 m. Downhole measurements were required to produce more accurate estimates of flow thicknesses.

Interpretation

The interpretation of the lavas involved three steps. The observed features were tied to physical processes, the emplacement style of indi-

vidual flows was inferred, and the environmental setting (e.g., subaerial or submarine) for the whole sequence was discussed. Interpretations relied most heavily on observations from active volcanism in Hawaii and the ~15-Ma flood basalts of Columbia River Basalt Group, in the United States.

Traditionally, mafic lava flows have been divided into pahoehoe and aa flows (Macdonald, 1953). This division is important because aa and pahoehoe flows are emplaced in fundamentally different styles. Aa flows disrupt and mix their upper crusts, which move like the treads on a bulldozer. Pahoehoe flows advance by inflating a lobe with a continuous crust, much like filling a rubber balloon with water. However, there is also a wide range of intermediate flow types. Most transitional flow types have "pahoehoe" in their names (e.g., slab pahoehoe, remobilized pahoehoe, toothpaste pahoehoe, and sharkskin pahoehoe), but many are more similar to aa than to pahoehoe. The most common transitional flow type found during Leg 183 has a flow-top breccia composed of broken pieces of pahoehoe. This type of flow has not been seen in Hawaii and has no widely accepted name.

Determining lava type is relatively straightforward if centimeter-scale morphologic features of the flow tops and bottoms are well preserved and recovered. Aa flows are characterized by angular, spinose clinker at both the flow tops and bottoms, and pahoehoe flows are characterized by smooth tops and bottoms. Transitional flows show some of the characteristics of both aa and pahoehoe lava flows. However, these types of features are the first to be destroyed by erosion and weathering and are also difficult to recover in core.

It is commonly possible to use the distribution and morphology of vesicles in the interior of the flow to determine the flow type (Fig. F9). Most lava flows have a thick vesicular upper crust, a dense core, and a thinner vesicular lower crust (Aubele et al., 1988). To avoid confusion with the drilled core, we use the term "massive interior" instead of "core" throughout this volume. Aa flows tend to have fewer, but more distorted vesicles than pahoehoe flows (Macdonald, 1953). Aa flows also commonly exhibit partially resorbed pieces of entrained crust within the dense interior of the flow. These typically appear as fist-sized clots of small, highly distorted vesicles within the nonvesicular part of the flow. Aa flows also commonly have 10- to 200-cm-wide "arms" or "fingers" of dense material pushed up into the vesicular, brecciated crust. The margins of these arms have been observed to disaggregate into sand-sized and finer fragments as they cool (L. Keszthelyi, unpubl. data).

For pahoehoe flows, we use the terminology from Self et al. (1997). Key vesicle features are horizontal vesicular zones in the upper crust, horizontal vesicle sheets defining the boundary between the upper crust and the massive interior of the flow, and pipe vesicles at the base. Pipe vesicles are typically 0.3–0.7 cm in diameter, 3–15 cm in height, and reliable indicators of a flow margin. Pipe vesicles may grade into vesicle cylinders, which in turn lead to 0.5- to 5-cm-thick horizontal vesicle sheets at the base of the upper vesicular crust. The vesicles within cylinders and sheets are usually 1–5 mm in size and are very irregular in shape. The vesicle cylinders and vesicle sheets are usually found in segregated late-stage differentiates that can have micropegmatite textures (e.g., Goff, 1996). These features are synonymous with segregation veins. However, they are very different from the horizontal vesicular zones that can be found in the upper crust of pahoehoe flows. These zones can vary in thickness from 0.5 to 500 cm and typically con-

F9. Drawing of cross sections of aa and pahoehoe lava flows, p. 70.

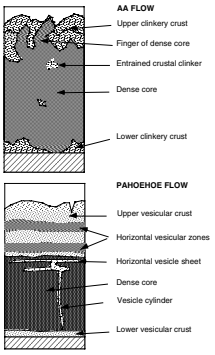

tain vesicles 0.5–5 cm in size. Commonly, they are marked by relatively sharp upper boundaries and fade gradually into a zone of relatively low vesicularity. Bubble sizes usually fine downward across this transition. The vesicles in the uppermost 1–10 cm and lowermost 10–50 cm of a pahoehoe flow are usually relatively small (0.1–3.0 mm in diameter) and highly spherical.

The interpretation of these vesicle features is explained at length in Self et al. (1997, 1998), but we provide a short synopsis here. The vesicles in the upper and lower crust represent bubbles formed during eruption. When the injection of fresh lava into the flow stops, the bubbles rapidly rise to the base of the upper crust, leaving a dense interior. Horizontal vesicular zones represent episodes of reactivation of the flow, whereas horizontal vesicle sheets and vesicle cylinders can only form in a stagnant lava.

This model allows the duration of active flow in an inflated pahoehoe flow to be estimated. The thickness of the upper vesicular crust is interpreted as a direct measurement of the amount of lava that solidified while fresh lava was being injected into the flow. A cooling model allows the translation of this thickness into time. We estimate the duration of active flow using the Hon et al. (1994) empirical cooling model as adopted by Thordarson (1995). This technique and its limitations and errors are described in more detail in Self et al. (1997, 1998).

Given the abundance of flows with brecciated flow tops recovered during Leg 183, the processes that disrupt lava require some additional explanation. Aa clinker forms primarily by the rupture of molten lava. This can only happen when and where strain rates are high and/or the viscosity of the fluid lava is high (Peterson and Tilling, 1980). This tearing of the lava is a result of the non-Newtonian behavior of lava under these conditions. Large "arms" of lava from the dense interior of the flow commonly extend into the breccia, especially along well-defined shear zones. Entrainment of the brecciated top into the interior of the flow is a powerful heat loss mechanism for aa flows (Crisp and Baloga, 1994), driving increased rapid crystallization of the flow interior (Crisp et al., 1994) and leading to effective degassing.

Transitional lavas in Hawaii fall into two broad categories. Lavas such as toothpaste or sharkskin pahoehoe involve emplacement of highly viscous lavas at very low strain rates (Rowland and Walker, 1987). These flows do not form brecciated tops. The other category of transitional lava is slab pahoehoe, which involves emplacement of relatively low viscosity lava under very high strain rates (Peterson and Tilling, 1980). Such high strain rates are usually not sustained and are, instead, associated with surges of lava. Also, high strain rates are associated with higher volumetric flux and larger, sheet-like, lobes. The crust on the flow at the time of the surge (typically flat slabs from the top of larger sheetlike pahoehoe lobes) is disrupted and rafted along. Jumbled piles of crustal slabs accrete wherever there are obstacles or constriction in the flow. The individual clasts usually demonstrate the full range of brittle to ductile deformation as the upper chilled portion cracks and the lower hotter portion deforms plastically to the disruption. Slab pahoehoe lavas rarely extend for >1 km before transitioning to classic aa or pahoehoe.

Another style of brecciation was observed during the Mauna Ulu eruption of Kilauea Volcano, Hawaii. Within <12 hr, pahoehoe sheet flows became disrupted and brecciated by the intrusion of new lava into the interior of the flow and remobilized the entire upper surface. In Hawaii, this kind of extreme inflation was observed only in the near-

vent facies, where sudden pulses in eruption rate could be immediately transferred into a flow without a longer transport system to buffer the surges (Peterson and Tilling, 1980). However, surges disrupted the pahoehoe surfaces of flows from Laki (Iceland) >50 km from the vent (Th. Thordarson, pers. comm., 1995).

Lava flows that entered water (or were erupted subaqueously) may form pillow basalts, hyaloclastites, and peperites. The latter two are volcaniclastic sediments that form by quench fragmentation. Pillow basalts can usually be distinguished from pahoehoe flows by the thicker glass rinds, lower vesicularity, and the presence of marine sediments between the pillows. However, larger subaqueous flows may form massive sheets. The morphology of submarine flows is apparently controlled by local flow rate that is primarily a function of slope and eruption rate (Gregg and Fink, 1995).

IGNEOUS PETROLOGY

Core Curation and Shipboard Sampling

To preserve important features and structures, core sections containing igneous rocks were examined prior to splitting. Each piece was numbered sequentially from the top of the core section and labeled on the outside surface. Pieces that could be fitted together were assigned the same number and were lettered consecutively (e.g., 1A, 1B, and 1C). Plastic spacers were placed between pieces with different numbers. The presence of a spacer may represent a more substantial interval of no recovery than that represented by the spacer. If it was evident that an individual piece had not rotated about a horizontal axis during drilling, an arrow was added pointing to the top of the section. The pieces were split with a diamond-impregnated saw so that important compositional and structural features are preserved in the archive and working halves.

Nondestructive physical properties measurements, such as magnetic susceptibility and natural gamma-ray emission, were made on the core before it was split (see **"Physical Properties,"** p. 31). After the core was split and described, the working half was sampled for shipboard physical properties, magnetic studies (see **"Paleomagnetism,"** p. 27), thin sections, XRD, and XRF studies. The archive half was described on the HRVCD form and was photographed before storage. To minimize contamination of the core with Pt-group elements and Au, describers removed jewelry from hands and wrists before handling.

Visual Core Descriptions

We used HRVCD forms to document each section of the igneous rock cores (see the **"Core Descriptions"** contents list). The left column on the form, adjacent to the core photograph, represents the archive half graphically. A horizontal line across the entire width of the column denotes a plastic spacer. Oriented pieces are indicated on the form by an upward-pointing arrow to the right of the piece. Location of samples selected for shipboard studies are indicated in the column headed "Shipboard Studies" with the following notation: XRD = X-ray diffraction analysis; XRF = X-ray fluorescence analysis; TS = petrographic thin section; PP = physical properties analysis; and PM = paleomagnetic analysis.

We subdivided the core into consecutively numbered lithologic units (mostly representing single lava flows) on the basis of changes in color, structure, grain size, and mineral occurrence and abundance. Some units were divided into subunits (A, B, C, and so forth) because of uncertainty as to the number of individual flows involved or to bring attention to major internal divisions within a flow. Breccia or mylonite zones within units led to subdivision into, for example, A, B (brecciated zone), and C subunits. Larger intercalated sediment horizons were designated as independent lithologic units.

Written descriptions accompany the schematic representation of the core sections. This information includes

1. The leg, site, hole, core, type, and section number (e.g., 183-1135A-15R-3).
2. The unit number (consecutively downhole), the rock name (see below), and the number of pieces. Additional detailed descriptions of igneous lithology are reported in the hard-rock core description log.
3. Contact relations with neighboring lithologic units.
4. Phenocrysts: the types of minerals visible (with a hand lens or binocular microscope), their distribution within the unit, and, for each phase, its abundance (in volume percent), size range (in millimeters), shape, degree of alteration, and further comments if appropriate.
5. Groundmass texture and grain size: glassy, aphanitic, fine grained (<1 mm), medium grained (1–5 mm), or coarse grained (>5 mm). Grain size changes within units were also noted.
6. Vesicles: abundance (nonvesicular = <1%, sparse = 1%–5%, moderate = 5%–20%, high >20% by volume), distribution, size, shape, and mineral linings and fillings. Additional detailed descriptions of vesicle distribution through units are reported in **"Physical Volcanology,"** p. 16.
7. Color name and code (for the dry rock surface) according to the Munsell color charts.
8. The rock structure: whether the unit is massive, flow-banded, brecciated, scoriaceous, pillowed, hyaloclastic, or tuffaceous. Note that we generally did not distinguish between syn- and postemplacement brecciation of the lava flows.
9. Alteration: the alteration was graded as fresh (<2% by volume alteration products), slight (2%–10%), moderate (10%–40%), high (40%–80%), very high (80%–95%), or complete (95%–100%). Changes of alteration through a section or a unit were also noted. Additional detailed descriptions of alteration and weathering of igneous units are reported in **"Alteration and Weathering,"** p. 25.
10. The presence of veins and fractures, including their abundance, width, mineral linings and fillings, and, where possible, their orientation. Additional detailed descriptions of vein materials are reported in **"Alteration and Weathering,"** p. 25.
11. Additional comments, including notes on the variability of the unit.

We assigned provisional rock names on the basis of hand-specimen observation (hand lens and binocular microscope) and later checked these with thin-section studies and XRF major element analyses, where necessary. Porphyritic rocks were named by phenocryst type, using min-

eral names in order of decreasing abundance. The term "phenocryst" was used for a crystal that was significantly larger (typically at least five times) than the average size of the groundmass crystals. Many porphyritic basalts recovered during Leg 183 exhibited a range of crystal sizes (seriate texture), making estimation of phenocryst populations approximate. Descriptors were defined as follows:

Aphyric: phenocrysts constitute <1% by volume of the rock,
Sparsely phyric: phenocryst content ranges between 1% and 2%,
Moderately phyric: phenocryst content ranges between 2% and 10%, and
Highly phyric: phenocryst content exceeds 10%.

These descriptors were further modified by including the names of phenocryst phases, in order of decreasing abundance. Thus, a "highly olivine-plagioclase phyric basalt" contains more than 10% (by volume) phenocrysts, the dominant phenocryst being olivine, with lesser amounts of plagioclase. The prefix includes all of the phenocryst phases that are in the rock, as long as the total content exceeds 1%.

Thin-Section Descriptions

We examined thin sections to complement and refine the hand-specimen observations. In general, the same terminology was used for thin-section descriptions as for the VCDs. The percentages of individual phases, either estimated visually or determined by point counting, and textural descriptions are reported in "Thin Sections" (see the **"Core Descriptions"** contents list). The textural terms used are defined in MacKenzie et al. (1982). For some porphyritic basalts, the thin section and visual core descriptions differ slightly, typically because small plagioclase laths in a rock with seriate texture are visible only in thin section. Thus, a rock visually described as olivine-plagioclase-phyric may be plagioclase-olivine-phyric according to the thin-section description. Because not all units were examined in thin section, this discrepancy has been accepted and retained to maintain consistency of the visual records. Where possible, plagioclase compositions were estimated optically using the Michel-Levy Extinction Angle Method from at least 10 separate crystals.

X-Ray Fluorescence Analysis

We selected representative samples of major lithologic units and samples with specific characteristics for shipboard XRF analysis. Large pieces (~20 cm^3) were reduced to smaller fragments (<1 cm in diameter) by crushing between two disks of Delrin plastic in a hydraulic press. The sample was then ground for ~5 min in a Spex 8510 shatterbox with a tungsten carbide barrel. Contamination of the samples with Nb during grinding was investigated before the start of Leg 152, and none was detected at that time (Larsen, Saunders, Clift et al., 1994).

We used a fully automated wavelength-dispersive ARL8420 XRF system equipped with a 3-kW generator and a Rh-anode X-ray tube to determine the major and trace element abundances in the samples. Analytical conditions used are given in Table **T6.** The spectrometer was calibrated using a suite of 30 well-analyzed reference standards. The values recommended by Govindaraju (1989) were used for all elements ex-

T6. Instrument conditions during XRF analyses, **p. 80.**

cept for Zr and Nb. A subset of the standards, with concentrations recommended by Jochum et al. (1990), was used for these two elements. Precision estimates, based on replicate shipboard analyses of the USGS reference standard BHVO-1, are given in Table T7 (major elements) and Table T8 (trace elements). Several mechanical failures of the instrument produced a hiatus in analyses after Site 1138 samples, requiring recalibration, so we report statistics for analyses before and after this interruption. Precision for Ba and Ce decreased significantly during the Site 1138 sample analyses, so abundances for these elements are not reported in that chapter. Variability in the measured standard Nb abundance also increased, so for this period we corrected the measured unknown Nb by a normalization factor (measured Nb/accepted Nb for BHVO-1).

T7. Major element analytical precision determined during Leg 183, p. 81.

T8. Trace element analytical precision determined during Leg 183, p. 82.

We analyzed major elements using fused lithium tetraborate glass disks doped with lanthanum oxide as a heavy absorber (Norrish and Hutton, 1969). The discs were prepared from 600 mg of rock powder that had been ignited for 2 hr at ~1025°C and mixed with 7.2 g of dry flux consisting of 80% lithium tetraborate and 20% lanthanum oxide. This mixture, with 20 mL of LiBr (8.6M) added to prevent adhesion to the Pt-Au crucible, was then melted in air at 1150°C for ~4 min with constant agitation to ensure thorough mixing and then cooled. The 12:1 flux:sample ratio and the use of the heavy absorber makes matrix effects insignificant over the normal range of igneous rock compositions. Hence, the relationship between X-ray intensity and element concentration is linear. Iron contents are reported as Fe_2O_3 as a consequence of oxidation during the fusion process. We measured loss on ignition from weighed powders heated for 4 hr at 1025°C, then reweighed. CO_2 and H_2O contents were determined with a Carlo Erba NA 1500 analyzer.

We determined trace elements using pressed-powder pellets. These were made by mixing 5 g of rock powder with 30 drops of a solution of Chemplex polymer in methylene chloride (100 mg/cm^3) and then pressing the mixture into an aluminum cap under a load of 8 T. A pellet made with 5 g of basalt powder should appear infinitely thick to the shortest wavelengths used in the analysis. X-ray intensities were corrected for line overlap and interelement absorption effects. The latter corrections were based on the relationship between mass absorption coefficient and the intensity of the Rh-Kα Compton scatter line (Reynolds, 1963, 1967; Walker, 1973).

ALTERATION AND WEATHERING

All igneous rocks recovered during Leg 183 have undergone secondary alteration or weathering in subaerial, shallow subaqueous, or deep marine environments. Many features of low-temperature hydrothermal alteration (both submarine and subaerial) and subaerial weathering appear similar and are difficult to distinguish in the drilled core. In these descriptions, alteration is defined as the chemical transformation of mineral assemblages caused by interaction with hydrothermal fluids. Weathered materials differ from altered materials in that they form at the Earth's surface at ambient temperatures and pressures and are affected by the percolation of rainwater and meteoric fluids that have not been heated. The products of subaerial weathering may be further modified on the seafloor. Postcruise mineralogic and chemical analysis may help discriminate between subaerial weathering and hydrothermal pro-

cesses. As a consequence, we did not make this distinction while logging core.

On the HRVCD forms, rocks were graded according to whether they were fresh (<2% by volume alteration/weathering products) or have slight (2%–10%), moderate (10%–40%), high (40%–80%), very high (80%–95%), or complete (95%–100%) alteration/weathering. We determined the types, forms, and distributions of secondary alteration/weathering effects, as well as abundances of veins, vesicles, and their mineral fillings, using a selection of precision tools. Any changes in alteration/weathering styles throughout a section or an igneous unit were also recorded on the HRVCD. Features related to subaerial weathering are also noted on the HRVCD. Unconsolidated parts of regolith intervals are also recorded on the sedimentary VCDs.

Alteration and vein-core description logs were tabulated to provide a consistent characterization of the rocks, as well as provide the information required to make quantitative estimates of the extent of alteration. Cores were described on a piece-by-piece scale. Alteration and vein logs for each hole are presented (see the **"Core Descriptions"** contents list). Descriptions are based mostly on hand-specimen observations, and specific clay, zeolite, and carbonate minerals are not generally distinguished, except where crystal morphology allows unequivocal identification. Where additional mineralogic evidence is available from either thin-section descriptions and/or X-ray diffractograms, these identifications were integrated into the alteration and vein logs and the HRVCDs.

Table **T9** provides a list of abbreviations used in the alteration and vein logs.

T9. Abbreviations used in the alteration and vein/structure logs, **p. 83.**

We recorded the following information in the databases:

1. The alteration log (e.g., Table **T10**) was used to record the bulk-rock alteration. Each entry records the igneous unit; identifiers for the core, section, piece, subpiece; the length of each piece; and the depth below seafloor of the top of each piece. Visual estimates of the percentage of altered groundmass, color, the abundance (in percent), diameter (in millimeters), mineral fillings and halo widths (in millimeters) of vesicles, and the proportion of altered phenocrysts with the precursor and secondary minerals are documented for each piece. Data recorded for breccias include percentages of matrix and clasts, and the total percentage of secondary minerals and sediments. A column for comments is included.

T10. Example of the alteration log, **p. 84.**

2. The vein/structure log (e.g., Table **T11**) was used to record the presence, location, and mineral content of veins observed on the cut surface of the Leg 183 cores. Each entry records the igneous unit and the identifiers for the core, section, piece, and subpiece. For each vein the location of the top and bottom of the feature is recorded, and the mineral fillings, vein width (in millimeters), apparent orientation on the cut face (0°–90°; horizontal to vertical), presence or absence of a related alteration halo, and the half width (in millimeters) of the halo are described. A column for comments is included.

T11. Example of the vein/structure log, **p. 87.**

STRUCTURAL GEOLOGY

Structural features in the cores recovered during Leg 183 are summarized on the HRVCD forms. For each section we described and sketched more detailed structural information, such as the apparent and true orientations of veins and fractures and crosscutting relationships, on a separate structural geology description form (e.g., Fig. F10). Structural data are tabulated in the vein/structure logs for each site (e.g., Table T11; see "Alteration and Weathering," p. 25). We recorded observations with reference to the structural geology checklist (Table T12). The structural data entered into the vein/structure logs include

- Hole, core, section, piece number; mbsf for top of section;
- Oriented sample (yes or no);
- Structural identifier: V-vein (vein crosscutting relationships are indicated as V1 . . . Vn from earliest to latest); Va . . . Vx are veins without crosscutting relationships; F = fault with offset; S_o = bedding;
- Interval in centimeters that the feature occurs on the cut surface (top or bottom);
- Composition of material in feature; abbreviations as those defined in "Alteration and Weathering," p. 25 (see Table T9);
- Width of structure in millimeters;
- Wallrock lithology: SED (sediment), BAS (basalt);
- Orientation of planar feature: two apparent dips and the calculated strike and dip; and
- Comments regarding the continuity and geometry of the feature, as well as information regarding thickness, alteration halos, offsets, and crosscutting relationships.

F10. Example of structural geology description form, p. 71.

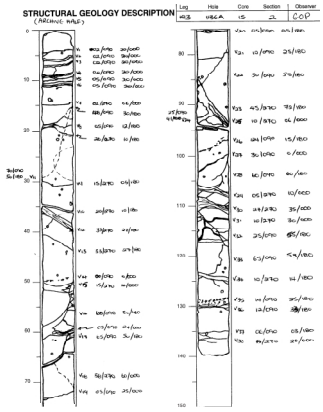

T12. Structural geology checklist, p. 91.

Geometrical Reference Frame

To orient structures within the drill core, we employed the convention adopted during Leg 135 (Shipboard Scientific Party, 1992). We assumed that the core axis is always vertical within a horizontal slice of the core. Pseudo-north, 000° is defined as 90° to the cut face of the archive core; the right side is designated as 270°, and the left side as 090° (Fig. F11). We measured most orientations as dip directions relative to the core reference frame on perpendicular sections of the core. To calculate the strike and dip for each pair of apparent dips measured for a structural feature, we used trigonometric functions in a Microsoft Excel spreadsheet that contained the vein/structure logs. If the structure was exposed in three dimensions, we measured the dip and working azimuth directly and entered them into the vein/structure log. We oriented structure relative to core piece and section depth. Depths are in centimeters from the top of the core section. When the vein extended over a depth interval, we recorded the top and bottom of its range.

F11. Orientation convention used to orient structures, p. 72.

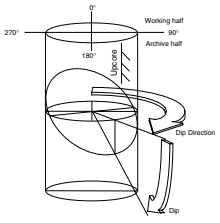

PALEOMAGNETISM

Paleomagnetic studies conducted on board the *JOIDES Resolution* during Leg 183 consisted of routine measurements of natural remanent magnetization (NRM) and of magnetic susceptibility of sedimentary and igneous rocks. NRM was measured on most archive-half cores of

sediments and basement rocks and on discrete working-half samples of sediments and basement rocks. Stepwise, alternating field (AF) demagnetization for most archive-half cores and some discrete samples was adopted for magnetic cleaning. Some igneous rocks were thermally demagnetized to obtain their primary remanent magnetization. The anisotropy of magnetic susceptibility (AMS) was determined for discrete igneous rock samples to obtain information about the magnetic fabric. Magnetic susceptibility was measured for whole cores, archive-half sections, and discrete samples. Magnetic properties were compared with the observed lithostratigraphic and basement units.

Ages of sedimentary rocks were estimated by magnetostratigraphy to establish the sedimentary history following igneous activity on the Kerguelen Plateau and Broken Ridge. The paleolatitudes of the Kerguelen Plateau and Broken Ridge at the time of their formation were determined from the remanent magnetization of igneous rocks.

Laboratory Instruments

The remanence of all archive-half sections and all oriented discrete working-half samples was measured using a 2-G Enterprises (Model 760R) pass-through cryogenic magnetometer equipped with direct-current superconducting quantum interference devices. The sensing coils of the magnetometer have slightly different response curves for each axis. The width of the sensing regions is ~10 cm, which corresponds to ~100 cm^3 of cored material. The practical limit on the resolution of natural remanence of the core samples is imposed by the magnetization of the core liner itself (~0.01 mA/m). An in-line AF demagnetizer capable of reaching peak fields of 80 mT (2-G Enterprises Model 2G600) was used with the cryogenic magnetometer. A Molspin spinner magnetometer was also available in the paleomagnetism laboratory for measurements of the NRM of discrete samples. For stepwise demagnetization of samples, the laboratory contains AF and thermal demagnetizers (Schonstedt Instrument Company Models GSD-1 and TSD-1) that are capable of demagnetizing discrete specimens to 100 mT and 700°C, respectively. Anhysteretic remanent magnetization was imparted to discrete samples by a DTECH, Inc., PARM-2 system. An Analytical Services Company Model IM-10 impulse magnetizer (capable of pulsed fields of 20 to 1200 mT) was available for studies of the acquisition of both stepwise and saturation isothermal remanence magnetization by discrete samples. For some discrete basement samples, the AMS was determined using a Kappabridge KLY/2 directional susceptibility meter and the program ANI20, provided by the manufacturer Geofyzika Brno (Czech Republic).

The magnetic susceptibility for whole-core and archive-half sections was routinely measured in 5-cm intervals using a susceptibility meter attached to the MST (see **"Physical Properties,"** p. 31), and in 4- and 2-cm intervals using a susceptibility meter attached to the AMST (see **"Spectrophotometer,"** p. 10) for sediments and basement rocks, respectively. Susceptibilities of discrete samples were also measured. For the three types of susceptibility measurements (MST, AMST, and discrete sample), the same type of magnetic susceptibility meter (Bartington Instruments Model MS2) was used with a different sensor. The sensor for whole-core measurements (MS2C) has an inner diameter of 88 mm, and the core passes through the sensor coil. The AMST has a cylindrical tip probe (MS2F), and the sensor provides a depth of investigation approximately equal to its diameter (20 mm). The measurements

were automatically recorded by the AMST, which permits measurements only at evenly spaced intervals along each section of core. Spacing of measurements varied from 2 to 10 cm. The MS1B (dual frequency) sensor was used for discrete-sample measurements. This sensor has an internal diameter of 36 mm and measures 2.54 cm of drill core at a time. General variations with depth were consistent among the three types of susceptibility measurements during Leg 183. However, the MST and AMST data occasionally had lower values than the discrete measurements, with the differences being more significant in the AMST measurements. The lower MST and AMST values were probably caused by gaps in the core and/or differences in the calibration of the sensors. The spatial resolution of the MS2C and MS2F sensors is 20 mm. For the MST measurements (MS2C), the sensor expects a volume of material 20 mm in length times the diameter of the ordinary core; thus, a gap in core material results in a lower value. For the AMST measurements (MS2F), the sensor expects a volume of material 20 mm in length times 15 mm in diameter. A gap in core material or between sensor and material thus results in a lower value. In addition, the calibration of the sensors also contributes to the differences between the three types of measurements.

During Leg 183, we could not program the AMST software to ignore measurements from voids or disturbed intervals of core (e.g., drilling slurry or biscuits). Consequently, these spurious measurements should be discarded before the data set is used. Moreover, the software (AMST v. 1.1) aborted the measurement each time the susceptibility sensor reached a core gap previously detected by the laser displacement sensor. To overcome this problem, gaps were covered during laser displacement measurements. This, however, led to systematically lower susceptibility measurements over core gaps. It is recommended that these values be discarded from the data set by comparing them with the core photographs. For rock cores, it was not always possible to measure planar, horizontal surfaces. Measurements from nonplanar, nonhorizontal surfaces produced slightly lower values (e.g., when the sensor touched the rock surface at an oblique angle). In some cores, the sensor stopped a few millimeters above the surface, also resulting in slightly lower values. Finally, a software error led to a slight shift of the starting point every few cores. This produced an offset of the actual length scale, which must be taken into account when comparing these measurements with the core sections.

Sampling

Coordinates

The standard ODP core orientation convention (fig. 8 in Shipboard Scientific Party, 1991; fig. 8 in Shipboard Scientific Party, 1997) was used for paleomagnetic measurements. This convention is defined as follows: the z-axis points downhole and is parallel to the core, and the x-axis forms a line perpendicular to the split face of the core and is directed into the working half, toward a reference mark (a double line) along the center of the core half. Discrete sample cubes and minicores were marked with an arrow in the negative-z (uphole) direction on the plane representing the split surface of the working half. The plane marked with the arrow is the y-z plane. Core orientation with a Tensor tool mounted on the APC core barrel was not achieved because only the RCB was used for drilling. Because all cores were drilled by the RCB

method, only inclination values were useful in paleomagnetic studies during Leg 183.

Sampling Method

Discrete samples were taken from soft sediment using standard plastic cubes (7 cm^3), with an arrow pointing in the uphole direction. Samples were not taken from portions of the core that were highly disturbed by drilling. To reduce deformation of the sediment while taking discrete samples, the core was cut using a thin stainless-steel spatula before pressing the cubes into the sediment. Cylindrical minicores (12 cm^3) were drilled from hard sediment and crystalline rocks using a water-cooled, nonmagnetic drill bit attached to a standard drill press. Minicores were oriented in the same manner, with an arrow pointing in the uphole direction. Typically, we took one or more discrete samples per section, and some were used for pilot demagnetization studies. In addition, discrete samples were taken from sedimentary rocks at smaller increments to examine geomagnetic reversals, key geologic boundaries, or other intervals of interest. We took several discrete samples in each flow unit of igneous rock.

Measurements

The NRM of the archive-half sections was analyzed on the cryogenic magnetometer at 5- and 2.5-cm intervals for sediments and basement rocks, respectively. To isolate characteristic magnetizations, archive halves were AF demagnetized at 20 and 40 mT for sediments and basement rocks, respectively. To confirm the reliability of the remanent magnetization, one section per each core was stepwise AF demagnetized up to 30 and 60 mT for sediment and basement rocks, respectively. For magnetic cleaning of most discrete igneous rock samples, stepwise thermal demagnetization up to 620°C was applied.

For determining the AMS, the induced magnetization of the specimens was measured at 15 positions in a 300 A/m field and the susceptibility tensor was calculated from the data. The principal magnitudes and directions of the tensor are obtained by the diagonalization of the tensor; the principal directions are given by the eigenvectors and the principal magnitudes by the eigenvalues.

Analysis

The stable or primary component of remanence was obtained from sediments after AF demagnetization. The stability of remanence within the archive cores and discrete samples was determined by both Zijderveld (1967) plots and equal-area stereographic projections. Magnetozones were defined by selecting directional data from the cryogenic magnetometer. The selection criteria were slightly different at each site. The following selection criteria were typically used during Leg 183:

1. The intensity of remanent magnetization after AF demagnetization at 20 mT was $>2 \times 10^{-4}$ A/m and hence above the noise level of the magnetometer in rough-sea conditions.
2. The inclination is >±30°.
3. At least two consecutive values (which corresponds to a split-core length of 10 cm) have the same polarity.
4. There is no significant core disturbance.

Positive and negative inclinations are defined as reversed and normal magnetic polarities, respectively. We interpreted the magnetic polarity stratigraphy, using constraints from the biostratigraphic data (see "Biostratigraphy," p. 10). The time scales of Berggren et al. (1995) and Gradstein et al. (1995) (see "Biostratigraphy," p. 10) were used for Cenozoic and Mesozoic polarity boundaries, respectively.

The characteristic inclinations of remanence from igneous rocks were obtained by component analysis (Kirschvink, 1980), and stability was examined in the same manner as for sediments. Paleolatitudes of each site at the time of eruption were calculated from mean inclination values based on the assumption of a geocentric dipole field using the equation:

$$\tan(\text{paleolatitude}) = \tfrac{1}{2}\tan(\text{inclination}). \quad (1)$$

The results from low-field susceptibility and AMS measurements were compared with lithologic units and/or geologic structures based on sedimentary, petrologic, and structural features (see "Lithostratigraphy," p. 7; "Igneous Petrology," p. 22; "Physical Volcanology," p. 16; and "Structural Geology," p. 27).

PHYSICAL PROPERTIES

Introduction and General Objectives

Shipboard physical properties determinations provide a first look at variations in core material characteristics and may be correlated with core lithology, downhole geophysical results, and regional seismic data. The principal objectives of the physical properties measurement program are closely connected to the main scientific and operational goals of Leg 183. They can be grouped together as follows:

1. Providing comprehensive physical properties datasets, including porosity and acoustic variations.
2. Integrating core physical properties data with physical parameters derived from downhole logging results. Bulk density, porosity, acoustic velocity, and thermal conductivity data can aid log interpretation.
3. Providing cross-hole correlation. Magnetic susceptibility was measured on whole-round sections along the length of the recovered core to enable correlation of stratigraphic horizons from adjacent holes.
4. Constraining the interpretation of seismic reflection and other geophysical data.

Additionally, physical properties data may help determine how the Kerguelen Plateau grew and its tectonic history, thereby contributing to the principal objectives of Leg 183.

All instruments/apparatus used in the shipboard laboratory and principles of methods are described in Blum (1997). Measurements were made on whole sections of cores using the MST. We determined thermal conductivity for sediments and basement rocks using the needle probe and half-space puck methods, respectively. When the sediment was sufficiently soft, we determined compressional-wave (*P*-wave) velocities (V_p) on the working half of the core. Using the insertion probe system

(PWS1 and PWS2) and/or the contact probe system (PWS3). For consolidated or lithified sediments and for hard rocks, we cut samples and we measured velocity using the contact probe system. Whenever possible, we measured index properties in samples where velocity was also measured.

Sampling Strategy

The sampling program for physical properties was designed to fulfill the following two requirements:

1. Whole-core sections were scanned with the MST before being split. We then selected physical properties samples from the split cores. Where recovery permitted, we chose one or two samples per section to represent the dominant lithology.
2. Core specimens for analyses were selected in conjunction with sedimentologists and structural geologists, we selected additional samples to represent intervals of unusual lithology or structure.

Whole-Core Measurements

Multisensor Track

The MST included four physical properties sensors (magnetic susceptibility meter, gamma-ray attenuation porosity evaluator [GRAPE], *P*-wave logger [PWL], and natural-gamma radiation detector [NGR]). Individual, unsplit core sections were placed on the MST, which automatically moved the section through the sensors on a fiberglass track. MST data were sampled at discrete intervals, with the sampling rate chosen to optimize data resolution and the time limitations of running each core section through the device. GRAPE data, compressional wave velocity, and magnetic susceptibility data were all logged at an interval of 4 cm and acquisition times of 5 s. Core sections were run through the MST after they had warmed to at least 16°C. GRAPE data are most reliable in undisturbed cores and offer the potential of direct correlation with downhole bulk density logs. For highly fragmented core, GRAPE acquisition was turned off. Many cores of (unconsolidated) soft sediments were disturbed to some degree. Where cores were not filling the lines, disturbed, or fractured, we expect the GRAPE density to have a general lower value.

The PWL operates simultaneously with the GRAPE and transmits a 500-kHz *P*-wave pulse (2-µs wave period; 120 V) through the core. A pair of displacement transducers monitors the separation between the *P*-wave transducers. Data are collected at 3-cm intervals. The quality of the data was assessed by examining the arrival time and amplitude of the received pulse. Data with anomalously large travel times or low amplitudes were discarded. Because RCB cores do not fill liners, only selected cores from each site were run through the PWL.

Magnetic susceptibility was determined on all sections at 3- to 5-cm intervals using the 1.0 (1 s integration time) range on the Bartington meter (model MS2C), which has an 88-mm coil diameter. Magnetic susceptibility helps detect variations in magnetic properties caused by lithologic changes or alteration. The quality of these results is degraded in RCB sections if the core liner is not completely filled or the core is disturbed. However, general downhole trends may still be used for labo-

ratory to well-log correlation. During Leg 183, magnetic susceptibility was also determined with a point-susceptibility meter on the AMST. We routinely compared data from the two instruments (see "Paleomagnetism" sections in the site chapters for discussion).

NGR emission was routinely recorded for all core sections, both to monitor variations in radioactive counts of sample rocks and to provide a correlation with the geophysical logging. The NGR system records radioactive decay of ^{40}K, ^{232}Th, and ^{238}U, three long half-life isotopes. The total gamma-ray count is a function of the combined influence of these three isotopes. The installation and operating principles of the NGR system used during Leg 183 are discussed by Blum (1997).

The area of influence for the four NGR sensors was ~10 cm from the points of measurements along the core axis. As gamma-ray emission is random, count times have to be sufficiently large to average for short-period variations. This was achieved on the MST system by utilizing the long area of influence on the sensors and using a moving average window to smooth count-rate variations and to achieve a statistically valid sample.

The NGR system was calibrated in port against a thorium source. We generally made measurements every 16 cm and, in some basement rock, every 6 cm. Results were output in CPS (counts per second) units.

Thermal Conductivity

Thermal conductivity is the rate at which heat is transmitted by molecular conduction. Thermal conductivity is an intrinsic material property that depends on the chemical composition, porosity, density, structure, and fabric of the material. Thermal conductivity profiles of sediments and rock sections are mainly used, along with temperature measurements, to calculate heat flow. Heat flow is not only characteristic of the material but also helps to indicate age of ocean crust and fluid circulation processes at a range of depths (Blum, 1997). Whole-round core sections were allowed to equilibrate to room temperature for at least 2 hr in preparation for thermal conductivity measurements. We used the needle-probe method in full-space configuration for soft sediments and in half-space mode for lithified sediment and hard-rock samples. We typically acquired data in every soft-sediment core and every section in basement rocks. Data are reported in units of W/(m·K). The mean error associated with these determinations is estimated as ±0.2 W/(m·K) in sediments. For technical details see Blum (1997).

Soft-Sediment Full-Space Determinations

We inserted a needle probe containing a heater wire and a calibrated thermistor into the sediment through a small hole drilled in the core liner before the sections were split. At the beginning of each determination, we monitored temperatures in the samples without applying current to the heating element to verify that temperature drift was <0.04°C/min. We then turned on the heater and recorded the temperature rise in the probes. After heating for ~60 s, the needle probe behaves nearly as a line source with constant heat generation per unit length. We fit the temperatures recorded between 60 and 240 s to the following equation using the least-squares method (von Herzen and Maxwell, 1959):

$$T(t) = (q/4\pi k) \cdot \ln(t) + L(t), \quad (2)$$

where k is the apparent thermal conductivity (W/[m·K]), T is temperature (°C), t is time in s, and q is the heat input per unit length of wire (W/m). The term $L(t)$ corrects for temperature drift, described by the following equation:

$$L(t) = At + T_e, \quad (3)$$

where A represents the rate of temperature change, and T_e is the equilibrium temperature. $L(t)$ therefore corrects for the background temperature drift, systematic instrumental errors, probe response, and sample geometry. The best fit to the data determines the unknown terms k and A.

Lithified Sediment and Hard-Rock Half-Space Determinations

We made half-space determinations on selected lithified sediments and basaltic rock samples after the cores were split and their faces polished. The needle probe rested between the polished surface and a grooved epoxy block with relatively low conductivity (Sass et al., 1984; Vacquier, 1985). We conducted half-space measurements in a water bath to keep the samples saturated, to improve the thermal contact between the needle and the sample, and to reduce thermal drift. EG&G thermal joint compound was used to improve the thermal contact. Data collection and reduction procedures for half-space tests are similar to those for full-space tests except for a multiplicative constant in equation 3 that accounts for the different experimental geometry.

Discrete Measurements in Split-Core Samples

Index Properties

We extracted samples of ~10 cm³ from the fresh core for determination of index properties. We calculated bulk density, grain density, water content, porosity, and dry density from wet and dry sample and dry volumes. The error associated with mass determinations using two Scitech electronic balances is ±0.05%. The balance was equipped with a computer averaging system that corrected for ship accelerations. The sample mass was counterbalanced by a known mass such that the mass differentials generally were <1 g. We determined sample volumes using a Quantachrome Penta-Pycnometer, a helium-displacement pycnometer with a nominal precision of ±0.02 cm³, but with apparently a lower experimental precision of ±0.04 cm³. We determined sample volumes at least three times, until readings were consistent. A standard reference volume was included with each group of samples during the measurements and rotated among the cells to check for instrument drift and systematic error. This exercise demonstrated that the measured volumes had a precision of ~0.02 cm³. We carefully calculated the sample beakers used for discrete determinations of index properties before the cruise. After the samples were oven dried at 105 ± 5°C for 24 hr and allowed to cool in a desiccator, we measured dry weight and volumes. The main problem with this drying temperature is that chemically bound water in clay minerals is largely lost in addition to interstitial water.

Water Content

The determination of water content as a fraction of total mass or as a ratio of water mass to solid mass followed the methods of the American Society for Testing and Materials (ASTM) designation (D) 2216 (ASTM, 1989). We measured total mass (M_t) and dry mass (M_d) using the electronic balance and the difference was taken as the uncorrected water mass. Corrections for salt assumed a pore-water salinity (r) of 0.35%, following the discussion by Boyce (1976). The equations for the two water content (W) calculations are

$$W_d \text{ (percent dry mass)} = [(M_t - M_d)/(M_d - rM_t)] \cdot 100, \quad (4)$$

$$W_w \text{ (percent wet mass)} = \{(M_t - M_d)/[(1 - r)\, M_t]\} \cdot 100, \quad (5)$$

where M_t and M_d are measured in grams.

Bulk Density

Bulk density (ρ_{bulk}) is the density of the total sample including the pore fluid (i.e., $\rho_{bulk} = M_t/V_t$), where V_t is the total sample volume (in cubic centimeters).

Grain Density

Grain density (ρ_g) was determined from the dry mass and dry volume measurements. Both mass and volume must be corrected for salt, leading to the following equation:

$$\rho_g = (M_d - M_s)/[V_d - (M_s/\rho_s)], \quad (6)$$

where M_d is the dry mass (g) and ρ_s is the density of salt (2.257 g/cm^3).

$M_s = r\, M_w$ (g) is the mass of salt in the pore fluid, M_w (g) is the salt-corrected mass of the seawater:

$$M_w = (M_t - M_d)/(1 - r). \quad (7)$$

Porosity

Porosity (ø) represents the ratio of pore-water volume to total volume. The following relationship was employed:

$$ø = [(\rho_g - \rho_{bulk})/(\rho_g - \rho_w)] \cdot 100, \quad (8)$$

where ρ_g represents the calculated grain density, ρ_{bulk} is the bulk density, and ρ_w is the density of seawater.

Dry Density

The dry density (ρ_d) is the ratio of the dry mass (M_d) to the total volume (V_t). We calculated the dry density using the corrected water content (W_d) and porosity (ø) as follows:

$$\rho_d = (ø/W_d) \cdot \rho_w. \quad (9)$$

Velocity Determinations

For discrete velocity measurements in split cores, we used the insertion probe system (PWS1 and PWS2) and the contact probe system (PWS3), using a signal frequency of 500 kHz. In soft sediments, we employed the insertion probe system that determines the traveltime over a fixed interval in the y (across the core) and z (along the core) directions. For consolidated and lithified sediments and for hard rocks, only the PWS3 was used, measuring samples within the liner or in cut samples. When lowering the transducer to the core surface, an indeterminate pressure is applied. For all measurements, we lowered the transducer to the point where it just reached the surface. We then applied an additional force of 20 psi, sufficient for achieving good contact yet nondestructive on soft sediments. Measurements of ultrasonic velocities are known to be relatively more stress sensitive in the low-pressure regime. The system was calibrated with Plexiglas standards, corresponding to velocities being found in sediments. The system was not calibrated with standards representing high velocities, and this may account for velocities >6000 m/s in some hard rocks. If the high velocities are a consequence of the calibration method, it would result in an increasing error as the velocities increase, but the general trend would be valid. At Site 1137, the discrete velocity measurements agree well with sonic log data, and all velocities are <6000 m/s. At later sites, and where we encounter higher velocities, we did not have sonic log data for comparison. Determining velocity over a short distance, as in some cut samples, can also increase the uncertainty of the measurements. We measured compressional wave velocity (500 kHz) once or twice per section and in more than one direction of the core where possible. Distilled water constituted the coupling fluid at the transducer/core interface. Sediments were measured in half liners or in discrete samples taken from the core. For disturbed or biscuited sediments, we employed a needle-probing method to identify harder and preserved biscuits for measurement. We sampled crystalline and basaltic rocks as minicores (2.54 cm in diameter) drilled perpendicular to the axis of the core (x-direction) or sawed as oriented cubes. The ends of the minicores were trimmed parallel with a rock saw, and we measured traveltimes and distances along the axis of the minicore. Velocities for cubes were determined in two or three mutually perpendicular directions, V_z (along the core), V_x (into the split core, perpendicular to core axis), and V_y (across the split core). Velocity anisotropy follows the relationship

$$\text{Anisotropy} = 3(V_{max} - V_{min})/(V_x + V_y + V_z), \quad (10)$$

where V_{max} and V_{min} are the maximum and minimum velocities (among V_x, V_y, and V_z). During Leg 183, we made measurements for velocity determinations either adjacent to paleomagnetic minicores or directly on the minicores to save core material for shipboard physical properties samples. In intervals where discrete sampling was sparse, and if time allowed, we made additional measurements on split pieces of hard rocks. Velocities from these measurements may have slightly lower values because of a more irregular contact surface. Nevertheless, velocities determined from hard-rock pieces should exhibit trends similar to those from discrete sample measurements.

We determined the dimensions of samples analyzed in the contact probe system with digital calipers. During Leg 183, we noted that the display of the digital caliper needed to be monitored regularly or erro-

neous readings could occur. It is imperative to keep the caliper's track clean. We estimated traveltime by identifying the first break of the stacked waveforms, and we corrected traveltime for system delays. Using the corrected traveltime and path length, we calculated velocities. Velocity data are reported here in raw form.

ORGANIC AND INORGANIC GEOCHEMISTRY

Shipboard organic geochemistry during Leg 183 included the following analyses: analyses of the light hydrocarbon gases in the sediment, determination of carbonate carbon concentrations, and elemental analyses of carbon, hydrogen, nitrogen and sulphur.

Hydrocarbon Gases

The primary focus of shipboard organic geochemical analyses is to provide, on the basis of observations and expertise, advice concerning the probable risks of an uncontrolled release of petroleum hydrocarbons (i.e., gas and/or oil). Imminent risks to the ship and/or the environment must be assessed, and the ODP operations manager and co-chief scientists must be advised in time so that drilling can be terminated and the hole plugged and abandoned before penetration of a hazardous depth interval.

As hydrocarbon generation is a natural and inevitable result of the maturation of buried organic matter, the objective from the safety standpoint is to distinguish possible hazardous accumulations of hydrocarbons against the background of the normal increase in hydrocarbon content with depth. The degree of organic matter maturation and its ability to generate hydrocarbons may be estimated from the content of C_{2+} hydrocarbons (C_2, ethane; $C_{2=}$, ethylene; C_3, propane; $C_{3=}$, propylene) relative to methane (C_1). The C_1/C_{2+} ratio changes from >1000 for immature to <100 for mature organic matter. Plots of log C_1/C_2 ratios vs. depth give downhole trends. Deviations from these trends toward a significantly higher contribution of heavier hydrocarbons justifies caution. As a general guideline, values <200 for C_1/C_2 and 2000 for C_1/C_3 justify caution.

During Leg 183, concentrations of the light hydrocarbon gases, C_1 through C_3, were monitored in each sediment core. Gases were extracted using the headspace technique for bulk sediments. Immediately after the core was retrieved and cut into 150-cm sections, a No. 6 cork borer was used to obtain a measurable volume of sediment from the top of one of the sections, usually midcore. This ~5-cm³ sediment sample was placed in a glass vial, sealed, and heated in an oven at 60ºC for 30 min before gas analysis. A gas-tight syringe and needle was then used to extract ~5.0 mL of headspace gas.

Headspace gas was analyzed using a Hewlett Packard 5890 Series II gas chromatograph (GC) equipped with a 2.44 m × 3.18 mm stainless steel column, packed with HaySep S (100/120) mesh, and a flame ionization detector. The headspace syringe was directly connected to the GC via a 1.0-cm³ sample loop. A Hewlett Packard GC ChemStation (Rev A.05.04) was used for data collection and evaluation. Calibration was performed using Scotty II and IV analyzed gases.

Inorganic Carbon

Carbonate carbon concentrations were determined using a Coulometrics CO_2 coulometer. Sediments were generally analyzed at a frequency of one sample per core.

The coulometric cell is filled with a partially aqueous proprietary solution containing monoethanolamine (ME) and a colorimetric indicator. A platinum cathode (negative electrode) and a silver anode (positive electrode) are placed in the cell, and the cell assembly is positioned between a light source and a photodetector (measuring the intensity of radiant energy) in the coulometer.

The samples (~10 mg of freeze-dried, ground sediment) are acidified with 2N HCl in a heated vial to generate forms of inorganic carbon as carbon dioxide. Carbon dioxide free air carries the CO_2 through a scrubbing system into the coulometer for detection. In the coulometer cell, the CO_2 is quantitatively absorbed, reacting with ME to form a titratable acid that causes the color to fade. The photodetector monitors the change in the solution's color as percent transmittance. As the percent transmittance increases, the titration current is automatically activated to generate a base at a rate proportional to the percent transmittance. When the solution returns to its original color, the current stops.

The weight percentage of carbonate is calculated from the inorganic carbon (IC) content, with the assumption that all inorganic carbon is present as calcium carbonate ($CaCO_3$):

$$CaCO_3 = IC \cdot 8.332. \quad (11)$$

Calibration was performed using pure calcium carbonate as a standard.

Elemental Analysis

Total carbon, hydrogen, nitrogen, and sulfur were determined using a Carlo Erba 1500 NCS Analyzer. Sediments were generally analyzed at a frequency of one sample per one or two cores and samples of basaltic basement that were analyzed by XRF were also analyzed by NCS (see "Igneous Petrology," p. 22).

Approximately 5 mg of freeze-dried, ground sediment and vanadium pentoxide (V_2O_5) was combusted at 1000°C in a stream of oxygen. Using helium as a carrier gas, the oxygen was removed and the combustion products were reduced. The reduced gases were separated by gas chromatography (a 2-m packed column) and quantified with a thermal conductivity detector. The EAGER 200 software program was used for data collection and analyses.

Sulfanilamide (16.27% N, 41.84% C, 18.62% S, and 4.86% H) was used as the primary standard and the National Institute of Standards and Technology's Estuarine Sediment (0.18% N, 1.79% C, and 0.96% S), which is more representative of marine particulate matter, as the secondary standard. Reagents for the elemental analyzer included the oxidation catalyst (tungstic anhydride granules), a desiccant (magnesium perchlorate), and reduced copper wire.

The organic carbon (OC) was then calculated from the total carbon (TC) found from the NCS Analyzer and the inorganic carbon (IC) found from the coulometer:

$$OC = TC - IC. \quad (12)$$

DOWNHOLE MEASUREMENTS

Logging Procedures and Logging Data

Introduction

Downhole logs reveal the physical, chemical, and structural properties of formations penetrated during drilling. A variety of geophysical tools make rapid, closely spaced in situ measurements as a function of depth after the hole has been drilled. Logs can be used to interpret the stratigraphy, lithology, and mineralogy of the penetrated formation. Where core recovery is incomplete or disturbed, log data may be the only way to characterize the borehole section. Where core recovery is good, log and core data complement one another. Geophysical well logs can aid in characterizing lithologic sedimentary sequences and stratal stacking patterns when integrated with core and seismic reflection data.

Individual logging tools were joined together into tool strings (Fig. F12) so that several measurements could be made during each logging run (Table T13). The tool strings were lowered to the bottom of the borehole on a wireline cable, and data were logged as the tool string was pulled back up the hole. Repeat runs were made in some holes to improve coverage and confirm the accuracy of log data. Not all tool strings were run in each hole; refer to individual site chapters for details of logging strings deployed at each site. During logging runs a wireline heave compensator was employed to minimize the effect of the ship's heave, caused by sea swell, on the motion and position of the tool string in the borehole.

F12. Schematic illustration of the configurations of tool strings run, p. 73.

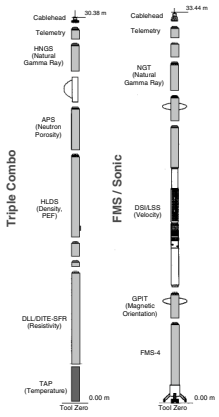

T13. Specifications of the logging tools deployed, p. 92.

Logging Tools and Tool Strings

During Leg 183, we deployed three different logging strings (Fig. F12; Table T13):

(1) The triple combo (resistivity, density, and porosity) tool string consists of the dual laterolog (DLL), the high temperature lithodensity sonde (HLDS), and the accelerator porosity sonde (APS). The hostile environment natural gamma-ray sonde (HNGS) was included at the top, and the LDEO high resolution temperature/acceleration/pressure tool (TAP) was attached to the base of this tool string. Because of the low resistivities we encountered in the first hole logged (Site 1137), we substituted the dual induction tool (DITE) for the DLL at all subsequent sites. (2) The FMS-Sonic tool string consists of the Formation MicroScanner (FMS), the general purpose inclinometer tool (GPIT), and the dipole shear sonic imager (DSI). The natural gamma-ray tool (NGT) was included at the top of this tool string. The DSI was replaced by the long-spaced sonic tool (LSS) because of tool failure. (3) The well seismic tool (WST). Data from the NGT or HNGS placed at the top of all but the WST tool string provide a common basis for correlation of several logging runs and for depth shifting all logs.

Principles and Uses of the Logging Tools

We describe individual logging tools used during Leg 183, including their geological applications and the controls on data quality, below. The properties of the formation logged by each tool, the sample intervals, and the precision of the measurements (including the vertical res-

olution) are summarized in Table T13. Explanations of tool name acronyms, the acronyms by which the log data generated by the different tools, are referred, and their units of measurement are summarized in Table T14.

More detailed descriptions of individual logging tools and their geological applications can be found in Ellis (1987), Goldberg (1997), Lovell et al. (1998), Rider (1996), Schlumberger (1989, 1994, 1995), Serra (1984, 1986, 1989), and the LDEO-BRG Wireline Logging Services Guide (1994).

T14. Logging tool and measurement acronyms and units of measurement, p. 93.

Hostile Environment Spectral Gamma-Ray Sonde and Natural Gamma-Ray Tool

The HNGS and the NGT measure the natural gamma radiation from isotopes of potassium, thorium, and uranium in the rocks surrounding the tool. The NGT uses a sodium iodide scintillation detector to measure the natural gamma-ray emission and five-window spectroscopy to determine concentrations of radioactive K (in weight percent), Th (in parts per million), and U (in parts per million). The NGT and HNGS use a similar measurement principle. However, the HNGS uses two bismuth germanate scintillation detectors for gamma-ray detection with full spectral processing, significantly improving tool precision compared to the NGT. The spectral analysis filters out gamma-ray energies <500 keV, eliminating sensitivity to bentonite or KCl in the drilling mud, and improves measurement accuracy. The HNGS generates the same output as the NGT, and it estimates the average borehole potassium contribution to the total potassium signal. Shipboard corrections to the HNGS account for variability in borehole size and borehole potassium concentrations. The NGT and HNGS also measure the total gamma-ray signature (SGR, gAPI [American Petroleum Institute] units) and uranium-free or computed gamma ray (CGR, gAPI units).

The NGT response is influenced by borehole diameter and the weight and concentration of bentonite or KCl present in the drilling mud. KCl may be added to the drilling mud to prevent freshwater clays from swelling and forming obstructions. All of these effects are corrected during processing of NGT data at the LDEO Borehole Research Group (LDEO-BRG).

High Temperature Lithodensity Sonde

The HLDS consists of a radioactive cesium (^{137}Cs) gamma-ray source (662 keV) and far and near gamma-ray detectors mounted on a shielded skid, which is pressed against the borehole wall by a hydraulic eccentralizing arm. Gamma rays emitted by the source experience both Compton scattering and photoelectric absorption. Compton scattering involves the transfer of energy from gamma rays to electrons in the formation via elastic collision. The number of scattered gamma rays that reach the detectors is directly related to the number of electrons in the formation, which is in turn related to bulk density (RHOM). Porosity may also be derived from this bulk density if the grain- and pore-fluid densities are known.

The HLDS also measures the photoelectric effect factor (PEF) caused by the absorption of low-energy gamma rays. Photoelectric absorption occurs when gamma rays reach <150 keV after being repeatedly scattered by electrons in the formation. Because PEF depends on the atomic

number of elements in formation, it is independent of porosity. Thus, PEF varies according to the chemical composition of the sediment. For example, the PEF of pure calcite = 5.08 barn/e^-; illite = 3.03 barn/e^-; quartz = 1.81 barn/e^-; and kaolinite = 1.49 barn/e^-. The PEF values can be used in combination with NGT curves to identify different types of clay minerals. Coupling between the tool and borehole wall is essential for good HLDS logs. Poor contact results in underestimation of density values. Both density correction and caliper measurement of the hole are used to check the contact quality.

Accelerator Porosity Sonde

The APS consists of a minitron neutron generator, which produces fast neutrons (14.4 MeV), and five neutron detectors (four epithermal and one thermal), positioned at different distances along the tool. The tool is pressed against the borehole wall by an eccentralizing bow spring. Emitted high-energy (fast) neutrons are slowed by collisions. The amount of energy lost per collision depends on the relative mass of the nucleus with which the neutron collides. Much energy is lost when the neutron strikes a nucleus of equal mass such as hydrogen, which is mainly present in the pore water. On degrading to thermal energies (0.025 eV), the neutrons are captured by the nuclei of Si, Cl, B, and other elements, resulting in a gamma-ray emission. The neutron detectors record both the numbers of neutrons arriving at various distances from the source and neutron arrival times, which are a proxy for formation porosity. However, hydrogen bound in minerals such as clays or in hydrocarbons also contributes to the measurement, so the raw porosity value is often an overestimate. The near/array limestone porosity corrected (APLC) log is usually displayed. The pulsing of the neutron source provides the measurement of the thermal neutron cross section (σ) in capture units (cu). It is a useful indicator for the presence of elements of high-thermal neutron capture cross section such as B, Cl, and rare-earth elements.

Dual Laterolog

The dual laterolog provides two resistivity measurements with different depths of investigation: deep (LLD) and shallow (LLS). In both devices, a current beam is forced horizontally into the formation by using focusing (also called bucking) currents. For deep measuring, both measure and focusing currents return to a remote electrode on the surface; thus, the depth of investigation is greatly improved, and the effect of borehole, and of adjacent formations, conductivity is reduced. In the shallow laterolog, the return electrodes that measure the bucking currents are located on the sonde, and, therefore, the current sheet retains focus over a shorter distance than the deep laterolog. The depth of investigation depends on the resistivity of the rock and on the resistivity contrast between the zone invaded by drilling fluid and the virgin (uninvaded) zone. Because of the inverse relationship between resistivity and porosity, the dual laterolog can be used to estimate the porosity of the rock from Archie's equation (Archie, 1942) if the sediments or rocks do not contain any clay. Archie's equation is expressed as $FF = a \cdot \phi^{-m}$, where ϕ is the porosity, a is a constant usually with set values of $a = 1$, and m is known as the cementation factor and it depends on the shape of the particles, which indicates the geometry of the pore channels.

Fracture porosity can be estimated from the separation between the deep and shallow measurements based on the observation that the former is sensitive to the presence of horizontal conductive fractures only, while the latter responds to both horizontal and vertical conductive structures. Compared to resistivity induction logging the DLL produces reliable data in highly resistive formations (>1000 Ωm).

Dual Induction Tool/Spherically Focused Resistivity Tool (DITE-SFR)

The DITE-SFR provides three different measurements of electrical resistivities, each with a different depth of investigation in the formation. Two induction devices (deep and medium resistivity) transmit high-frequency alternating currents through transmitter coils, creating magnetic fields that induce secondary (Foucault) currents in the formation. These ground-loop currents produce new inductive signals, proportional to the conductivity of the formation, which are measured by the receiving coils. The measured conductivities are then converted to resistivity. A third device, a spherically focused resistivity instrument that gives higher vertical resolution, measures the current necessary to maintain a constant voltage drop across a fixed interval.

LDEO High Resolution Temperature/Acceleration/Pressure Tool

The TAP is a new "dual application" logging tool (i.e., it can operate as either a wireline tool or as a memory tool using the same sensors and data acquisition electronics depending on the purpose and required precision of logging data) (Table T15). During Leg 183, the LDEO-TAP was deployed as a memory tool in low-resolution mode; the data were downloaded via modem after the logging run was completed. The LDEO-TAP offers greater flexibility in logging operations, and it substantially improves the quality and resolution of data over an extended ambient temperature range (when used in the wireline mode) compared to its predecessor, the LDEO temperature logging tool.

T15. LDEO-TAP tool specifications, p. 94.

The tool starts recording automatically after reaching a preset pressure (depth). Temperature, measured by high precision thermistors, and pressure are measured every second. Tool acceleration is recorded four times per second. Data, recorded as a function of time, are correlated to depth based on a synchronized time-wireline cable depth record and pressure recordings. Temperatures determined using the LDEO-TAP do not necessarily represent in situ formation temperatures because water circulation during drilling will have disturbed temperature conditions in the borehole. However, from the spatial temperature gradient it is possible to identify abrupt temperature changes that may represent localized fluid flows into the borehole, indicating fluid pathways and fracturing and/or breaks in the temperature gradient that may correspond to contrasts in permeability at lithologic boundaries.

Dipole Shear Sonic Imager

The DSI employs a combination of monopole and dipole transducers to make accurate measurements of sonic wave propagation in a wide variety of lithologies (Schlumberger, 1995). In addition to a robust and high-quality determination of compressional wave velocity the DSI can

determine shear-wave velocity (V_s) in most formations. The configuration of the DSI also allows recording of cross-line dipole waveforms. These modes can be used to estimate shear-wave splitting caused by preferred mineral and/or structural orientations in consolidated formations. A low-frequency source enables Stoneley waveforms to be acquired as well.

We deployed the DSI in two passes of the FMS-Sonic tool string combination, where the DSI replaced the more commonly used array sonic tool. The DSI was run in conventional P and S modes, along with the dipole recording modes.

The DSI tool consists of a transmitter sonde, a receiver sonde, and an acquisition cartridge (see Fig. F13). The transmitter sonde consists of a power amplifier and switching circuitry, which drive one dual-frequency (14 and 1 kHz) monopole transmitter and two pair of dipole (2.2 kHz) transmitters. Separate source functions with appropriate shape and frequency content are used for compressional, Stoneley, and dipole wave modes, respectively.

The receiver sonde houses eight receiver groups spaced every 15 cm, each consisting of four orthogonal elements aligned with the dipole transmitters. During acquisition, the output from these 32 individual elements are differenced or summed appropriately to produce in-line and cross-line dipole signals or monopole-equivalent (compressional and Stoneley) waveforms.

Preliminary processing of DSI data by the Schlumberger Multitask Acquisition and Imaging System (MAXIS 500) estimates monopole and dipole mode velocities using waveform correlation of the digital signals recorded at each receiver. In most instances, the shear-wave data should be reprocessed postcruise to correct for the effects of dispersion, which is caused by the variation of sound velocity with frequency. Processing techniques must be applied to account for a dispersive model without assumptions or to compute a bias correction to minimize any frequency effects on the velocity.

In addition, information such as mode amplitudes, shear-wave polarization, and Poisson's ratio can be extracted postcruise to provide information about lithology, porosity, and anisotropy. Amplitude processing and stacking of Stoneley-wave reflections may also be used to identify fractures, fracture permeability, and aperture in the vicinity of the borehole. The DSI tool is particularly important for determining shear-wave velocities for the upper parts of the basalt flow units. The V_p/V_s ratio in basalts is typically 1.8–2.0. Thus, the part of the lava flow with V_p of <3.0 km/s will have a V_s of <1.5 km/s, which cannot be determined without using the dipole source of the DSI tool.

F13. Diagram showing the DSI tool configuration, p. 74.

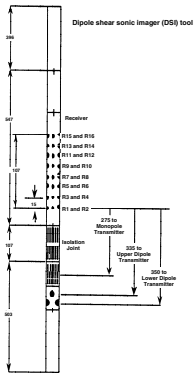

Long-Spaced Sonic Tool

The LSS measures the compressional wave velocity of the formation. The LSS is configured with two acoustic sources 61 cm apart and two receivers also spaced 61 cm apart. The spacing between the upper receiver pair and the transmitter pair is 2.44 m. The tool measures traveltime in microseconds over a certain distance in the formation. The configuration of the tool allows eight different traveltime measurements that compensate for irregular borehole walls. The velocity data together with the formation density can be used to generate a synthetic seismogram.

Formation MicroScanner

The FMS produces high-resolution images of borehole wall microresistivity that can be used for detailed sedimentologic or structural interpretation. This tool has four orthogonally oriented pads, each with 16 button electrodes that are pressed against the borehole walls. Good contact with the borehole wall is necessary for acquiring good quality data. Of a 25-cm borehole, ~30% is imaged during a single pass. Coverage may be increased by a second run. The vertical resolution of FMS images is ~5 mm, allowing features such as burrows, thin beds, fractures, veins, and vesicles to be imaged. The resistivity measurements are converted to color or grayscale images for display. A histogram of image data is used to subdivide the cumulative distribution in classes. During Leg 183, local contrasts in an image of all FMS figures in the site chapters were improved by applying dynamic normalization to the FMS data. A linear transform is applied to the input data to keep a constant mean and standard deviation within a sliding window (1 m was used). When dynamic normalization is used, the values of color indicate relative changes in resistivity. Furthermore, the hole diameter was reduced artificially from 25.1 to 15.2 cm to see more details in the pad tracks. This in effect reduced the blank space between the pad tracks and thereby enlarged the images produced by the FMS data proportionally.

FMS images are oriented to magnetic north using the GPIT (see below). This allows the dip and strike of geological features intersecting the hole to be measured from processed FMS images. FMS images can be used to visually compare logs with the core to ascertain the orientations of bedding, fracture patterns, sedimentary structures, and to identify stacking patterns. FMS images have proved particularly valuable in interpreting sedimentary structures, and they have been used to identify cyclical stacking patterns in carbonates (Eberli, Swart, Malone, et al., 1997), turbidite deposits (Lovell et al., 1998), cross-beds (Hiscott et al., 1992), facies changes (Serra, 1989), and volcanic sequences (Demant et al., 1995). Detailed interpretation of FMS images in combination with other log and core data in the sense of core-log integration will be carried out postcruise.

General Purpose Inclinometer Tool

The GPIT is included in the FMS-Sonic tool string to calculate tool acceleration and orientation during logging. The GPIT contains a triple-axis accelerometer and a triple-axis magnetometer. The GPIT records the orientation of the FMS images, and it allows more precise determination of log depths than can be determined from cable length, which may experience stretching and/or be affected by ship heave.

Well Seismic Tool

The WST is used to produce a zero-offset vertical seismic profile and/or check shots in the borehole. The WST consists of a single geophone used to record the full waveform of acoustic waves generated by a seismic source positioned just below the sea surface. During Leg 183, a 300-in^3 air gun positioned at a water depth of 3–7 m, depending on wave height, and offset from the borehole by 50 m on the port side of the *JOIDES Resolution,* was used as the seismic source. The WST was clamped against the borehole wall at 30- to 50-m intervals, and the air gun was typically fired between five and 15 times at each station. The

recorded waveforms were stacked and a one-way traveltime was determined from the median of the first breaks for each station, thus providing check shots for calibration of the integrated transit time calculated from sonic logs. Check-shot calibration is required for the borehole to seismic tie because compressional wave velocity derived from the sonic log may differ significantly from seismic stacking velocities and velocities obtained via well-seismic surveys. This is caused by (1) differential frequency dispersion (the sonic tool operates at 10–20 kHz; seismic data is in the 50- to 100-Hz range), (2) difference in travel paths between well-seismic and surface-seismic surveys, and (3) borehole effects caused by formation alterations (Schlumberger, 1989). In addition, sonic logs cannot be measured through pipe, and the traveltime to the uppermost logging point has to be estimated by other means.

Data Quality

Log data quality is largely determined by the state of the borehole wall. It may be seriously degraded by rapid changes in the hole diameter and in sections where the borehole diameter greatly decreases or is washed out. Deep-investigation measurements, such as the resistivity and sonic compressional wave velocity, are least sensitive to borehole conditions. Nuclear measurements (density and neutron porosity) are more sensitive because of their shallower depth of investigation and the effect of increased drill-fluid volume on neutron and gamma-ray attenuation. Corrections can be applied to the original data to reduce these effects. We cannot, however, correct for very large washout. By use of the HNGS and the NGT on the strings, data can be depth correlated between logging runs. Logs from different tool strings may still, however, have depth mismatches caused by either cable stretch or ship heave during recording. Ship heave is minimized by a hydraulic wireline heave compensator designed to adjust for rig motion during logging operations.

Data Recording and Processing

Data for each logging run were recorded and stored digitally and monitored in real time using the Schlumberger MAXIS 500 system. After logging a hole, data were transferred to the shipboard Downhole Measurements Laboratory for preliminary processing and interpretation. FMS image data were interpreted using Schlumberger's Geoframe 3.1.4 software package. Well-seismic, sonic, and density data were interpreted using GeoQuest's IESX software package to establish the seismic-to-borehole tie. We plotted logs from the shipboard-processed data as depth-related curves, or images, representing the physical and chemical properties of the strata penetrated.

Log data were also transmitted to LDEO-BRG for processing using a FFASTEST satellite high-speed data link, soon after each hole was logged. Data processing at LDEO-BRG includes (1) depth-shifting all logs relative to a common datum (i.e., mbsf), (2) corrections specific to individual tools, and (3) quality control and rejection of unrealistic or spurious values. Once processed at LDEO-BRG, log data were transmitted back to the ship providing near real-time data processing. Log curves of LDEO-BRG processed data were then replotted on board for refining interpretations (see "Downhole Measurements" in each site chapter). Further postcruise processing of the log data from the FMS is performed at the Laboratoire de Mésures en Forage (LMF) in Aix-en-

Provence, France. Mismatches of data sets can be related to ship heave, which caused irregular tool motion.

Postcruise-processed data (acoustic, caliper, density, gamma-ray, magnetic, neutron porosity, resistivity, and temperature) are available in ASCII format (see the **"Related Leg Data"** contents list). Access to the log data is free. A summary of "logging highlights" is also posted on the LDEO-BRG website at the end of each leg.

Downhole logging on board the *JOIDES Resolution* is provided by LDEO-BRG in conjunction with Leicester University Borehole Research, the LMF, University of Aachen, University of Tokyo, and Schlumberger Well Logging Services.

UNDERWAY GEOPHYSICS

Underway geophysical data were collected during all transits. Onboard instrumentation used included a precision echo-sounder (3.5 kHz), magnetometer, gyrocompass (Lehmkul LR40), and GPS navigation systems.

Navigation

The GPS was used throughout Leg 183. Three GPS systems were available for operation, with output provided to the underway geophysics laboratory. A GPS from Ashtech GG24 was used as the primary navigation device throughout the leg. Older Omnistar and Magnavox GPS systems were available, but not used.

GPS fixes were available continuously (1-s updates) and were recorded at ~60-s intervals. Event data were recorded at 60-s intervals on site and in transit. Navigation data were logged by the WINFROG software system, mounted on a dedicated PC in the underway geophysics laboratory. Subsequent processing and display of navigation data were performed using the Generic Mapping Tools (GMT) software package (Wessel and Smith, 1995) on shipboard Unix workstations.

Echo-Sounder

One 3.5-kHz echo-sounder (precision depth recorder) was used to acquire bathymetric data as well as high-resolution reflection records of the uppermost sediment layers. Data from the system were recorded on an EPC 8082 analog line-scanning recorder. The 3.5-kHz system used a Raytheon CESP III Correlator Echo-Sounder Processor driven by a Raytheon PTR105B transceiver with a 2-kW sonar transmitter and included a single EDO-type 323c transducer. The transducers are mounted in a sonar dome on the hull 40 m forward of the center of the moonpool. This location was chosen to reduce ship-generated noise and signal attenuation from aeration beneath the hull. The recorder was annotated automatically at fixed intervals; ship speed and heading were marked every 5 min, and position, every 30 min. Depth readings were taken manually every 5 min and entered into an Excel spreadsheet.

Magnetometer

Total intensity measurements of the Earth's magnetic field were obtained with a Geometrics Model G-886 proton precession magnetometer towed ~500 m astern. Magnetic data were recorded during transits at

1-min intervals on navigation files produced by WINFROG navigation software. The data were reduced to magnetic anomalies at ODP/TAMU (Texas A&M University) after Leg 183.

SEISMIC STRATIGRAPHY

Correlation of borehole results with MCS reflection data requires relating lithostratigraphy and physical properties of sediments and hard rocks to seismic reflections. To do so, we use one-dimensional synthetic seismograms created from density and velocity logs, MST data, and downhole wireline logs. We treat the relatively noisy core and MST data with a robust-mode filter employing a 5-m window, using GMT software (Wessel and Smith, 1995). This filter is a maximum likelihood probability estimator that calculates the mode (i.e., the most frequently occurring data value) within the given data window. In addition, the median of the filtered data is computed during filtering, and outliers with values 2.5 times greater than the L1 scale are replaced with the median ("robust" filter option). The L1 scale is defined as 1.4826 times the median absolute deviation (MAD), because, in a Gaussian distribution, the expected value for the MAD is the standard deviation $\sigma/1.4826$. Filtering noisy index properties data with various filters with and without the "robust" option shows that a robust-mode filter is the most efficient way to smooth the data and remove outlying data points. In most cases, a filter width of 3.5–5 m yields the best results.

If no check shots with the WST are available to determine transit time directly, we sum log transit times to create a record of two-way traveltime (TWT) vs. depth. The TWT log is linearly resampled using a sampling interval of 0.1–0.5 ms, depending on the sampling of the raw data. Downhole logs typically sample every 15 cm, whereas the sampling interval of physical properties measurements varies highly, depending on recovery. To avoid aliasing, linear resampling in TWT oversamples the data; other resampling methods (e.g., splines and near-neighbor) cause artifacts at data gaps. We then resample velocities and densities, using the TWT array, and multiply to obtain impedance.

We then calculate reflection coefficients from impedance contrasts. We compute a second time series of reflection coefficients including interbed multiples and transmission losses based on a Fourier domain method from Lavergne (1989), implemented using MATLAB. Both reflection coefficient time series are convolved with a Ricker wavelet with a peak frequency of 40 or 30 Hz, depending on the frequency content of the MCS data. We chose this wavelength by trial and error, as we found that wavelets with higher or lower peak frequencies do not match the MCS data as well.

REFERENCES

Archie, G.E., 1942. The electrical resistivity log as an aid in determining some reservoir characteristics. *J. Pet. Technol.,* 5:1–8.

ASTM, 1989. *Annual Book of ASTM Standards for Soil and Rock: Building Stones* (Vol. 4.08): *Geotextiles:* Philadelphia (Am. Soc. Testing and Mater.).

Aubele, J.C., Crumpler, L.S., and Elston, W.E., 1988. Vesicle zonation and vertical structure of basalt flows. *J. Volcanol. Geotherm. Res.,* 35:349–374.

Balsam,W.L. and Damuth, J.E., in press. Further investigations of shipboard vs. shore-based spectral data: implications for interpreting Leg 164 sediment composition. *In* Paull, C.K., Matsumoto, R., Wallace, P., and Dillon, W.P. (Eds.), *Proc. ODP, Sci. Results,* 164: College Station, TX (Ocean Drilling Program).

Balsam, W.L., Damuth, J.E., and Schneider, R.R., 1997. Comparison of shipboard vs. shore-based spectral data from Amazon Fan cores: implications for interpreting sediment composition. *In* Flood, R.D., Piper, D.J.W., Klaus, A., and Peterson, L.C. (Eds.), *Proc. ODP, Sci. Results,* 155: College Station, TX (Ocean Drilling Problem), 193–215.

Balsam, W.L., Deaton, B.C., and Damuth, J.E., 1998. The effects of water content on diffuse reflectance measurements of deep-sea core samples: an example from ODP Leg 164 sediments. *Mar. Geol.,* 149:177–189.

Berggren, W.A., 1992a. Neogene planktonic foraminifer magnetobiostratigraphy of the southern Kerguelen Plateau (Sites 747, 748, and 751). *In* Wise, S.W., Jr., Schlich, R., et al., *Proc. ODP, Sci. Results,* 120 (Pt. 2): College Station, TX (Ocean Drilling Program), 631–647.

————, 1992b. Paleogene planktonic foraminifer magnetobiostratigraphy of the Southern Kerguelen Plateau (Sites 747–749). *In* Wise, S.W., Jr., Schlich, R., et al., *Proc. ODP, Sci. Results,* 120 (Pt. 2): College Station, TX (Ocean Drilling Program), 551–568.

Berggren, W.A., Kent, D.V., and Flynn, J.J., 1985. Jurassic to Paleogene, Part 2. Paleogene geochronology and chronostratigraphy. *In* Snelling, N.J. (Ed.), *The Chronology of the Geological Record.* Geol. Soc. London Mem., 10:141–195.

Berggren, W.A., Kent, D.V., Swisher, C.C., III, and Aubry, M.-P., 1995. A revised Cenozoic geochronology and chronostratigraphy. *In* Berggren, W.A., Kent, D.V., Aubry, M.-P., and Hardenbol, J. (Eds.), *Geochronology, Time Scales and Global Stratigraphic Correlation.* Spec. Publ.—Soc. Econ. Paleontol. Mineral. (Soc. Sediment. Geol.), 54:129–212.

Blum, P., 1997, Physical properties handbook: a guide to the shipboard measurement of physical properties of deep-sea cores. *ODP Tech. Note,* 26 [Online]. Available from World Wide Web: <**http://www-odp.tamu.edu/publications/tnotes/tn26/INDEX.HTM**>.

Bown, P.R., Rutledge, D.C., Crux, J.A., and Gallagher, L.T., 1998. Lower Cretaceous. *In* Bown, P.R. (Ed.), *Calcareous Nannofossil Biostratigraphy:* Dordvecht (Kluwer Academic Publishers), 92–131.

Boyce, R.E., 1976. Definitions and laboratory techniques of compressional sound velocity parameters and wet-water content, wet-bulk density, and porosity parameters by gravimetric and gamma-ray attenuation techniques. *In* Schlanger, S.O., Jackson, E.D., et al., *Init. Repts. DSDP,* 33: Washington (U.S. Govt. Printing Office), 931–958.

Bralower, T. J., 1992. Aptian-Albian calcareous nannofossil biostratigraphy of ODP Site 763 and the correlation between high- and low-latitude zonations. *In* Duncan, R.A., Rea, D.K., Kidd, R.B., von Rad, U., and Weissel, J.K. (Eds.), *Synthesis of Results from Scientific Drilling in the Indian Ocean.* Geophys. Monogr., Am. Geophys. Union, 70:245–369.

Bralower, T.J., Leckie, R.M., Sliter, W.V., and Thierstein, H.R., 1995. An integrated Cretaceous microfossil biostratigraphy. *In* Scholle, P.A. (Ed.), *Geochronology, Time Scales,*

and Global Stratigraphic Correlation. Spec. Publ.—Soc. Econ. Paleontol. Mineral., 54:65–79.

Bralower, T.J., Sliter, W.V., Arthur, M.A., Leckie, R.M., Allard, D.J., and Schlanger, S.O., 1993. Dysoxic/anoxic episodes in the Aptian-Albian (Early Cretaceous). *In* Pringle, M.S., Sager, W.W., Sliter, M.V., and Stein, S. (Eds.), *The Mesozoic Pacific: Geology, Tectonics, and Volcanism*. Geophys. Monogr., Am. Geophys. Union, 77:5–37.

Bukry, D., 1973. Low-latitude coccolith biostratigraphic zonation. *In* Edgar, N.T., Saunders, J.B., et al., *Init. Repts. DSDP,* 15: Washington (U.S. Govt. Printing Office), 685–703.

————, 1975. Coccolith and silicoflagellate stratigraphy, northwestern Pacific Ocean, Deep Sea Drilling Project Leg 32. *In* Larson, R.L., Moberly, R., et al., *Init. Repts. DSDP,* 32: Washington (U.S. Govt. Printing Office), 677–701.

Cande, S.C., and Kent, D.V., 1995. Revised calibration of the geomagnetic polarity timescale for the Late Cretaceous and Cenozoic. *J. Geophys. Res.,* 100:6093–6095.

Caron, M., 1985. Cretaceous planktic foraminifera. *In* Bolli, H.M., Saunders, J.B., and Perch-Nielsen, K. (Eds), *Plankton Stratigraphy:* Cambridge (Cambridge Univ. Press), 17–86.

Cita, M.B., Coccioni, R., Edwards, A.R., Monechi, S., Morgans, H.E.G., Strong, C.P., Watkins, D.K., and Webb, P.-N., 1997. Nannofossils and foraminifera. *In* Hannah, M.J., and Raine, J.I. (Eds.), *Southern Ocean Late Cretaceous/Early Cenozoic Biostratigraphic Datums*. Inst. Geol. Nucl. Sci., Sci. Rep., 97/4:5–10.

Crisp, J., and Baloga, S.M., 1994. Influence of crystallization and entrainment of cooler material on the emplacement of basaltic aa flows. *J. Geophys. Res.,* 99:11819–11831.

Crisp, J., Cashman, K.V., Bonini, J.A., Hougen, S.B., and Pieri, D.C., 1994. Crystallization history of the 1984 Mauna Loa lava flow. *J. Geophys. Res.,* 99:7177–7198.

Davis, E.E., Villinger, H., MacDonald, R.D., Meldrum, R.D., and Grigel, J., 1997. A robust rapid-response probe for measuring bottom-hole temperatures in deep-ocean boreholes. *Mar. Geophys. Res.,* 19:267–281.

Demant, A., Cambray, H., Vandamme, D., and Leg 152 Shipboard Scientific Party, 1995. Lithostratigraphy of the volcanic sequences at Hole 917A, Leg 152, Southeast Greenland margin. *J. Geol. Soc. London,* 152:943–946.

Eberli, G.P., Swart, P.K., Malone, M.J., et al., 1997. *Proc. ODP, Init. Repts.,* 166: College Station, TX (Ocean Drilling Program).

Ellis, D.V., 1987. *Well Logging for Earth Scientists:* New York (Elsevier).

Erba, E., Premoli Silva, I., and Watkins, D.K., 1995. Cretaceous calcareous plankton biostratigraphy of Sites 872 through 879. *In* Haggerty, J.A., Premoli Silva, I., Rack, F., and McNutt, M.K. (Eds.), *Proc. ODP, Sci. Results,* 144: College Station, TX (Ocean Drilling Program), 157–169.

Fisher, R.V., and Schmincke, H.-U., 1984. *Pyroclastic Rocks:* New York (Springer-Verlag).

Gersonde, R., Hodell, D.A., Blum, P., et al., 1999. *Proc. ODP, Init. Repts.,* 177: College Station, TX (Ocean Drilling Program).

Goff, F., 1996. Vesicle cylinders in vapor-differentiated basalt flows. *J. Volcanol. Geotherm. Res.,* 97:167–185.

Goldberg, D., 1997. The role of downhole measurements in marine geology and geophysics. *Rev. Geophys.,* 35:315–342.

Govindaraju, K., 1989. 1989 compilation of working values and sample description for 272 geostandards. *Geostand. Newsl.,* 13 (spec. iss.).

Gradstein, F.M., Agterberg, F.P., Ogg, J.G., Hardenbol, J., van Veen, P., Thierry, J., and Huang, Z., 1994. A Mesozoic time scale. *J. Geophys. Res.,* 99:24051–24074.

————, 1995. A Triassic, Jurassic and Cretaceous time scale. *In* Berggren, W.A., Kent, D.V., and Aubry, M.P., and Hardenbol, J. (Eds.), *Geochronology, Time Scales and Global Stratigraphic Correlation*. Spec. Publ.—Soc. Econ. Paleontol. Mineral., 54:95–126.

Gregg, T.K.P., and Fink, J.H., 1995. Quantification of submarine lava-flow morphology through analog experiments. *Geology,* 23:73–76.

Harwood, D.M., and Maruyama, T., 1992. Middle Eocene to Pleistocene diatom biostratigraphy of Southern Ocean sediments from the Kerguelen Plateau, Leg 120. *In* Wise, S.W., Jr., Schlich, R., et al., *Proc. ODP, Sci. Results,* 120: College Station, TX (Ocean Drilling Program), 683–733.

Hiscott, R.N., Colella, A., Pezard, P., Lovell, M.A., and Malinverno, A., 1992. Sedimentology of deep-water volcaniclastics, Oligocene Izu-Bonin forearc basin, based on formation microscanner images. *In* Taylor, B., Fujioka, K., et al., *Proc. ODP, Sci. Results,* 126: College Station, TX (Ocean Drilling Program), 75–96.

Hon, K., Kauahikaua, J.P., Denlinger, R., and Mackay, K., 1994. Emplacement and inflation of pahoehoe sheet flows: observations and measurements of active lava flows on Kilauea, Hawaii. *Geol. Soc. Am. Bull.,* 106:351–370.

Huber, B.T., 1990. Maestrichtian planktonic foraminifer biostratigraphy of the Maud Rise (Weddell Sea, Antarctica): ODP Leg 113 Holes 689B and 690C. *In* Barker, P.F., Kennett, J.P., et al., *Proc. ODP, Sci. Results,* 113: College Station, TX (Ocean Drilling Program), 489–513.

————, 1991. Paleogene and early Neogene planktonic foraminifer biostratigraphy of Sites 738 and 744, Kerguelen Plateau (southern Indian Ocean). *In* Barron, J., Larsen, B., et al., *Proc. ODP, Sci. Results,* 119: College Station, TX (Ocean Drilling Program), 427–449.

Huber, B.T., 1992. Upper Cretaceous planktic foraminiferal biozonation for the Austral Realm. *Mar. Micropaleontol.,* 20:107–128.

Huber, B.T., and Watkins, D.K., 1992. Biogeography of Campanian-Maastrichtian calcareous plankton in the region of the Southern Ocean: paleogeographic and paleoclimatic implications. *In* Kennett, J.P., and Warnke, D.A. (Eds.), *The Antarctic Paleoenvironment: A Perspective on Global Change.* Am. Geophys. Union, Antarct. Res. Ser., 56:31–60.

Jenkins, D.G., 1971. New Zealand Cenozoic planktonic foraminifera. *N.Z. Geol. Surv. Paleontol. Bull.,* 42:1–278.

Jenkins, D.G., and Srinivasan, M.S., 1986. Cenozoic planktonic foraminifers from the equator to the sub-antarctic of the southwest Pacific. *In* Kennett, J.P., von der Borch, C.C., et al., *Init. Repts. DSDP,* 90: Washington (U.S. Govt. Printing Office), 795–834.

Jochum, K.P., Seufert, H.M., and Thirlwall, M.F., 1990. High-sensitivity Nb analysis by spark-source mass spectrometry (SSMS) and calibration of XRF Nb and Zr. *Chem. Geol.,* 81:1–16.

Kennett, J.P., and Srinivasan, M.S., 1983. *Neogene Planktonic Foraminifera: A Phylogenetic Atlas:* Stroudsburg, PA (Hutchinson Ross).

Kirschvink, J.L., 1980. The least-squares line and plane and the analysis of palaeomagnetic data. *Geophys. J. R. Astron. Soc.,* 62:699–718.

Krasheninnikov, V.A., and Basov, I.A., 1983. Stratigraphy of Cretaceous sediments of the Falkland Plateau based on planktonic foraminifers, Deep Sea Drilling Project, Leg 71. *In* Ludwig, W.J., Krasheninnikov, V.A., et al., *Init. Repts. DSDP,* 71: Washington (U.S. Govt. Printing Office), 789–820.

Lamont-Doherty Earth Observatory-Borehole Research Group, 1994. *Wireline Logging Services Guide:* Lamont-Doherty Earth Observatory-Borehole Research Group.

Larsen, H.C., Saunders, A.D., Clift, P.D., et al., 1994. *Proc. ODP, Init. Repts.,* 152: College Station, TX (Ocean Drilling Program).

Lavergne, M., 1989, *Seismic Methods:* Dordrecht (Kluwer Academic).

Leckie, R.M., 1984. Mid-Cretaceous planktonic foraminiferal biostratigraphy off Central Morocco, Deep Sea Drilling Project Leg 79, Sites 545 and 547. *In* Hinz, K., Winterer, E.L., et al., *Init. Repts. DSDP,* 79: Washington (U.S. Govt. Printing Office), 579–620.

Lovell, M.A., Harvey, PK., Brewer, T.S., Williams, C., Jackson, P.D., and Williamson, G., 1998. Application of FMS images in the Ocean Drilling Program: an overview. *In* Cramp, A., MacLeod, C.J., Lee, S.V., and Jones, E.J.W. (Eds.), *Geological Evolution*

of Ocean Basins: Results from the Ocean Drilling Program. Geol. Soc. Spec. Publ. London, 131:287–303.

Macdonald, G.A., 1953. Pahoehoe, aa, and block lava. *Am. J. Sci.,* 251:169–191.

MacKenzie, W.S., Donaldson, C.H., and Guilford, C., 1982. *Atlas of Igneous Rocks and their Textures:* Harlow, England (Longman).

Martini, E., 1971. Standard Tertiary and Quaternary calcareous nannoplankton zonation. *In* Farinacci, A. (Ed.), *Proc. 2nd Int. Conf. Planktonic Microfossils Roma:* Rome (Ed. Tecnosci.), 2:739–785.

Martini, E., and Müller, C., 1986. Current Tertiary and Quaternary calcareous nannoplankton stratigraphy and correlations. *Newsl. Stratigr.,* 16:99–112.

Mazzullo, J.M., Meyer, A., and Kidd, R.B., 1988. New sediment classification scheme for the Ocean Drilling Program. *In* Mazzullo, J., and Graham, A.G. (Eds.), *Handbook for Shipboard Sedimentologists. ODP Tech. Note*, 8:45–67.

McCartney, K., and Harwood, D.M., 1992. Silicoflagellates from Leg 120 on the Kerguelen Plateau, southeast Indian Ocean. *In* Wise, S.W., Jr., Schlich, R., et al., *Proc. ODP, Sci. Results,* 120: College Station, TX (Ocean Drilling Program), 811–831.

McCartney, K., and Wise, S.W., Jr., 1990. Cenozoic silicoflagellates and ebridians from ODP Leg 113: biostratigraphy and notes on morphologic variability. *In* Barker, P.F., Kennett, J.P., et al., *Proc. ODP, Sci. Results,* 113: College Station, TX (Ocean Drilling Program), 729–760.

McKee, E.D., and Weir, G.W., 1953. Terminology for stratification and cross-stratification in sedimentary rocks. *Geol. Soc. Am. Bull.,* 64:381–390.

Mohr, B.A.R., and Gee, C.T., 1992. Late Cretaceous palynofloras (sporomorphs and dinocysts) from the Kerguelen Plateau, southern Indian Ocean (Sites 748 and 750). *In* Wise, S.W., Jr., Schlich, R., et al., *Proc. ODP, Sci. Results,* 120: College Station, TX (Ocean Drilling Program), 281–306.

Moore, C.L., Cas, R.A.F., Scutter, C., and Yamagishi, H., 1996. Fragmentation and depositional processes during construction of a submarine volcanic edifice, Kabuto Cape, Hokkaido, Japan. *Eos,* 77:W125.

Munsell Color Company, Inc., 1971. *Munsell Soil Color Charts:* Baltimore, MD (Munsell).

Norrish, K., and Hutton, J.T., 1969. An accurate X-ray spectrographic method for the analysis of a wide range of geological samples. *Geochim. Cosmochim. Acta,* 33:431–453.

Okada, H., and Bukry, D., 1980. Supplementary modification and introduction of code numbers to the low-latitude coccolith biostratigraphic zonation (Bukry, 1973; 1975). *Mar. Micropaleontol.,* 5:321–325.

Olsson, R.K., Hemleben, C., Berggren, W.A., and Huber, B.T. (Eds.), 1999. *Atlas of Paleocene Planktonic Forminifera*. Smithsonian Contrib. Paleobiol., 85.

Peirce, J., Weissel, J., et al., 1989. *Proc. ODP, Init. Repts.,* 121: College Station, TX (Ocean Drilling Program).

Perch-Nielsen, K., 1985a. Mesozoic calcareous nannofossils. *In* Bolli, H.M., Saunders, J.B., and Perch-Nielsen, K. (Eds.), *Plankton Stratigraphy:* Cambridge (Cambridge Univ. Press), 329–426.

————, 1985b. Silicoflagellates. *In* Bolli, H.M., Saunders, J.B., and Perch-Nielsen, K. (Eds.), *Plankton Stratigraphy:* Cambridge (Cambridge Univ. Press), 811–846.

Peterson, D.W., and Tilling, R. I., 1980. Transition of basaltic lava from pahoehoe to aa, Kilauea Volcano, Hawaii: field observations and key factors. *J. Volcanol. Geotherm. Res*. 7:271–293.

Pospichal, J., Wei, W., and Wise, S.W., Jr., 1992. Probing the limits of nannofossil stratigraphic resolution in the Southern High Latitudes. *Mem. Sci. Geol.,* 43:115–131.

Quilty, P.G., 1992. Upper Cretaceous planktonic foraminifers and biostratigraphy, Leg 120, southern Kerguelen Plateau. *In* Wise, S.W., Jr., Schlich, R., et al., *Proc. ODP, Sci. Results,* 120: College Station, TX (Ocean Drilling Program), 371–392.

Ramsay, D.C., Colwell, J.B., Coffin, M.F., Davies, H.L., Hill, P.J., Pigram, C.J., and Stagg, H.M.J., 1986. New findings from the Kerguelen Plateau. *Geology,* 14:589–593.

Reynolds, R.C., Jr., 1963. Matrix corrections in trace element analysis by X-ray fluorescence: estimation of the mass absorption coefficient by Compton scattering. *Am. Mineral.,* 48:1133–1143.

————, 1967. Estimation of mass absorption coefficients by Compton scattering: improvements and extensions of the method. *Am. Mineral.,* 52:1493–1502.

Rider, M., 1996. *The Geological Interpretation of Well Logs* (2nd ed.): Caithness (Whittles Publishing).

Roth, P.H., 1978. Cretaceous nannoplankton biostratigraphy and oceanography of the northwestern Atlantic Ocean. *In* Benson, W.E., Sheridan, R.E., et al., *Init. Repts. DSDP,* 44: Washington (U.S. Govt. Printing Office), 731–759.

Rowland, S.K., and Walker, G.P.L., 1987. Toothpaste lava: characteristics and origin of a lava structural type transitional between pahoehoe and aa. *Bull. Volcanol.,* 49:631–641.

Sass, J.H., Kennelly, J.P., Jr., Smith, E.P., and Wendt, W.E., 1984. Laboratory line-source methods for the measurement of thermal conductivity of rocks near room temperature. *Open-File Rep.—U.S. Geol. Surv.,* 84–0091.

Schlich, R., Munschy, M., Boulanger, D., Cantin, B., Coffin, M.F., Durand, J., Humler, E., Li, Z.G., Savary, J., Schaming, M., and Tissot, J.D., 1988. Résultats préliminaires de la campagne océanographique de sismique reflexion multitraces MD47 dans le domaine sud du plateau de Kerguelen. *C. R. Acad. Sci. Ser. 2.,* 305:635–642.

Schlumberger, 1989. *Log Interpretation Principles/Applications:* Houston, TX (Schlumberger Wireline and Testing).

————, 1994. *IPL Integrated Porosity Lithology* (Schlumberger Wireline and Testing), SMP-9270.

————, 1995. *DSI—Dipole Sonic Imager:* (Schlumberger Wireline and Testing), SMP-5128.

Self, S., Keszthelyi, L., and Thordarson, T., 1998. The importance of pahoehoe. *Annu. Rev. Earth Planet. Sci,* 26:81–110.

Self, S., Thordarson, T., and Keszthelyi, L., 1997. Emplacement of continental flood basalt lava flows. *In* Mahoney, J.J., and Coffin, M. (Eds.), *Large Igneous Provinces: Continental, Oceanic, and Planetary Flood Volcanism.* Am. Geophys. Union., Geophys. Monogr., 100:381–410.

Serra, O., 1984. *Fundamentals of Well-Log Interpretation* (Vol. 1): *The Acquisition of Logging Data:* Dev. Pet. Sci., 15A: Amsterdam (Elsevier).

————, 1986. *Fundamentals of Well-Log Interpretation* (Vol. 2): *The Interpretation of Logging Data.* Dev. Pet. Sci., 15B.

————, 1989. *Formation MicroScanner Image Interpretation:* Houston (Schlumberger Educ. Services), SMP-7028.

Shepard, F., 1954. Nomenclature based on sand-silt-clay ratios. *J. Sediment. Petrol.,* 24:151–158.

Shipboard Scientific Party, 1991. Explanatory notes. *In* Davies, P.J., McKenzie, J.A., Palmer-Julson, A., et al., *Proc. ODP, Init. Repts.,* 133 (Pt. 1): College Station, TX (Ocean Drilling Program), 31–58.

————, 1992. Explanatory notes. *In* Parson, L., Hawkins, J., Allan, J., et al., *Proc. ODP, Init. Repts.,* 135: College Station, TX (Ocean Drilling Program), 49–79.

————, 1995. Explanatory notes. *In* Flood, R.D., Piper, D.J.W., Klaus, A., et al., *Proc. ODP, Init. Repts.,* 155: College Station, TX (Ocean Drilling Program), 47–81.

————, 1997. Explanatory notes. *In* Eberli, G.P., Swart, P.K., Malone, M.J., et al., *Proc. ODP, Init. Repts.,* 166: College Station, TX (Ocean Drilling Program), 43–65.

————, 1999a. Explanatory Notes. *In* Gersonde, R., Hodell, D.A., Blum, P., et al., *Proc. ODP, Init. Results,* 177, 1-57 [CD-ROM]. Available from: Ocean Drilling Program, Texas A&M University, College Station, TX 77845-9547, U.S.A.

————, 1999b. Explanatory Notes. *In* Barker, P.F., Camerlenghi, A., Acton, G.D., et al., *Proc. ODP, Init. Results,* 178, 1-66 [CD-ROM]. Available from: Ocean Drilling Program, Texas A&M University, College Station, TX 77845-9547, U.S.A.

Sissingh, W., 1977. Biostratigraphy of Cretaceous calcareous nannoplankton. *Geol. Mijnbouw,* 56:37–65.

Sliter, W.V., 1977. Cretaceous foraminifers from the southwestern Atlantic Ocean, Leg 36, Deep Sea Drilling Project. *In* Barker, P.F., Dalziel, I.W.D., et al., *Init. Repts. DSDP,* 36: Washington (U.S. Govt. Printing office), 519–573.

Srinivasan, M.S., and Kennett, J.P., 1981. Neogene planktonic foraminiferal biostratigraphy and evolution: equatorial to subantarctic, South Pacific. *Mar. Micropaleontol.,* 6:499–533.

Stott, L.D., and Kennett, J.P., 1990. Antarctic Paleogene planktonic foraminifer biostratigraphy: ODP Leg 113, Sites 689 and 690. *In* Barker, P.F., Kennett, J.P., et al., *Proc. ODP, Sci. Results,* 113: College Station, TX (Ocean Drilling Program), 549–569.

Thordarson, T., 1995. Volatile release and atmospheric effects of basaltic fissure eruptions [Ph.D. thesis]. Univ. of Hawaii at Manoa, Honolulu.

Toumarkine, M., and Luterbacher, H., 1985. Paleocene and Eocene planktic foraminifera. *In* Bolli, H.M., Saunders, J.B., and Perch-Nielsen, K. (Eds.), *Plankton Stratigraphy:* Cambridge (Cambridge Univ. Press), 87–154.

Vacquier, V., 1985. The measurement of thermal conductivity of solids with a transient linear heat source on the plane surface of a poorly conducting body. *Earth Planet. Sci. Lett.,* 74:275–279.

Von Herzen, R.P., and Maxwell, A.E., 1959. The measurement of thermal conductivity of deep-sea sediments by a needle-probe method. *J. Geophys. Res.,* 64:1557–1563.

Walker, D., 1973. Behavior of X-ray mass absorption coefficients near absorption edges: Reynold's method revisited. *Am. Mineral.,* 58:1069–1072.

Watkins, D.K., Wise, S.W., Jr., Pospichal, J.J., and Crux, J., 1996. Upper Cretaceous calcareous nannofossil biostratigraphy and paleoceanography of the Southern Ocean. *In* Moguilevsky, A., and Whatley, R. (Eds.), *Microfossils and Oceanic Environments:* Univ. of Wales (Aberystwyth Press), 355–381.

Wei, W., 1992. Paleogene chronology of Southern Ocean drill holes: an update. *In* Kennett, J.P., and Warnke, D.A. (Eds.), *The Antarctic Paleoenvironment: a Perspective on Global Change*. Antarct. Res. Ser., 56:75–96.

Wei, W., and Pospichal, J.J., 1991. Danian calcareous nannofossil succession at Site 738 in the southern Indian Ocean. *In* Barron, J., Larsen, B., et al., *Proc. ODP, Sci. Results,* 119: College Station, TX (Ocean Drilling Program), 495–512.

Wei, W., and Thierstein, H.R., 1991. Upper Cretaceous and Cenozoic calcareous nannofossils of the Kerguelen Plateau (southern Indian Ocean) and Prydz Bay (East Antarctica). *In* Barron, J., Larsen, B., et al., *Proc. ODP, Sci. Results,* 119: College Station, TX (Ocean Drilling Program), 467–494.

Wei, W., and Wise, S.W., Jr., 1990. Middle Eocene to Pleistocene calcareous nannofossils recovered by Ocean Drilling Program Leg 113 in the Weddell Sea. *In* Barker, P.F., Kennett, J.P., et al., *Proc. ODP, Sci. Results,* 113: College Station, TX (Ocean Drilling Program), 639–666.

————, 1992. Selected Neogene calcareous nannofossil index taxa of the Southern Ocean: biochronology, biometrics, and paleoceanography. *In* Wise, S.W., Jr., Schlich, R., et al., *Proc. ODP, Sci. Results,* 120: College Station, TX (Ocean Drilling Program), 523–537.

Wentworth, C.K., 1922. A scale of grade and class terms of clastic sediments. *J. Geol.,* 30:377–392.

Wessel, P., and Smith, W.H.F., 1995. New version of the Generic Mapping Tools released. *Eos,* 76:329.

Wise, S.W., Jr., 1983. Mesozoic and Cenozoic calcareous nannofossils recovered by Deep Sea Drilling Project Leg 71 in the Falkland Plateau region, Southwest Atlantic Ocean. *In* Ludwig, W.J., Krasheninnikov, V.A., et al., *Init. Repts. DSDP,* 71 (Pt. 2): Washington (U.S. Govt. Printing Office), 481–550.

Zijderveld, J.D.A., 1967. AC demagnetization of rocks: analysis of results. *In* Collinson, D.W., Creer, K.M., and Runcorn, S.K. (Eds.), *Methods in Paleomagnetism:* New York (Elsevier), 254–286.

Figure F1. Examples of numbered core sections.

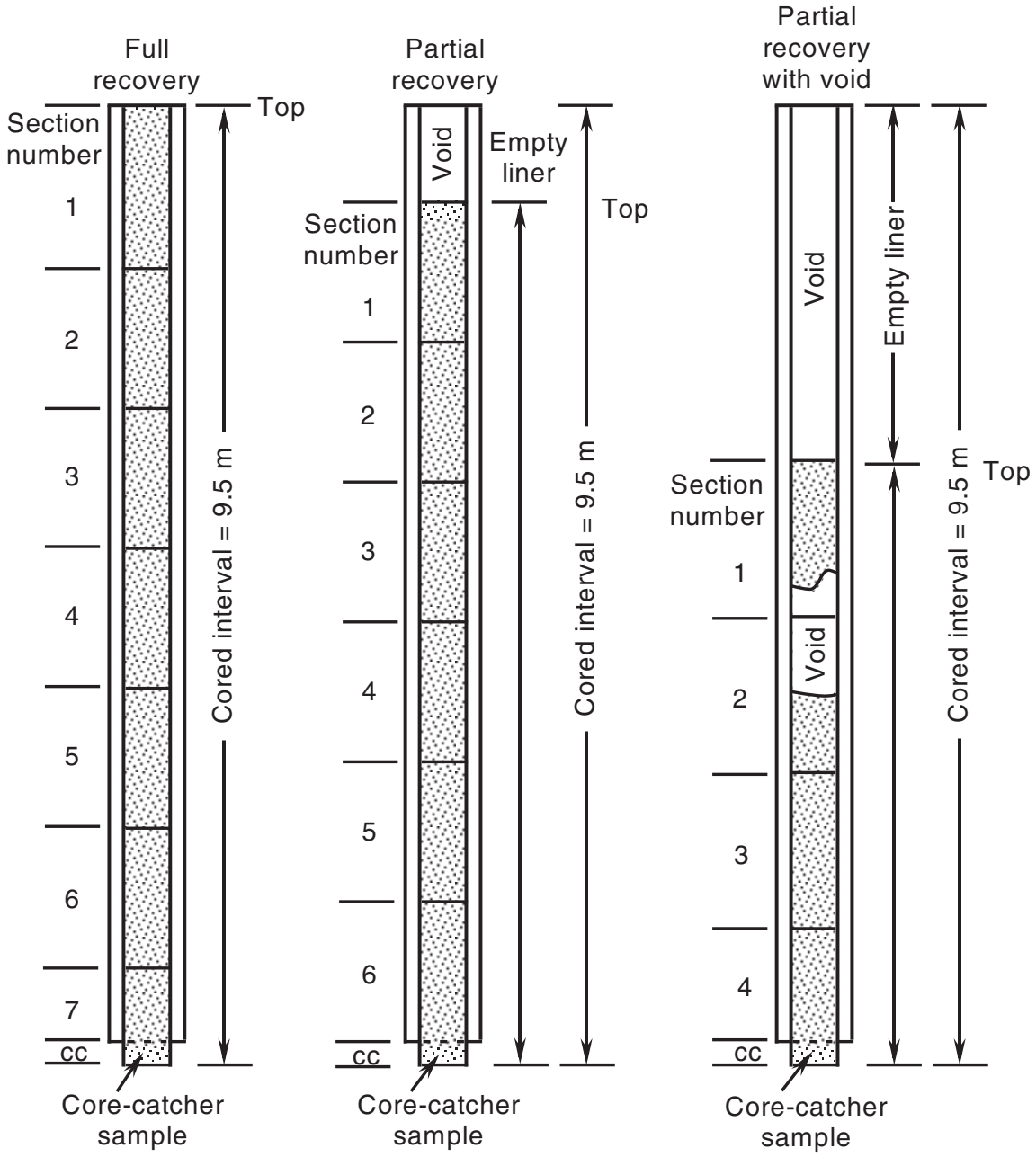

Figure F2. Bathymetry of the Kerguelen Plateau. Solid stars = previous ODP drill sites that recovered igneous basement; open stars = sites that bottomed in sediment. Circles = proposed drill sites (KIP) for Leg 183. Seismic lines used to select the sites = black lines with cruise identifiers (GA = *Gallieni;* MD = *Marion Dufresne;* RS = *Rig Seismic*). Contour interval is 500 m.

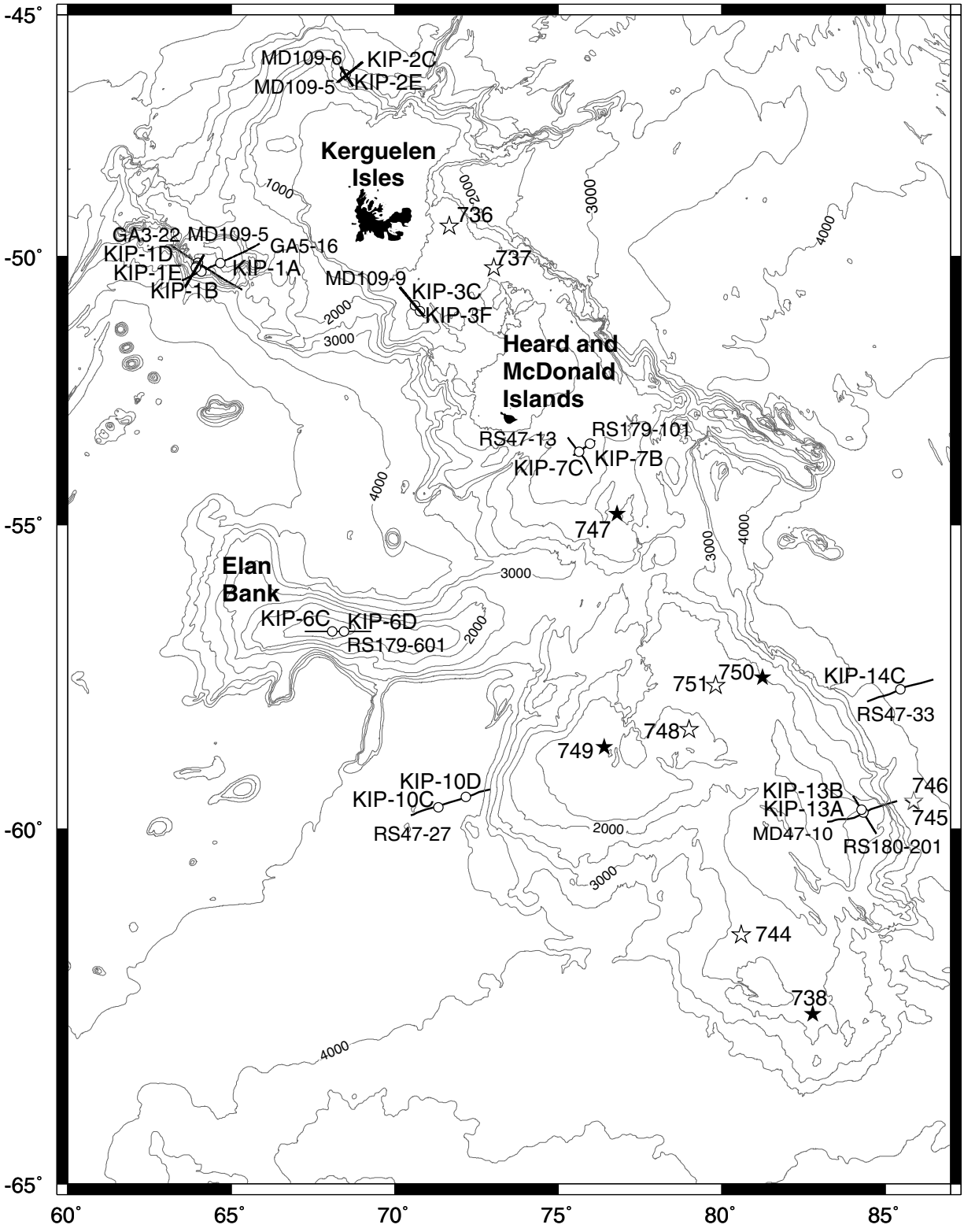

Figure F3. Key to symbols used to represent lithology, sedimentary structures, accessories, bioturbation, and drilling disturbance in the barrel sheets.

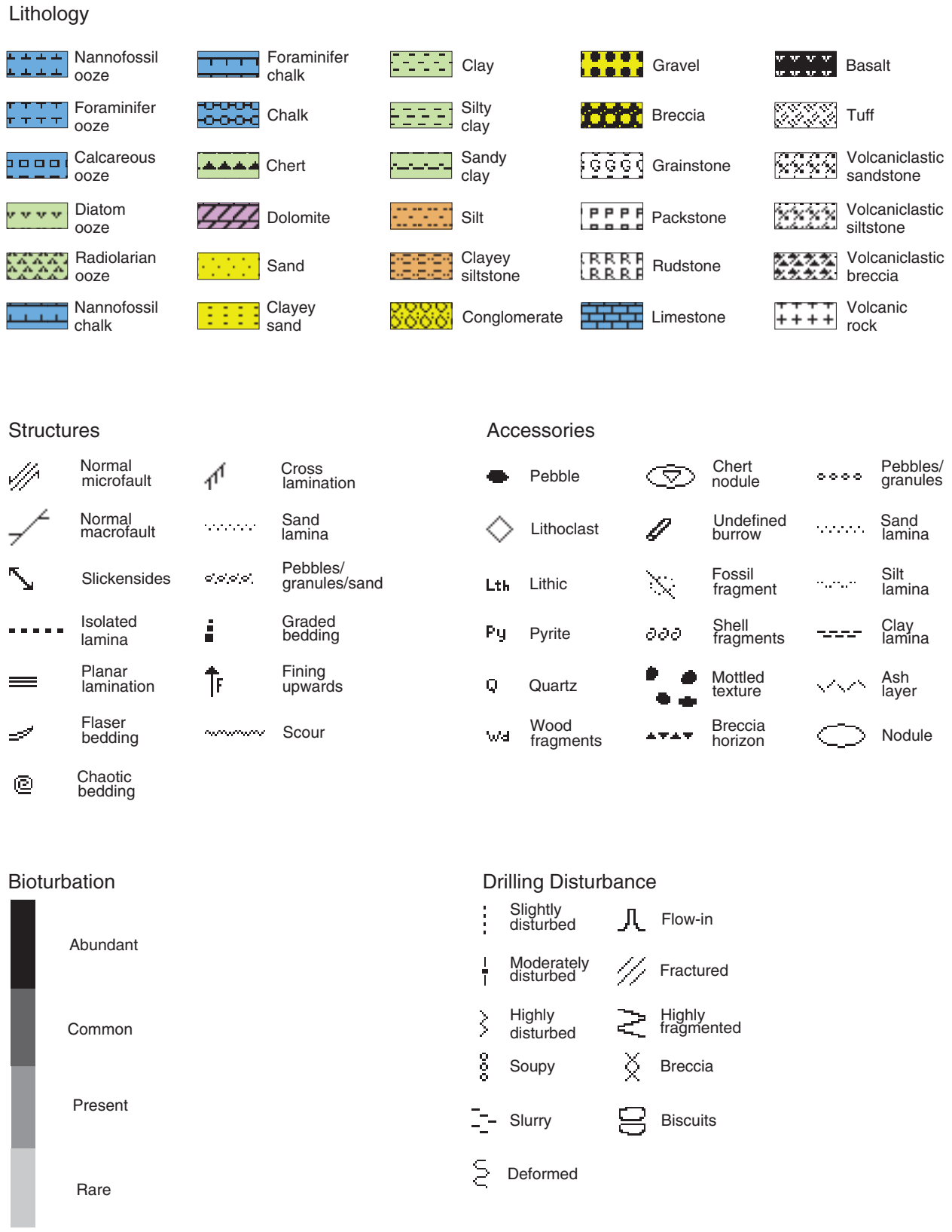

Figure F4. A. Textural classification scheme for siliciclastic sediments modified from Shepard (1954) by subdivision of the central triangular field into muddy sand and sandy mud; the term "mud" is used here for a mixture of silt and clay (Shipboard Scientific Party, 1995). The sand-, silt-, and clay-sized fractions are defined using the Wentworth (1922) grade scale. Symbols used on the Shepard triangle are the same as shown in Figure F3, p. 57. **B.** Classification of sediments composed of mixtures of biogenic and siliciclastic components. In this scheme the names shown for microfossil components and the siliciclastic fraction are examples only (i.e., placeholders), and can be replaced by any valid textural name (for siliciclastic fraction) or microfossil name.

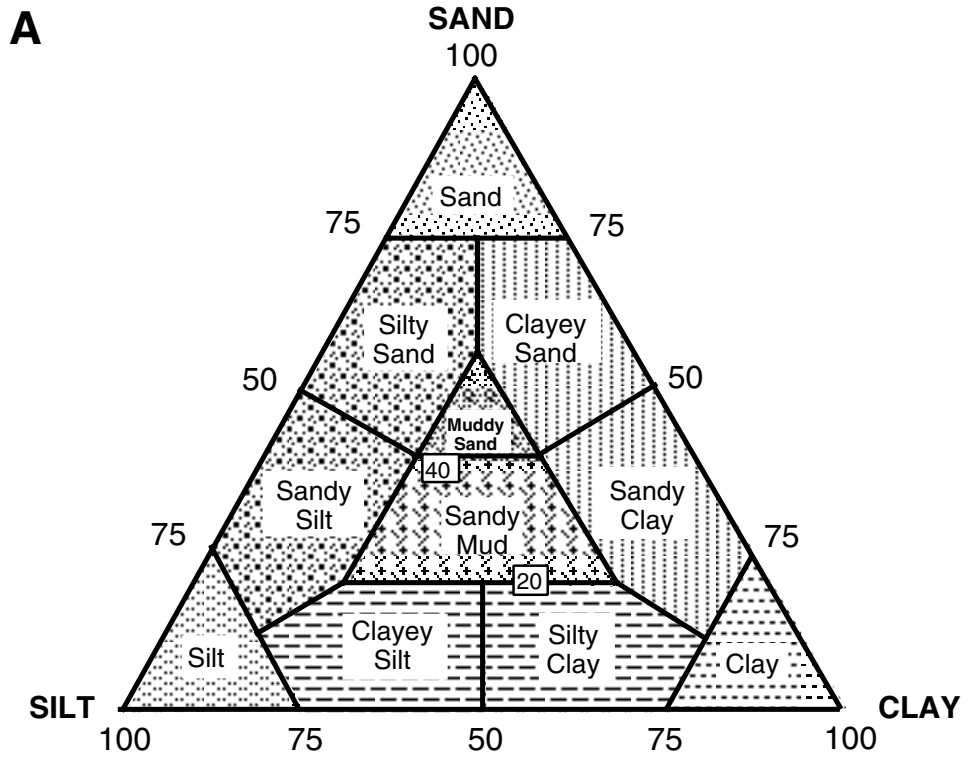

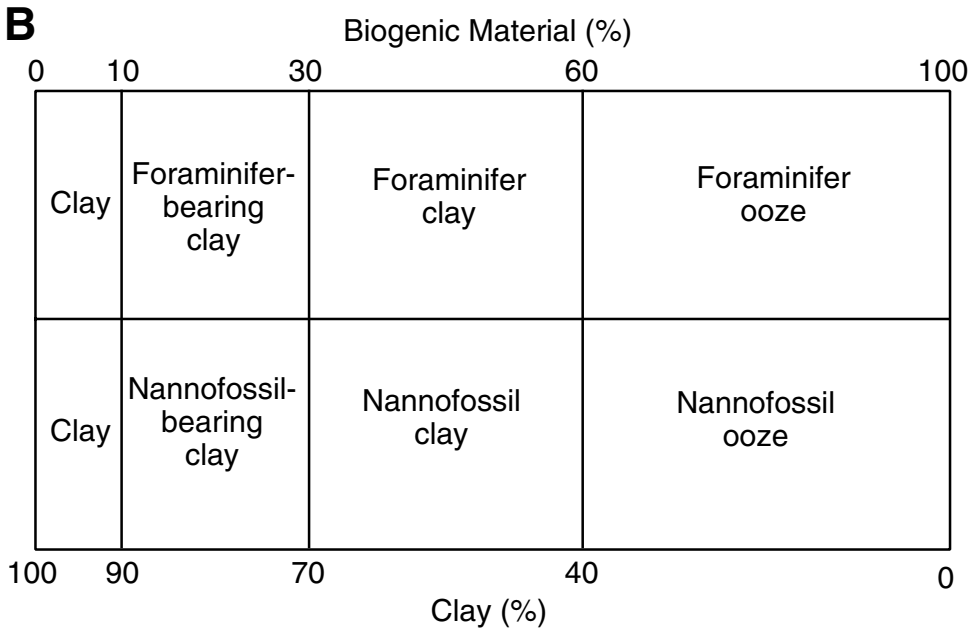

Figure F5. Neogene time scale and biostratigraphic datums used during Leg 183 for Broken Ridge Site 1141 (after Kennett and Srinivasan, 1983; Berggren et al., 1995; Erba et al., 1995). The temperate Miocene planktonic foraminifer zonation is adopted from Kennett and Srinivasan (1983). Dashed lines between zones represent uncertain datums scaled to the low-latitude zonation and time scale of Berggren et al. (1995). T = top/last occurrence, B = base/first occurrence. (**Figure shown on next page.**)

Figure F5. (Caption on previous page.)

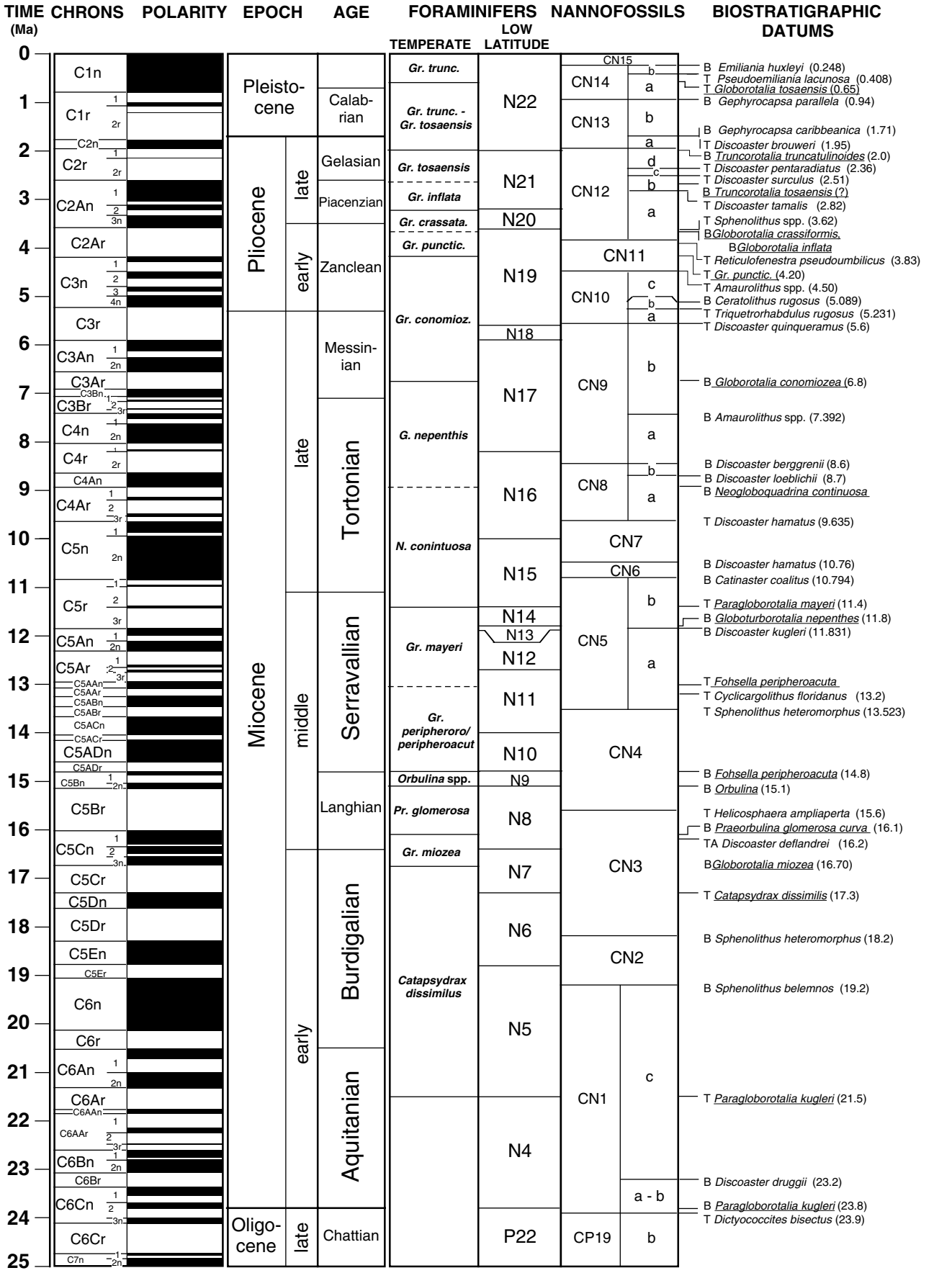

Figure F6. Holocene through Late Cretaceous time scale and biostratigraphic datums used during Leg 183 for the Kerguelen Plateau Sites 1135–1140 (modified from Berggren et al., 1995; Gradstein et al., 1994; Erba et al., 1995). High-latitude zonations used on Leg 183 vs. low-latitude zonations are indicated under "Leg 183" and "Low Lat.," respectively, for foraminifers and nannofossils. High-latitude biostratigraphic datum and age correlations are indicated in bold type under "Biostratigraphic Datums"; foraminiferal datums are underlined. Planktonic foraminifer zonations adopted from Berggren (1992: Neogene Kerguelen); Stott and Kennett (1990: Antarctic Paleogene; modified by Huber, 1991, and Berggren, 1992); Cita et al. (1997: Southern Ocean Late Cretaceous [after Huber, 1992]). Nannofossil zonations adopted from Wise (1983: Antarctic Oligocene to mid-middle Eocene; modified by Wei and Wise, 1990; and Wei and Thierstein, 1991, and calibrated against magnetostratigraphy by Wei, 1992); Wei and Pospichal (1991: Antarctic Paleocene ["NA" zones]); Watkins et al. (1996: Austral Upper Cretaceous [see also Cita el al., 1997]); and Bralower (1992: Albian [Lower Cretaceous]; also see Bralower et al., 1993, 1995). Note that some of the high-latitude datums are only correlated to magnetic chrons in the literature. Dashed zonal boundaries indicate uncertain datum levels. T = top/last occurrence, B = base/first occurrence. (**Figure on next six pages.**)

Figure F6. (Caption on previous page.)

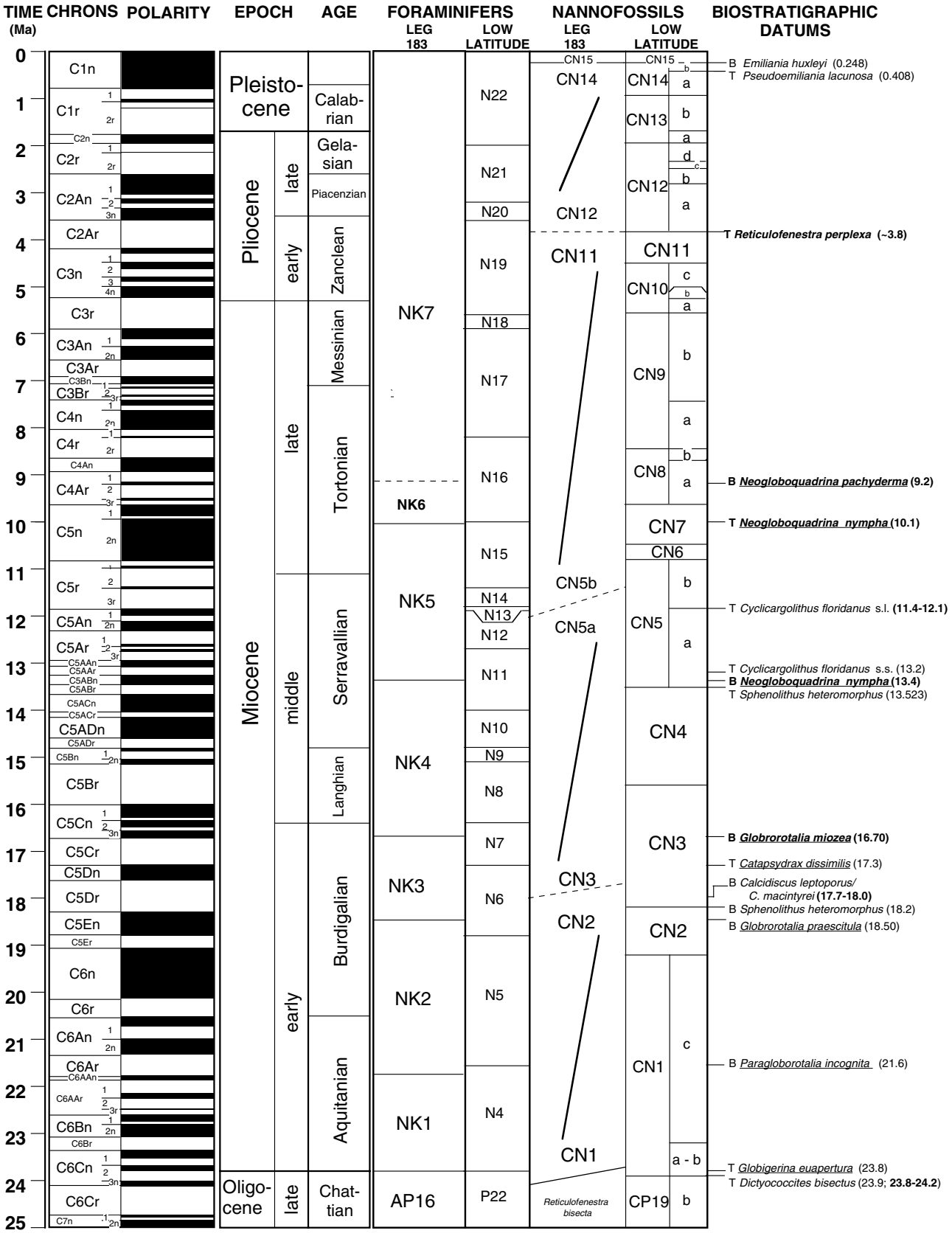

Figure F6 (continued).

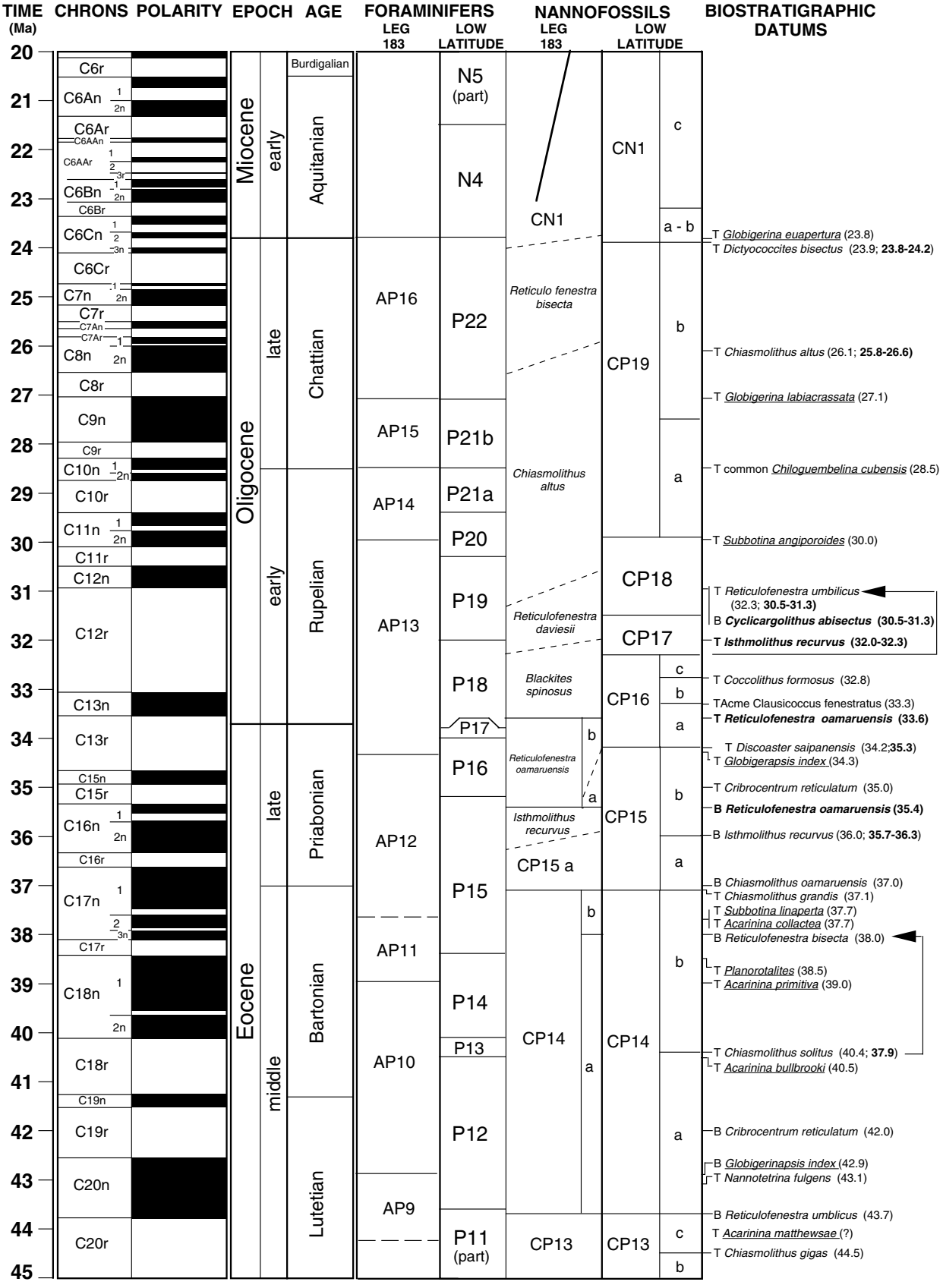

Figure F6 (continued).

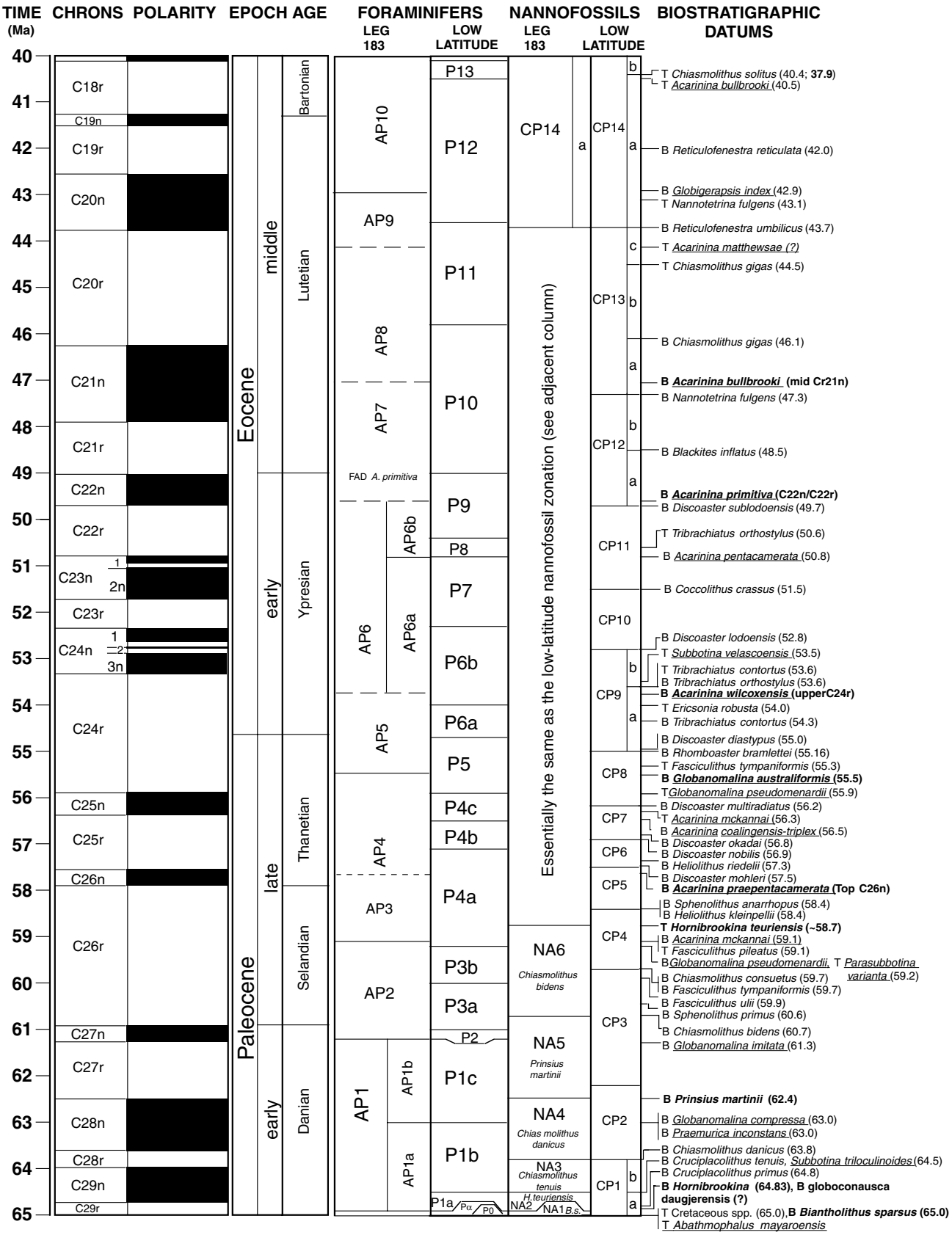

Figure F6 (continued).

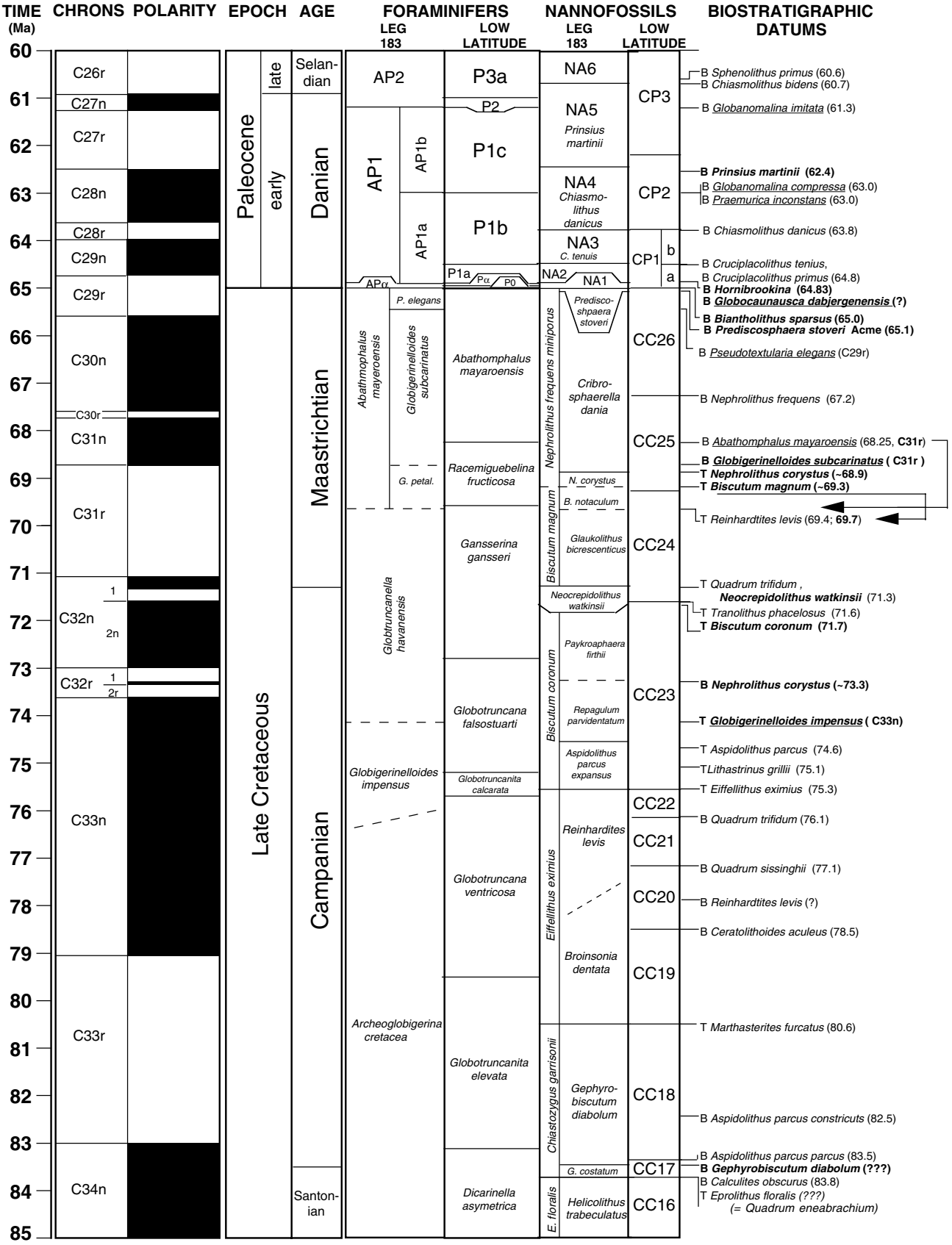

Figure F6 (continued).

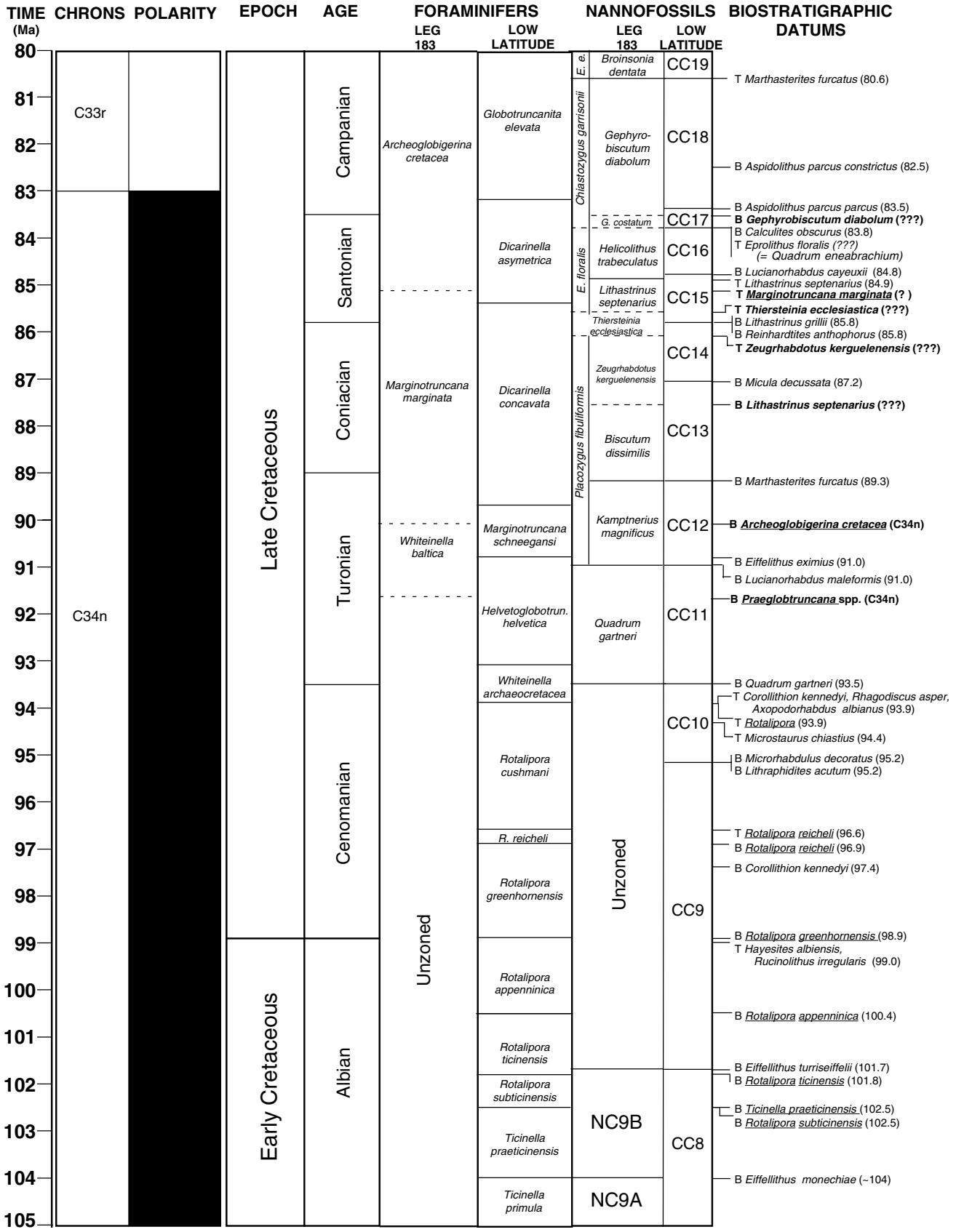

Figure F6 (continued).

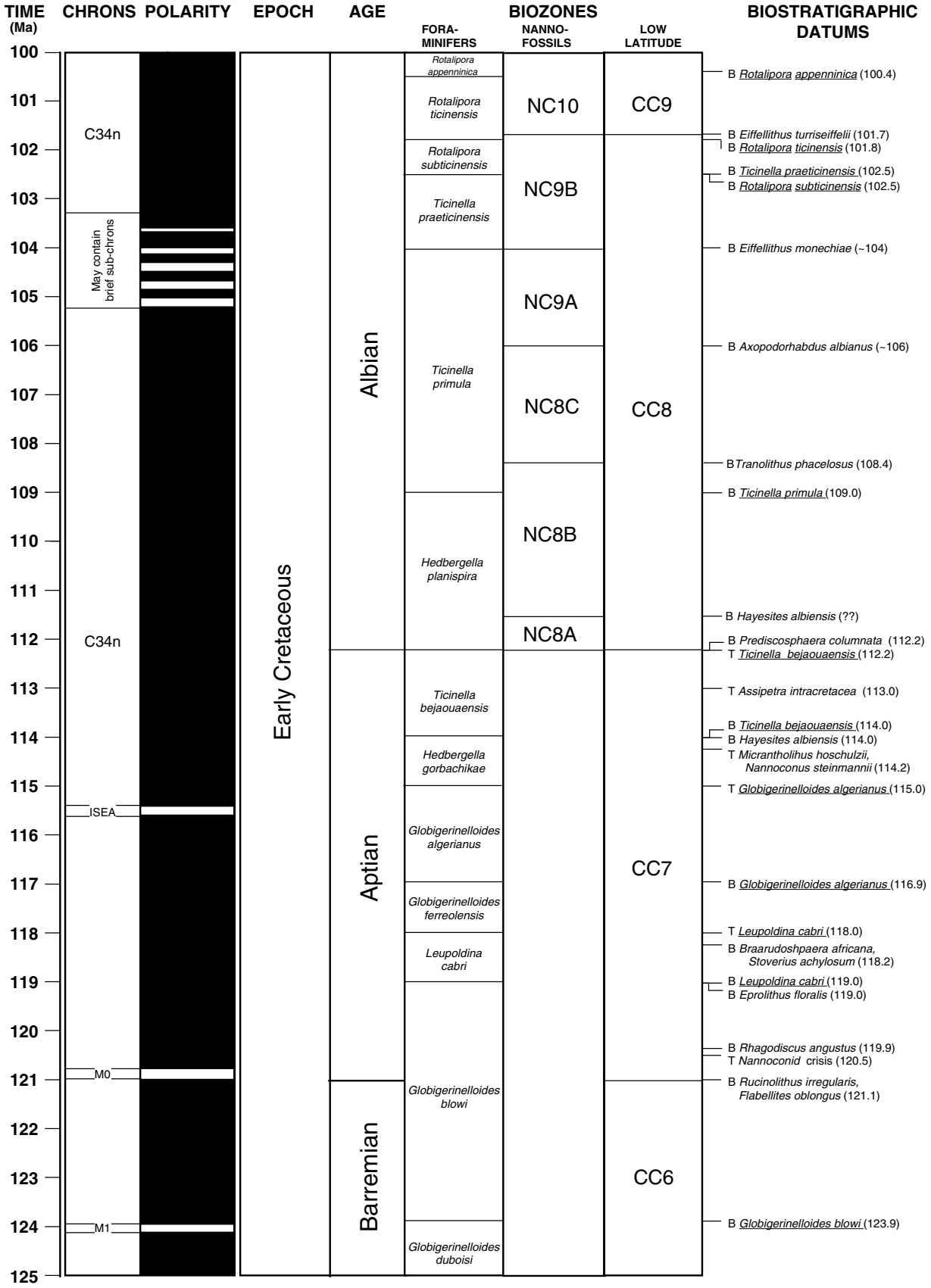

Figure F7. Holocene to middle Miocene diatom zones and datums used during Leg 183 (fig. F10 from Shipboard Scientific Party, 1999b). Geomagnetic time scale of Berggren et al. (1995). T = top/last occurrence, B = base/first occurrence. Age references are from Harwood and Maruyama (1992).

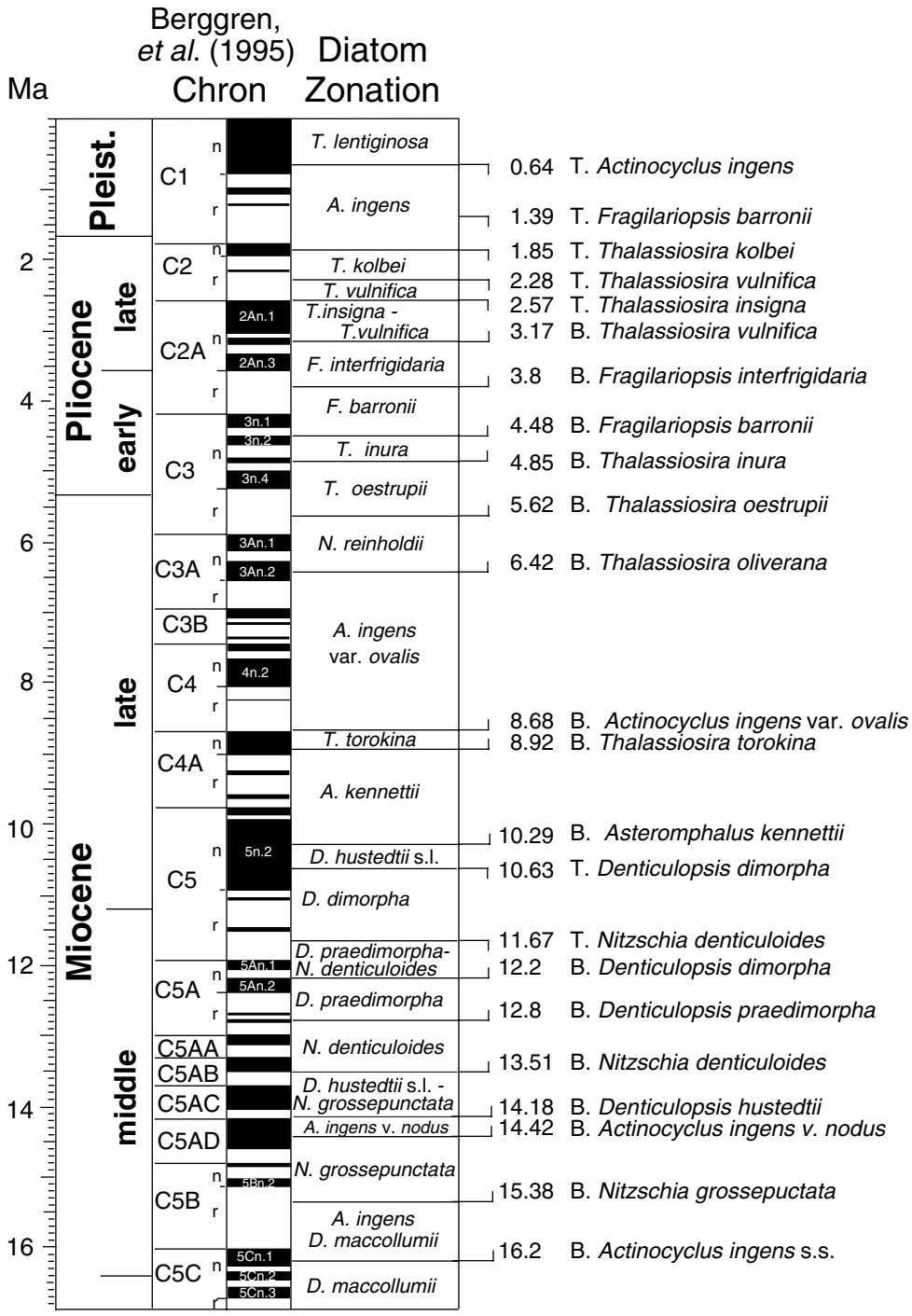

Figure F8. Leg 177 diatom zonation and stratigraphic ranges of key diatom species (fig. F9 from Shipboard Scientific Party, 1999a).

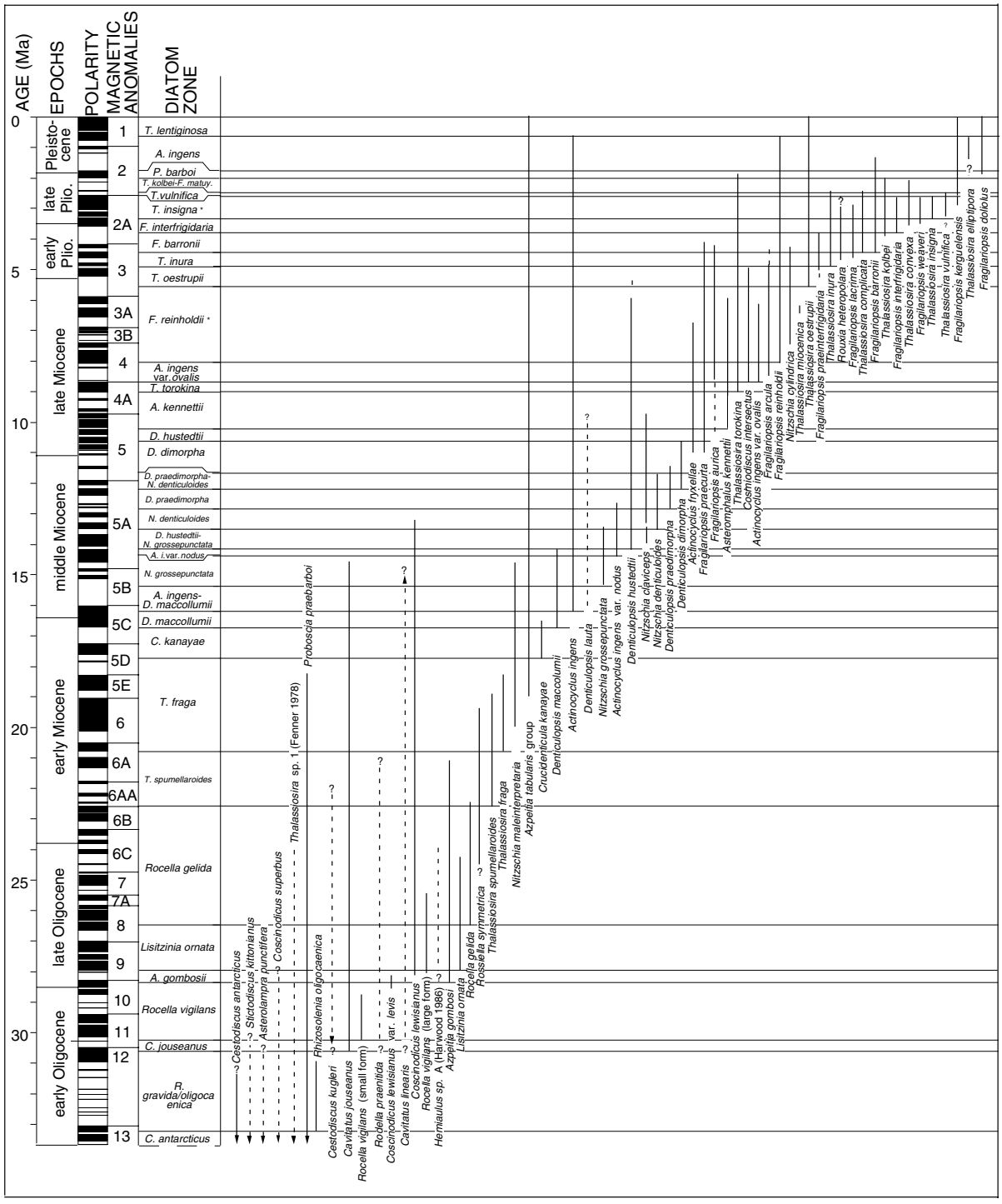

Figure F9. Drawing of cross sections of aa and pahoehoe lava flows.

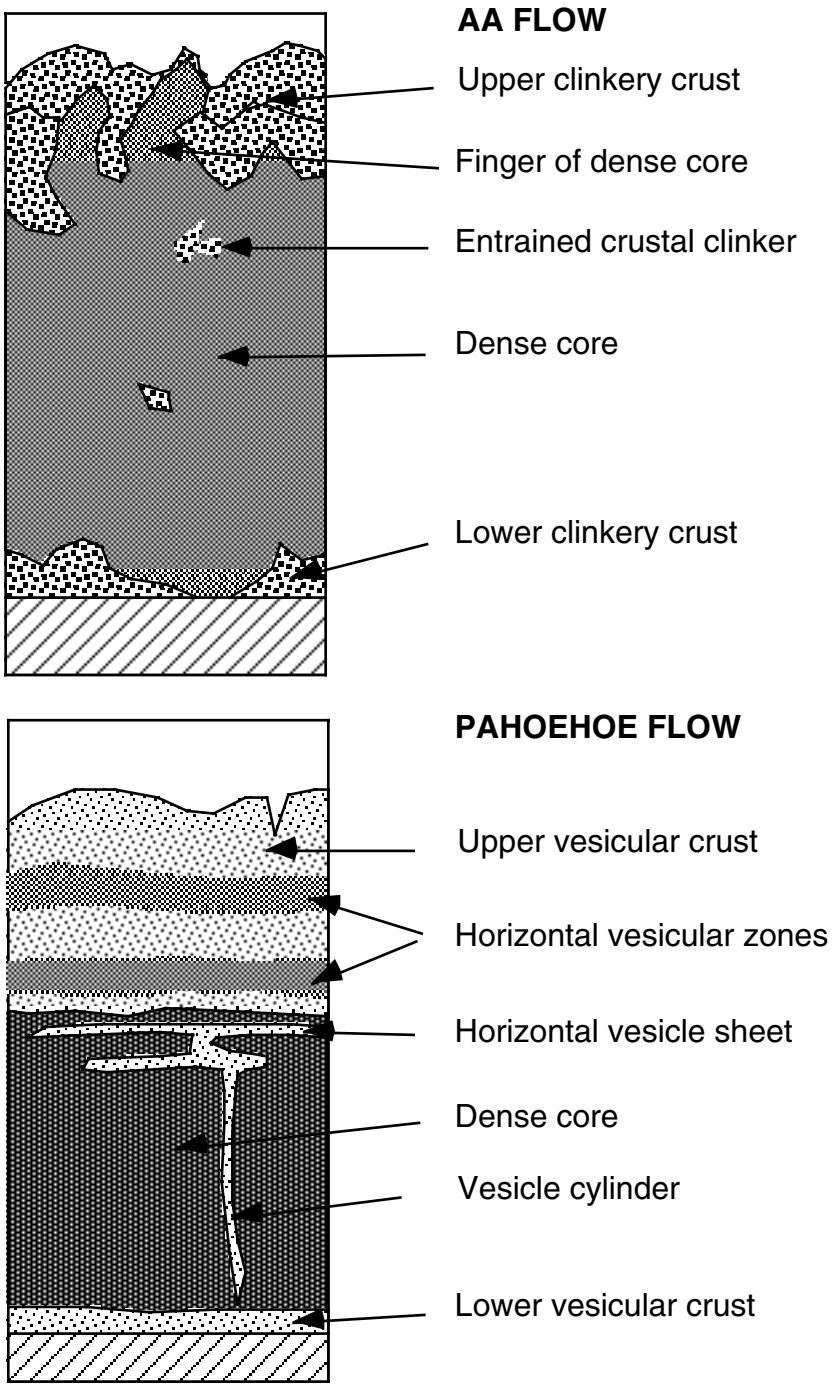

Figure F10. Example of structural geology description form.

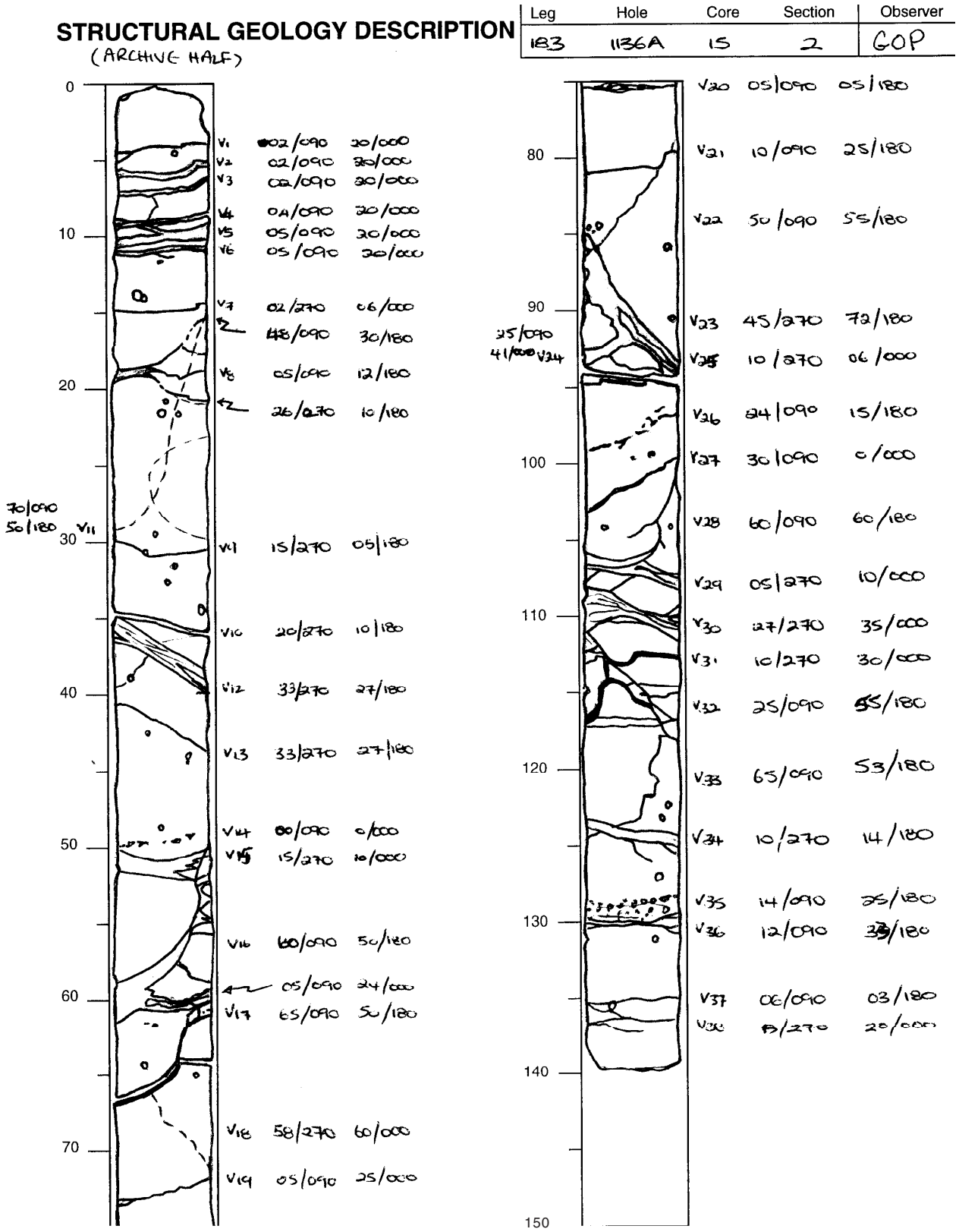

Figure F11. Orientation convention used to orient structures.

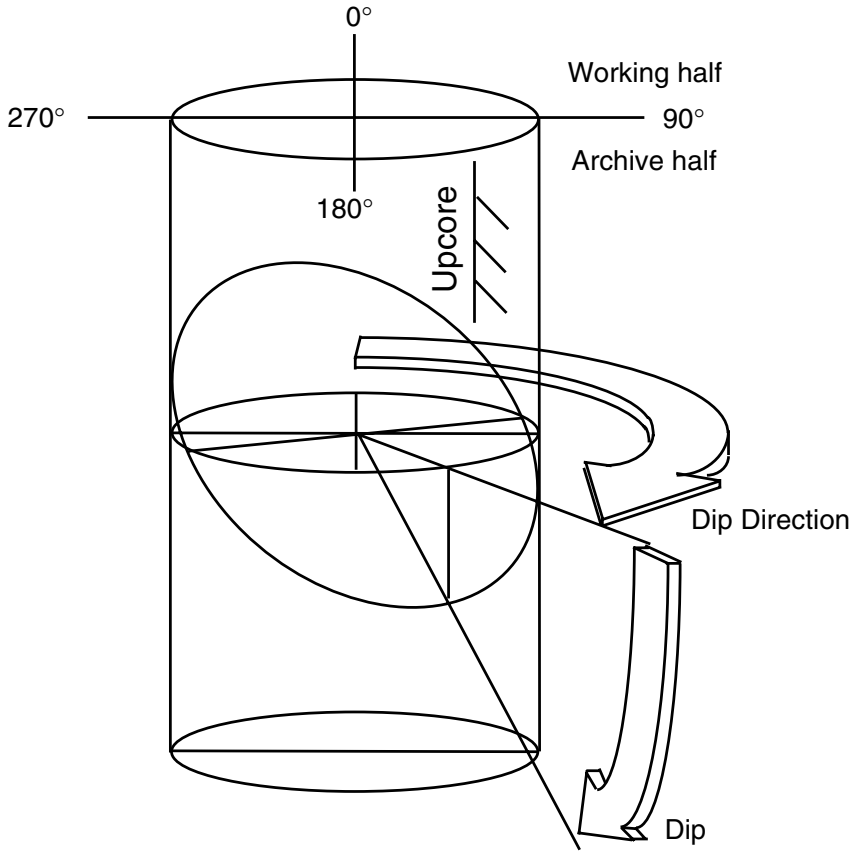

Figure F12. Schematic illustration of the configurations of tool strings run during Leg 183.

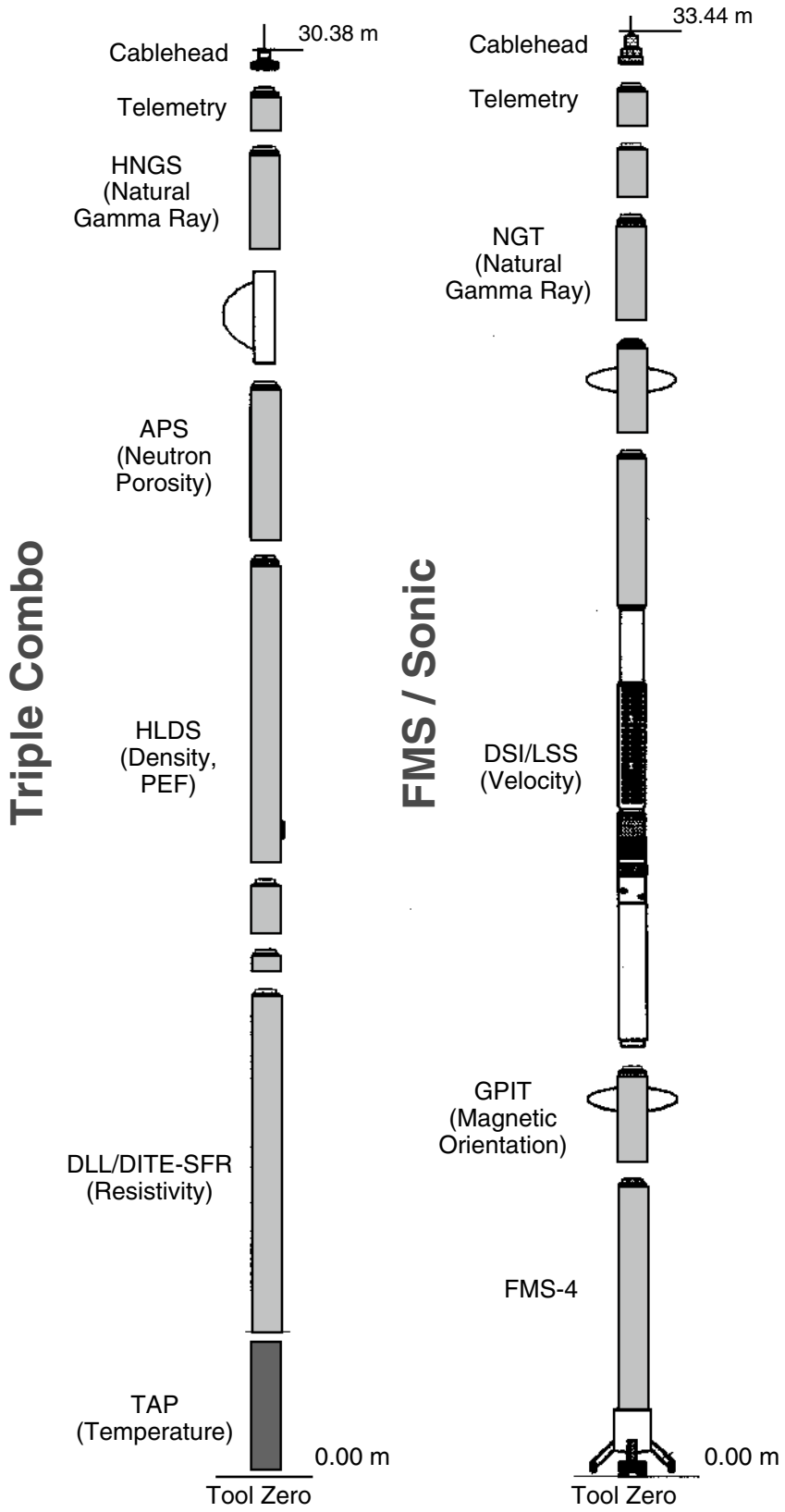

Figure F13. Diagram showing the DSI tool configuration (after Schlumberger, 1995). Distances are given in centimeters. The DSI tool is divided into a transmitter sonde, a receiver sonde, and an acquisition cartridge. The transmitter sonde drives one dual-frequency (14 and 1 kHz) monopole transmitter and two pair of dipole (2.2 kHz) transmitters. The receiver sonde houses an array of eight receiver groups with 15-cm spacing, each consisting of four orthogonal elements that are aligned with the dipole transmitters. The output from these 32 individual elements are differenced or summed appropriately to produce in-line and cross-line dipole signals or monopole-equivalent (compressional and Stoneley) waveforms.

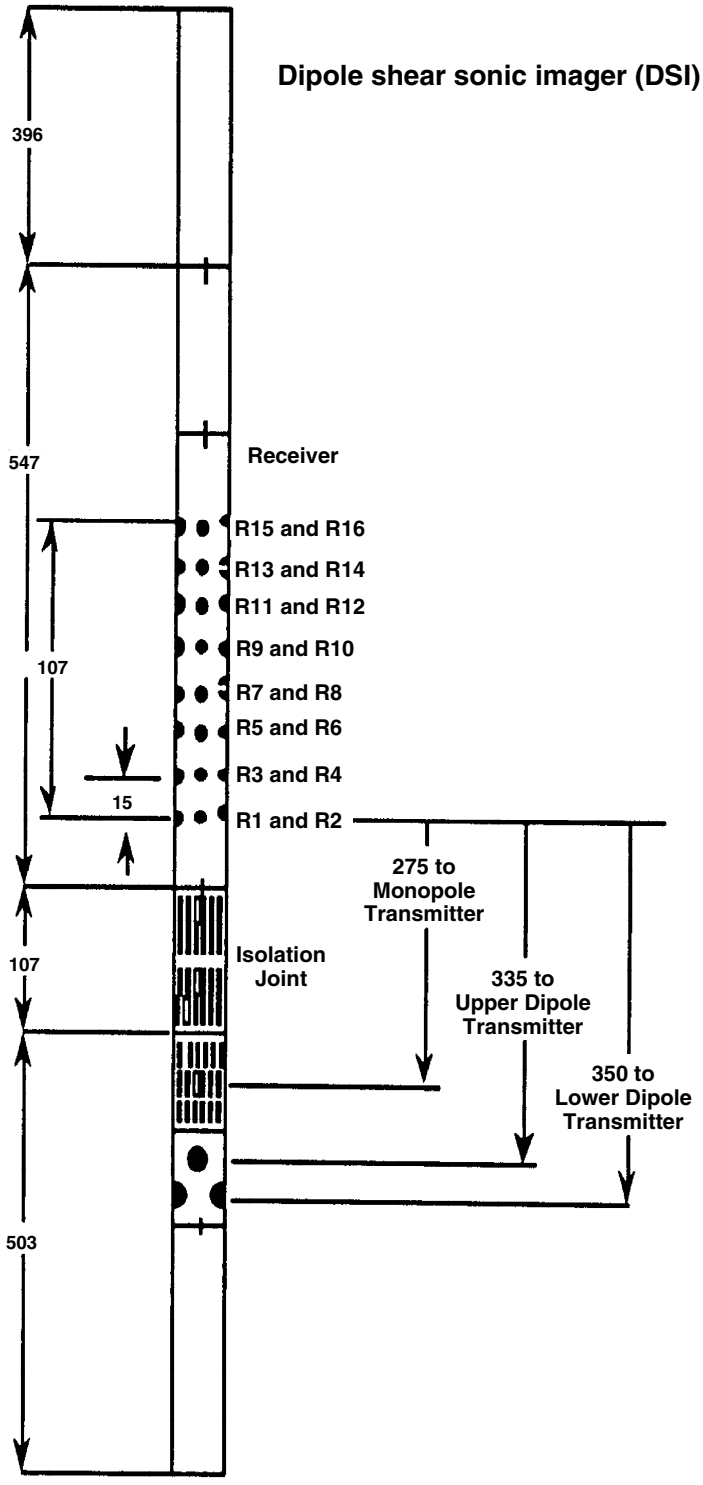

Table T1. Acquisition parameters of seismic reflection data used in selecting proposed drill sites on the Kerguelen Plateau and Broken Ridge.

Research vessel: Cruise number:	*Rig Seismic* 47	*Marion Dufresne* 47	*Robert Conrad* 2708	*Rig Seismic* 179	*Rig Seismic* 180	*Marion Dufresne* 109
Region:	Kerguelen Plateau	Kerguelen Plateau	Broken Ridge	Kerguelen Plateau	Kerguelen Plateau	Kerguelen Plateau
Year:	1985	1986	1986	1997	1997	1998
Designation:	RS47	MD47	C2708	RS179	RS180	MD109
Navigation:	Transit satellite	Transit satellite	Transit satellite	Differential GPS	Differential GPS	GPS
Source:	2 air guns	1 Flexichoc	2 water guns	20 sleeve air guns	20 sleeve air guns	10 GI air guns
Volume:	1000 in^3	NA	160 in^3	3000 in^3	3000 in^3	1050 in^3
Shot interval:	~50 m	~50 m	~65 m	~50 m	~50 m	~50 m
Sample interval:	2 ms	4 ms	1 ms	2 ms	2 ms	4 ms
Record length:	7 s + delay	4 s	9 s	16 s	16 s	17 s
Streamer length:	1200 m	2400 m	?	3000 m	3000 m	2400 m
Number of groups:	48	48	1	240	240	96
Group interval:	25 m	50 m	NA	12.5 m	12.5 m	25
Processing:	Stack	Stack	NA	F-x migration	F-x migration	F-k migration

Notes: GPS = Global Positioning System, GI = Generator-Injector. NA = not applicable, ? = unknown. F-x = frequency-distance, F-k = frequency-wave number.

Table T2. Positions of diagnostic peaks used for the identification of minerals in X-ray diffractograms and for quantification of peak intensities.

Mineral	Peak (2θ)	Peak (Å)
Quartz	26.65	3.34
K-Feldspar	26.93-27.52	3.31-3.24
Plagioclase	27.77-28.13	3.21-3.17
Hornblende	10.30-10.70	8.59-8.27
Calcite	29.45	3.03
Dolomite	30.94	2.89
Pyrite	33.05	2.71
Siderite	32.07	2.79
Opal-CT	21.94-21.67	4.05-4.10
Clinoptilolite	9.83	8.99

Note: Opal A shows a very broad peak around 4 Å.

Table T3. Volcaniclastic sediment description sheet.

Leg		Site	Hole	Core	Type	Section	Volcaniclastic sediment description sheet				
183										Observer	Recorder
Interval	Interval	Interval									
Top (cm)	Bottom (cm)	Clast/matrix (%)	Maximum size (mm)	Average size (mm)	Minimum size (mm)	Sphericity (H,M,L)	Angularity (A,SA,SR,R)	Clast morphology (El,Eq/Shape)	Sedimentary structure	Agg/weld	Notes/interpretation

Notes: Sphericity: H = high, M = medium, L = low. Angularity: A = angular, SA = subangular, SR = subrounded, R = rounded. Clast morphology: El = elongate, Eq = equant. Agg/weld = agglutinated/welded.

Table T4. Volcaniclastic breccia grid information.

Leg	Sub	Site	Hole	Core	Type	Section

Volcaniclastic breccia Grid information	
Point	(number)
Clast/Matrix (%)	
Clast size	(mm)
	short
	intermediate
	long
Jigsaw fit/clast rotated	
Sphericity	(H,M,L)
Angularity	(A,SA,SR,R)
Clast morphology	(El,Eq)
	polygonal
	triangular
	fluidal
	subsperical
	cuspate
	tabular/oblate
	comment
Sides	(number)
	concave
	convex
	planar
	irregular
	comment
Devitrification/weathering	
Sedimentary structure	composition

Notes: Sphericity: H = high, M = medium, L = low. Angularity: A = angular, SA = subangular, SR = subrounded, R = rounded. Clast morphology: El = elongate, Eq = equant.

Table T5. Vesicle description sheet.

Leg	Sub	Site	Hole	Core	Type	Section
183						

Vesicle description sheet

Observer	Recorder

Top (cm)	Bottom (cm)	Vesicularity (%)	Maximum size (mm)	Average size (mm)	Minimum size (mm)	N Density (N/cm2)	Sphericity (H,M,L)	Angularity (A,SA,SR,R)	Grading (fine U/D)	Vesicle fill (%/material)	Notes/interpretation

Notes: N = number of vesicles. Sphericity: H = high, M = medium, L = low. Angularity: A = angular, SA = subangular, SR = subrounded, R = rounded, U = fining upward, D = fining downward.

Table T6. Instrument conditions during Leg 183 XRF analyses.

Element	Line	Crystal	Detector	Collimator	Peak angle (°2θ)	Background offset (°2θ)	Total peak (s)	Count time background (s)
SiO_2	Kα	PET(002)	FPC	Coarse	109.21	0	40	0
TiO_2	Kα	LiF(200)	FPC	Fine	86.11	0	40	0
Al_2O_3	Kα	PET(002)	FPC	Coarse	145.18	0	100	0
Fe_2O_3*	Kα	LiF(200)	FPC	Fine	57.47	0	40	0
MnO	Kα	LiF(200)	FPC	Fine	62.93	0	100	0
MgO	Kα	TLAP	FPC	Coarse	45.17	±0.80	150	300
CaO	Kα	LiF(200)	FPC	Coarse	113.12	0	40	0
Na_2O	Kα	TLAP	FPC	Coarse	55.1	–1.2	150	150
K_2O	Kα	LiF(200)	FPC	Coarse	136.69	0	100	0
P_2O_5	Kα	Ge(111)	FPC	Coarse	141.09	0	100	0
Nb	Kα	LiF(200)	Scint	Fine	21.4	0.35	100	100
Zr	Kα	LiF(200)	Scint	Fine	22.55	–0.35	100	100
Y	Kα	LiF(200)	Scint	Fine	23.8	–0.4	100	100
Sr	Kα	LiF(200)	Scint	Fine	25.15	–0.4	100	100
Rb	Kα	LiF(200)	Scint	Fine	26.62	–0.6	100	100
Zn	Kα	LiF(200)	Scint	Fine	41.81	–0.55	100	100
Cu	Kα	LiF(200)	Scint	Fine	45.03	–0.4	100	100
Ni	Kα	LiF(200)	Scint	Fine	48.67	–0.55	100	100
Cr	Kα	LiF(200)	FPC	Fine	69.35	–0.5	100	100
TiO_2	Kα	LiF(200)	FPC	Fine	86.11	0.5	40	40
V	Kα	LiF(220)	FPC	Fine	123.06	–0.5	100	100
Ce	Lβ	LiF(220)	FPC	Medium	128.13	–1.5	100	100
Ba	Lβ	LiF(220)	FPC	Medium	128.78	–1.5	100	100

Notes: Total Fe as Fe_2O_3*; FPC = flow proportional counter using P10 gas; Scint = NaI scintillation counter. Trace elements analyzed under vacuum using goniometer 2 at generator settings of 60 kV and 50 mA; major elements analyzed under vacuum using goniometer 2 (1 for Na and Mg) at generator settings of 30 kV and 80 mA.

Table T7. Major element analytical precision determined during Leg 183.

Element	BHVO-1 Published values	Mean 1* (*N* = 26)	1 SD* (%)	Mean 2† (*N* = 13)	1 SD† (%)	Kilauea 1919-1**	1 SD** (%)
SiO_2	49.62	49.53	0.45	49.86	0.23	49.65	0.04
TiO_2	2.70	2.75	2.51	2.70	0.39	2.804	0.003
Al_2O_3	13.67	13.65	1.04	13.60	0.61	13.56	0.03
Fe_2O_3	12.23	12.18	0.62	12.29	1.05	12.09	0.01
MnO	0.17	0.17	2.39	0.18	2.07	0.159	0.001
MgO	7.13	7.09	1.80	7.09	0.38	6.530	0.004
CaO	11.32	11.37	0.71	11.35	0.19	11.41	0.01
Na_2O	2.27	1.99	6.11	2.08	4.29	2.44	0.02
K_2O	0.54	0.54	1.64	0.54	5.77	0.537	0.002
P_2O_5	0.27	0.26	1.91	0.28	1.88	0.286	0.001

Notes: * = analyses run through Site 1138 samples. SD = standard deviation. † = analyses run after Site 1138 samples. Means (in weight percent) and standard deviations of repeated analyses of the BHVO-1 reference standard are reported as two sets because of recalibration after mechanical repairs during the leg. ** = samples from Sites 1141 and 1142 were analyzed postcruise at The University of Massachusetts. Kilauea 1919-1 is a sample collected from the same flow as BHVO-1 and is used as a standard at The University of Massachusetts. The reported values are the average and standard deviation of three replicate measurements.

Table T8. Trace element analytical precision determined during Leg 183.

Element	Published values	Mean 1* (*N* = 13)	1 SD* (%)	Kilauea 1919-1†
TiO_2	2.7	2.7	0.3	2.83
V	317	324	3.1	279
Cr	290	295.4	1.8	299
Ni	121	120.1	0.7	114
Cu	137	132.3	1.2	
Zn	109	103.4	1.7	113
Rb	9	9.2	6.2	8.5
Sr	395	394.2	0.2	380
Y	26	25.5	3.4	25.1
Zr	179	176.6	0.7	186
Nb	19	18.5	6.7	18.7
Ba	132	131.9	4.3	133
Ce	39	32.8	13.4	33
U				0
Th				2
Pb				2
Ga				21
La				20

Notes: * = analyses run through January 21, 1999. Published values and means (parts per million except for TiO_2, which is in weight percent) and standard deviations (in percent) of repeated analyses of the BHVO-1 reference standard following Leg 183 calibration. SD = standard deviation. Trace elements were not recalibrated after mechanical repairs during the leg. † = samples from Sites 1141 and 1142 were analyzed postcruise at The University of Massachusetts. Kilauea 1919-1 is a sample collected from the same flow as BHVO-1 and is used as a standard at The University of Massachusetts. The reported values are the average and standard deviation of three replicate measurements.

Table T9. Abbreviations used in the Leg 183 alteration and vein/structure logs.

Colors	Minerals	Mineral proportions	Other
B = brown	Am, Si = amorphous silica	Tr = trace (<1%)	Ox = oxidized
Bl = blue	C = clay	X + Y = ≈50:50 x:y	P = piece(s)
Bk = black	CO_3 = calcium carbonate	X > Y = 70:30 x:y	V = vertical
G = gray	Cu = native copper	X >> Y = 90:10 x:y	R = rubble
Gn = green	Cp = chalcopyrite	X>>>Y = 99:1 x:y	Blank = same as above
Pk = pink	FeOx = iron-oxyhydroxides		-> = altered to
Pr = purple	Go = goethite		Bx = breccia
R = red	He = hematite		
Or = orange	Ol = olivine		
W = white	Pl = plagioclase		
G-Gn = gray-green, etc.	Py = pyrite		
Lt = light	Gyp = gypsum		
Dk = dark	Z = zeolite		

Note: All other minerals and colors are not abbreviated.

Table T10. Example of alteration log used during Leg 183, Kerguelen Plateau. (Continued on next two pages.)

Curatorial data							Groundmass												Breccia			
Basement unit	Core	Section	Piece	Length (cm)	Subpiece	Depth (mbsf)	Alteration (%)	Color	Vesicles (%)	Filled (%)	Dark green clay	Quartz	Black clay	Blue-green clay	White clay	Am silica	Calcite	Siderite	Volcanic	Tectonic	Matrix (%)	Clast (%)
14	67	1	1	17		633.10	H/C	Bk to brown	0											X	65	35
			2	13		633.27																
			3	33		633.40																
14	67	2	1	139		633.73	H/C	Bk to brown	0											X	65	35
14	67	3	1	150		635.12	H/C	Bk to brown	0											X	30	70
14	67	4	1	90		636.62	H	Pk/gray	0										X		15	85
							M	Green	0											X		
			2	46		637.52	S/M	Lt gray	0.1	100							100					
14	67	5	1	24		637.98	S/M	Gray	0.1	100							10	90				
			2	2		638.22																
			3	27		638.24																
			4	13		638.51																
			5	7		638.64																
			6	13		638.71																
			7	7		638.84																
			8	4		638.91																
			9	5		638.95																
			10	8		639.00																
			11	7		639.08																
			12	11		639.15																
			13	2		639.26																
14	68	1	1	101		642.60	C	Green	0										X	X	50	50
15			2	24		643.61	C	Red	0										X	X	80	20
			3	14		643.85			0													
15	68	2	1	150		643.99	M/H	Green	0										X	X	20	80
15	68	3	1	126		645.49	M/H	Gray to green	0											X		
							C	Red to black	0											X		
							M/H	Green	3	80							70	30	X	X	4	16
15	68	4	145			646.75	M	Lt green	1	100							95	5				
16							C	Red to black												X	70	30
16	68	5	1	17		646.75	H/C	Dk red to black	0										X		60	40

Note: See Table T9, p. 83, for abbreviations.

Table T10 (continued).

Curatorial data							Breccia							Phenocrysts			
Ig. Unit	Core	Section	Piece	Length (cm)	Sub	Depth (mbsf)	Red/ brown clay	Green clay	Siderite	Am silica	Fe-oxides	Sediment	Calcite	Primary mineral	Proportion (%)	Secondary mineral	Comments
14	67	1	1	17		633.10		64					1				Brecciated flow top. Slicks everywhere on all coherent clasts. Matrix (65%) is clasts + black/green clay (98%) and carbonate (2%). Clasts altered to dark brown clay.
			2	13		633.27											
			3	33		633.40											
14	67	2	1	139		633.73		64					1				Same as above, with some blue clay.
14	67	3	1	150		635.12		10	3				1				Breccia, clasts altered to clay. Lots of slicks.
14	67	4	1	90		636.62			5				1				0–68 cm: flow top breccia, 5% zeolite, 1% carbonate, remainder clasts + clay.
								30					10				68–104 cm: tectonic breccia, highly angular clasts, sheared green clay and ground up clasts (30%), carbonate (10%), rest is clasts.
			2	46		637.52											104–141: coherent flow interior. Mesostasis altered to siderite (90%) and carbonate (10%). Some resorbed clasts.
14	67	5	1	24		637.98											Massive flow interior.
			2	2		638.22											
			3	27		638.24											
			4	13		638.51											
			5	7		638.64											
			6	13		638.71											
			7	7		638.84											
			8	4		638.91											
			9	5		638.95											
			10	8		639.00											
			11	7		639.08											
			12	11		639.15											
			13	2		639.26											
14	68	1	1	101		642.60		97	1				2				Volcanic + tectonic breccia. 50% clasts altered to clay. 50% matrix. For interval: 2% carbonate, 0.1% siderite, rest = clast and clay. Clay rich zones are highly sheared and polished. Clasts from red alteration zone below in this interval.
15			2	24		643.61											Clast and matrix altered to clay. Green slicks noted.
			3	14		643.85											Clast and matrix altered to clay. Green slicks noted.
15	68	2	1	150		643.99		19	0	0			0				Breccia. 20% matrix = 95% green clay, 2% carbonate, 2% siderite, 1% am si, all recalculated for total section percent. Locally silicified. Some slicks in matrix rich areas. Some tectonic brecciation. Not all primary igneous brecciation.
15	68	3	1	126		645.49		2	5				7				0–40 cm: Tectonic breccia. Numerous hydrothermal carbonate veins. Angular clasts (bottom most clast highly sheared). Clasts broken and rotated. Matrix + vesicles = 7% carbonate, 5% siderite, 2% clay.
									10								40–66 cm: Highly altered and sheared glassy volcanic breccia. Clasts = 30%, matrix = 70% (altered to clay). Total interval = 10% siderite. Slicks noted.
																	66–126: Brecciated in places (down to 98 cm) where there is a sharp contact with vesicular basalt below. Breccias = 20% of interval and are composed of matrix (20%) and clast (80%).
15	68	4	1	145		646.75											Oxidized patches = 30% of rock. Resorbed vesicular clast from 82-100 cm.

Table T10 (continued).

Curatorial data						Breccia			Phenocrysts	
16						98	2			This breccia begins at 100 cm in section. Breccia is green and brown clays. 70% matrix yields 2% siderite in interval with the rest = clay. 30% clasts altered to clay. Some slicks.
16	68	5	1	17	646.75		1	0		Volcanic breccia. 60% clasts 40% matrix. In section: 0.5% siderite and 0.1% carbonate, rest = clay + clasts. Clasts are highly oxidized to brick red from 0–43 cm. Rare slicks. Magmatic flow textures in some clasts.

Table T11. Example of the vein-structure log used during Leg 183, Kerguelen Plateau. (**See table note.** Continued on next three pages.)

Vein-structure log for igneous rocks recovered from Hole 1138A																							
Curatorial data (mbsf)							Vein intersections				Minerals												
Depth (mbsf)	Basement unit	Core	Section	P	Ori?	L (cm)	T (cm)	B (cm)	Id	Pos (cm)	DkGnC	LtGnC	BkC	BGnC	BlC	WC	CO_3	Z	W (mm)	OriV?	Halo	W (mm)	
746.38	3	80R	1	2	Y		8	9	V1	8							100		5.0				
746.37	3	80R	1	2	Y		7	15	V2	9							100		3.0	V			
746.40	3	80R	1	2	Y		10	11	V3	11							100		0.2				
746.41	3	80R	1	2	Y		11	13	V4	12							100		0.6				
746.44	3	80R	1	2	Y		14	15	V5	14							100		0.2				
746.55	3	80R	1	4	Y		25	26	V6	25							100		0.5				
746.56	3	80R	1	4	Y		26	27	V7	26	5						95		1.0				
746.87	3	80R	1	9	Y		57	59	V9	58	100								0.3				
746.93	3	80R	1	9	Y		63	66	V10	64	5						95		1.2				
746.87	3	80R	1	9	Y		57	57	V8	57	100								0.3				
747.05	3	80R	1	10	Y		75	76	V11	75	100								0.2				
747.07	3	80R	1	10	Y		77	87	V12	78	40						60		0.2	V	bgn	2.0	
747.06	3	80R	1	10	Y		76	84	V13	76	100								0.5				
747.10	3	80R	1	10	Y		80	81	V14	81							100		1.0				
747.11	3	80R	1	10	Y		81	86	V15	80	100								0.5	V			
747.12	3	80R	1	10	Y		82	87	V16	85	50						50		0.5				
747.17	3	80R	1	11	N		87	94	V17	91	100								0.5				
747.23	3	80R	1	12	N		93	93			100								0.3				
747.26	3	80R	1	13	Y		96	101	V18	100	100								0.2				
747.42	3	80R	1	15	N		112	118	V19	112							100		0.5	V			
747.50	3	80R	1	16	N		120	126	V20	120							50	50	1.0				
747.90	4	80R	2	3	Y		33	38	V1		30							70	0.5				
747.94	4	80R	2	3	Y		37	44	V2						1			99	0.5				
748.22	4	80R	2	7	Y		65	73	V3						100				0.2				
748.36	4	80R	2	9	N		79	84	V4						100				0.2				
748.36	4	80R	2	9	N		79	84			100								0.1	V			
748.42	4	80R	2	10	Y		85	89	V5		100								0.2				
748.46	4	80R	2	10	Y		89	95	V6		100								0.2				
748.56	4	80R	2	11	Y		99	104	V7						50			50	0.4				
748.61	4	80R	2	11	Y		104	104	V8		100								0.2				
748.64	4	80R	2	12	Y		107	114	V9		60							40	0.8				
748.64	4	80R	2	12	Y		107	116	V10		40							60	0.8				
748.72	4	80R	2	12	Y		115	118	V11		100								0.2				
748.76	4	80R	2	13	Y		119	124	V12						100				0.2				
748.78	4	80R	2	13	Y		121	131	V13		100								0.1				

Table T11 (continued).

Vein-structure log for igneous rocks recovered from Hole 1138A														
Curatorial data (mbsf)							Structural (measurements)				Calculated			
Depth (mbsf)	Basement unit	Core	Section	P	Ori?	L (cm)	App-1 (°)	Dir-1 (°)	App-2 (°)	Dir-2 (°)	Strike (°)	Dip (°)	DipDir (°)	Comments
746.38	3	80R	1	2	Y		3	90	7	180	67	–8	–23	
746.37	3	80R	1	2	Y		85	270	75	0	18	85	–72	
746.40	3	80R	1	2	Y		4	270	7	180	120	–8	30	
746.41	3	80R	1	2	Y		16	270	7	180	157	–17	67	
746.44	3	80R	1	2	Y		4	270	4	0	45	6	–45	
746.55	3	80R	1	4	Y		9	90	8	180	42	–12	–48	
746.56	3	80R	1	4	Y		17	90	2	180	7	–17	–83	
746.87	3	80R	1	9	Y		17	270	1	180	177	–17	87	
746.93	3	80R	1	9	Y		31	90	15	180	24	–33	–66	
746.87	3	80R	1	9	Y		7	90	8	180	49	–11	–41	
747.05	3	80R	1	10	Y		8	90	7	180	41	–11	–49	
747.07	3	80R	1	10	Y		76	90	30	180	8	–76	–82	
747.06	3	80R	1	10	Y		55	270	50	0	40	62	–50	
747.10	3	80R	1	10	Y		16	270	15	0	43	21	–47	Connects vesicle
747.11	3	80R	1	10	Y							85	60	True dip
747.12	3	80R	1	10	Y		50	90	41	0	144	56	54	
747.17	3	80R	1	11	N									
747.23	3	80R	1	12	N									
747.26	3	80R	1	13	Y							85	90	True dip
747.42	3	80R	1	15	N									
747.50	3	80R	1	16	N									
747.90	4	80R	2	3	Y		75	270	55	0	21	76	–69	
747.94	4	80R	2	3	Y		60	270	5	180	177	–60	87	
748.22	4	80R	2	7	Y									
748.36	4	80R	2	9	N									
748.36	4	80R	2	9	N									
748.42	4	80R	2	10	Y		60	270	2	180	179	–60	89	
748.46	4	80R	2	10	Y		50	0	64	0	60	67	–30	3 mesostasis trails like this one
748.56	4	80R	2	11	Y		40	270	42	180	133	–51	43	
748.61	4	80R	2	11	Y		5	90	70	180	88	–70	–2	
748.64	4	80R	2	12	Y		77	90	35	0	171	77	81	
748.64	4	80R	2	12	Y		80	90	17	0	177	80	87	
748.72	4	80R	2	12	Y		35	270	20	0	27	38	–63	
748.76	4	80R	2	13	Y		60	90	20	0	168	61	78	
748.78	4	80R	2	13	Y		60	90	55	180	40	–66	–50	

Table T11 (continued).

Vein-structure log for igneous rocks recovered from Hole 1138A																							
Curatorial data (mbsf)							Vein intersections				Minerals												
Depth (mbsf)	Basement unit	Core	Section	P	Ori?	L (cm)	T (cm)	B (cm)	Id	Pos (cm)	DkGnC	LtGnC	BkC	BGnC	BlC	WC	CO_3	Z	W (mm)	OriV?	Halo	W (mm)
748.85	4	80R	3	1	Y		0	0	V1	0	99				1				1.0			
749.06	4	80R	3	2	Y		21	25	V2	22	100								0.1			
749.17	4	80R	3	3	N		32	34										100	0.2	V		
749.22	4	80R	3	4	Y		37	42	V3	37								100	0.1			
749.45	5	80R	3	8	Y		60	63	V4	60	60				30			5	0.5			
750.27	5	80R	4	1	Y		12	14	V1		100								0.5			
750.69	5	80R	4	2	Y		54	57	V2		100								0.1			
750.69	5	80R	4	2	Y		54	58	V3		100								0.5			
750.76	5	80R	4	2	Y		61	63	V4		100								0.5			
750.94	5	80R	4	3	Y		79	82	V5		100								1.0			
750.95	5	80R	4	3	Y		80	83	V6		100								0.5			
751.20	5	80R	4	5	Y		105	109	V7		100								0.2			
751.30	5	80R	4	6	Y		115	118	V8		100								0.2			
751.43	5	80R	4	7	Y		128	129	V9		100								0.2			
751.65	5	80R	5	1	Y		2	4	V1	2	100								0.2			
751.67	5	80R	5	1-3	Y		4	20	V2	4	100								0.2			
751.89	5	80R	5	4	N		26	27	V3	26	100								0.2			
751.90	5	80R	5	4	N		27	28	V4	27	100								0.2			

Notes: P = piece, Ori? = orientation measured (Y = yes, N = no), T = top (upper) intersection, B = bottom (lower) intersection, Id = identifier, Pos = position measured, W = vein or halo width, OriV? = vertical vein, App-1 = first apparent dip, Dir-1 = first dip direction, App-2 = second apparent dip, Dir-2 = second dip direction, DipDir = calculated dip direction. See Table **T9,** p. 83, for other abbreviations.

Table T11 (continued).

Vein-structure log for igneous rocks recovered from Hole 1138A														
Curatorial data (mbsf)							Structural (measurements)				Calculated			
Depth (mbsf)	Basement unit	Core	Section	P	Ori?	L (cm)	App-1 (°)	Dir-1 (°)	App-2 (°)	Dir-2 (°)	Strike (°)	Dip (°)	DipDir (°)	Comments
748.85	4	80R	3	1	Y		4	270	13	180	107	–14	17	
749.06	4	80R	3	2	Y		15	270	18	0	50	23	–40	
749.17	4	80R	3	3	N									
749.22	4	80R	3	4	Y		50	270	30	0	26	53	–64	
749.45	5	80R	3	8	Y		30	90	24	0	142	36	52	5% black clay
750.27	5	80R	4	1	Y		11	90	33	180	73	–34	–17	
750.69	5	80R	4	2	Y		30	90	28	180	43	–38	–47	
750.69	5	80R	4	2	Y		31	90	4	180	7	–31	–83	
750.76	5	80R	4	2	Y		16	90	5	180	17	–17	–73	
750.94	5	80R	4	3	Y							70	30	True dip, vein equivalent of 10 veins
750.95	5	80R	4	3	Y		26	270	15	0	29	29	–61	
751.20	5	80R	4	5	Y		20	270	20	180	135	–27	45	Mesostasis trail with vesicles
751.30	5	80R	4	6	Y		13	270	10	180	143	–16	53	Mesostasis trail with vesicles
751.43	5	80R	4	7	Y		9	270	25	0	71	26	–19	Mesostasis trail with vesicles
751.65	5	80R	5	1	Y		13	90	14	180	47	–19	–43	
751.67	5	80R	5	1-3	Y		80	90	10	0	178	80	88	Connects vesicles
751.89	5	80R	5	4	N		15	90	44	0	106	45	16	
751.90	5	80R	5	4	N		14	270	20	0	56	24	–34	

Table T12. Structural geology checklist used during Leg 183.

Structural geology checklist
Fractures:
Fracture density per section (1.5 m)
Veins:
Vein orientation
Average vein width
Mineral infilling
Vein fabric
Crack seal events (number of events)
Vein density per section
Wall rock alteration (width and characteristics of halo)
Crosscutting relations of veins
Vein array
Array thickness
Number of veins in array
Composition of veins
Orientation
Shear Zones:
Shear zone thickness
Lineations
Deformation bands
Color
Thickness
Mineral composition
Number of bands within array
Faults:
Orientation of fault zone
Fault zone thickness
Shear sense (offset, Riedel shears, mineral lineation)
Amount of offset
Nature of gouge
Composition of mineral infilling
Slickenside orientation
Cataclasites:
Clast size
Clast shape
Clast composition
Matrix composition (gouge or secondary minerals)
Breccias:
Matrix or clast supported
% matrix
Matrix composition
Clast size
Angular vs. rounded clasts
Clast composition
Origin (hydraulic vs. fault)
Sedimentary structures:
Layering (spacing between laminae)
Clastic dikes
Igneous contacts:
Chilled margins
Dike width
Crosscutting relations

Table T13. Specifications of the logging tools deployed during Leg 183.

Tool strings	Typical logging speed (m/hr)	Tools	Measurement	Sample interval (cm)	Approximate vertical resolution (cm)
Run 1 - Triple combination (total length = ~30.4 m)	250–275	HNGS	Natural gamma ray	15	45
		APS	Porosity	5 and 15	30
		HLDS	Bulk density, PEF	15	38
		DLL, DITE-SFR	Resistivity	15	61, 200–76
		TAP	Temperature	One per second	NA
			Tool acceleration	Four per second	NA
			Pressure	One per second	NA
Run 2 - FMS-Sonic (total length = ~33.4 m)	250–275	NGT	Natural gamma ray	15	45
		GPIT	Magnetic orientation	0.25	0.5
		DSI, LSS	Sonic velocity	15	120, 61
		FMS	Resistivity image	0.25	0.5
Run 3 - WST	Stationary	WST	Sonic traveltime	3000–5000	NA

Note: See Table T14, p. 93, for explanations of the tool and measurement acronyms. NA = not applicable.

Table T14. Logging tool and measurement acronyms and units of measurement.

Tool	Output	Explanation	Units
HNGS		Hostile environment natural gamma-ray sonde	
	HSGR	Standard (total) gamma ray	gAPI
	HCGR	Computed gamma ray (HSGR minus uranium contribution)	gAPI
	HFK	Formation potassium	%
	HTHO	Thorium	ppm
	HURA	Uranium	ppm
NGT		Natural gamma-ray tool	
	SGR	Standard total gamma ray	gAPI
	CGR	Computed gamma ray (SGR minus uranium contribution)	gAPI
	POTA	Potassium	%
	THOR	Thorium	ppm
	URAN	Uranium	ppm
APS		Accelerator porosity sonde	
	APLC	Near array porosity (limestone corrected)	%
	FPLC	Far array porosity (limestone corrected)	%
	SIGF	Neutron capture cross section of the formation (Sf)	cu (capture units)
	STOF	Tool standoff (computed distance from borehole wall)	in
HLDS		High temperature lithodensity sonde	
	RHOM	Bulk density (corrected)	g/cm^3
	PEFL	Photoelectric effect factor	$barn/e^-$
	LCAL	Caliper measure of borehole diameter	in
	DRH	Bulk density correction	g/cm^3
DLL		Dual laterolog	
	LLD	Deep laterolog	Ωm
	LLS	Shallow laterolog	Ωm
DITE-SFR		Dual induction tool-spherically focused resistivity tool	
	IDPH	Phasor deep induction	Ωm
	IMPH	Phasor medium induction	Ωm
	SFLU	Shallow spherically focused log	Ωm
TAP		High resolution temperature/acceleration/pressure tool	
	T, A, P	Temperature/acceleration/pressure	°C, mm/s^2, psi
DSI		Dipole shear sonic imager	
	V_p	Compressional wave velocity	m/s
	V_s	Shear wave velocity	m/s
LSS		Long-spaced sonic tool	
	V_p	Compressional wave velocity	m/s
FMS		Formation MicroScanner	
		Resistivity image	
GPIT		General purpose inclinometer tool	
	Hazi	Hole azimuth	°
	FNOR	Intensity of the total magnetic field	oer (oersted)
WST		Well seismic tool	
	Δt	Acoustic arrival time	μs

Table T15. LDEO-TAP tool specifications (memory mode).

TAP tool specifications (memory mode)	
Acceleration measurement range	from –2g to +2g
Acceleration resolution	1 mm/s^2
Acceleration sampling rate	
Low-resolution mode (LR)	4 Hz
High-resolution mode(HR)	8 Hz
Temperature measurement range	from –4°C to +85°C
Temperature resolution	±0.005°C
Pressure measurement range	from 0 to 10, 000 psi
Pressure resolution	1 psi
Pressure measurement precision	0.1% FS
Temperature/pressure sampling rate	1 Hz
Total data recording time	
in high-resolution mode (HR)	5 hr
in low-resolution mode (LR)	8 hr
Power source	8 alkaline batteries (D type)
Total operation time (1 set of batteries)	~40 hr